

Analysis and Mitigation of Conducted EMI Noise in SiC Fed Three-Phase Brushless DC Motor Drive

A Thesis Submitted

in Partial Fulfilment of the Requirements

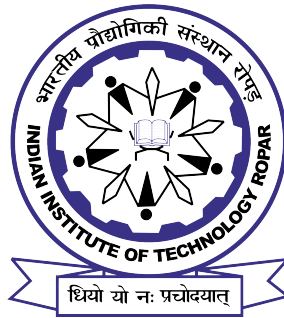
for the Degree of

DOCTOR OF PHILOSOPHY

by

Samarjeet Singh

(2019EEZ0007)



DEPARTMENT OF ELECTRICAL ENGINEERING

INDIAN INSTITUTE OF TECHNOLOGY ROPAR

February, 2024

Samarjeet Singh: *Analysis and Mitigation of Conducted EMI Noise in SiC Fed
Three-Phase Brushless DC Motor Drive*

Copyright ©2024, Indian Institute of Technology Ropar
All Rights Reserved

I dedicate the thesis to the late Prof. Parashuram Thakura.

Declaration of Originality

I hereby declare that the work which is being presented in the thesis entitled **Analysis and Mitigation of Conducted EMI Noise in SiC Fed Three-Phase Brushless DC Motor Drive** has been solely authored by me. It presents the result of my independent investigation/research conducted during the period from July 2019 to January 2024 under the supervision of Dr. J. Kalaiselvi, Assistant Professor, IIT Ropar. To the best of my knowledge, it is an original work, both in terms of research content and narrative, and has not been submitted or accepted elsewhere, in part or in full, for the award of any degree, diploma, fellowship, associateship, or similar title of any university or institution. Further, due credit has been attributed to the relevant state-of-the-art and collaborations with appropriate citations and acknowledgments, in line with established ethical norms and practices. I also declare that any idea/data/fact/source stated in my thesis has not been fabricated/ falsified/ misrepresented. All the principles of academic honesty and integrity have been followed. I fully understand that if the thesis is found to be unoriginal, fabricated, or plagiarized, the Institute reserves the right to withdraw the thesis from its archive and revoke the associated Degree conferred. Additionally, the Institute also reserves the right to appraise all concerned sections of society of the matter for their information and necessary action. If accepted, I hereby consent for my thesis to be available online in the Institute's Open Access repository, inter-library loan, and the title & abstract to be made available to outside organizations.



Signature

Name: Samarjeet Singh

Entry Number: 2019EEZ0007

Program: PhD

Department: Electrical Engineering

Indian Institute of Technology Ropar

Rupnagar, Punjab 140001

Date: 26/02/2024

Acknowledgement

I am overwhelmed with gratitude as I reflect on the incredible journey of my Ph.D., and there are several individuals whose support and guidance have been instrumental in shaping this endeavor.

First and foremost, I extend my heartfelt appreciation to my advisor, Dr. J. Kalaiselvi. Her unwavering guidance has been a guiding light throughout this research journey. The insightful feedback and suggestions she provided played a pivotal role in shaping the direction of this dissertation. I am truly grateful for her mentorship.

I would also like to express my sincere gratitude to the members of my dissertation committee: Dr. Saifullah Payami, Dr. Ravi Teja, Dr. Swati A Patel, and Dr. Ravi Kant. Their valuable insights and constructive criticism significantly enriched the quality of my work. I am fortunate to have had such a distinguished group of scholars guiding me.

A special acknowledgment goes to Dr. Naga Brahmendra Gorla for dedicating time and effort to steer me toward the successful completion of numerous studies during my Ph.D. Your commitment to excellence has been a tremendous source of inspiration, impacting me both professionally and personally.

Prof. Joseph Pou, your support has been a beacon, and I cherish our collaboration. I extend my gratitude to Dr. Prasun Mishra for his assistance in organizing my paper and helping me improve my writing skills.

I would like to recognize the continuous support of my friends Dwiza, Tushar, Poorna, Nishant, and Vishal during technical discussions. Their insights and encouragement were invaluable throughout this journey.

A heartfelt thank you to the NPTEL course, which played a significant role in improving my fundamentals and fostering my passion for research.

I extend my appreciation to the entire electrical department and its dedicated staff for their contributions to my academic growth. Special thanks to Mr. Dilbaag for his immense support in providing the necessary equipment for hardware implementation.

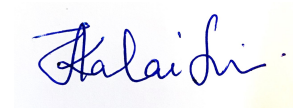
My deepest gratitude goes to my mother, whose love and understanding were my pillars of strength during this Ph.D. journey. Her encouragement provided the emotional resilience needed to navigate the challenges. I am truly blessed to have her unwavering support.

In closing, I want to express my gratitude to everyone who has played a part in this journey. Your contributions, whether big or small, have left an indelible mark on this work. I am immensely grateful for the collective support that has made this achievement possible.

Certificate

This is to certify that the thesis entitled **Analysis and Mitigation of Conducted EMI Noise in SiC Fed Three-Phase Brushless DC Motor Drive**, submitted by **Samarjeet Singh (2019EEZ0007)** for the award of the degree of **Doctor of Philosophy** of Indian Institute of Technology Ropar, is a record of bonafide research work carried out under my guidance and supervision. To the best of my knowledge and belief, the work presented in this thesis is original and has not been submitted, either in part or full, for the award of any other degree, diploma, fellowship, associateship or similar title of any university or institution.

In my opinion, the thesis has reached the standard of fulfilling the requirements of the regulations relating to the Degree.



Signature of the Supervisor

Dr. J. Kalaiselvi

Department of Electrical Engineering

Indian Institute of Technology Ropar

Rupnagar, Punjab 140001

Date: 26/02/2024

Lay Summary

The thesis explores the complexities of common-mode (CM) noise in three-phase Brushless DC (BLDC) motor drives, emphasizing the significance of the floating phase in the BLDC motor drive. It discusses the challenges posed by CM noise, which can lead to electromagnetic interference (EMI) issues. It explores various methods to mitigate this noise, including passive EMI filters for three-phase BLDC motors.

Furthermore, the thesis addresses the significance of pulse-width modulation (PWM) schemes in BLDC motor drives, and its impact on CM noise. It highlights the need for a comprehensive analysis of CM voltage, leakage current, and CM choke requirements for different PWM schemes at higher switching frequencies, with a focus on silicon carbide (SiC) fed BLDC motor drives.

The use of SiC devices is discussed for its positive impact on power converter efficiency, power density, and thermal performance. However, the challenges associated with increased switching frequencies and the resulting CM and differential-mode (DM) noise are also acknowledged. The thesis explores the use of passive EMI filters and proposes an integrated choke design to reduce the volume and occupied PCB area, aiming to improve the power density of the converter.

In summary, this technical document provides a detailed exploration of the challenges and integrated magnetic strategies for BLDC motor drives, considering advancements in semiconductor technology and the use of SiC devices. The primary emphasis of this research centers on the in-depth exploration of CM noise analysis, the influence of PWM schemes on CM noise, and the intricacies of integrated choke design for BLDC motor drives.

Abstract

The growth of brushless DC (BLDC) motor drives in industrial and residential applications emphasizes the need to effectively understand electromagnetic interference (EMI). This critical concern can significantly impact system performance and electromagnetic compatibility (EMC) requirements. This thesis addresses the nuanced challenges EMI poses in the context of a three-phase Silicon Carbide (SiC) fed BLdc motor drive, leveraging the advantages of trapezoidal back electromotive force (EMF) profiles.

While BLDC motors offer superior attributes, including high torque-to-weight ratios, enhanced efficiency, and reduced acoustic noise, the integration of wide bandgap (WBG) power devices, such as SiC and Gallium Nitride (GaN), further elevates power density and efficiency. Despite the extensive discourse on EMI issues in induction motor drives, the research has paid limited attention to EMI challenges specific to trapezoidal flux BLdc motors. This thesis fills this gap by comprehensively analyzing common-mode (CM) noise in SiC-fed BLDC motor drives. Additionally, the study investigates the influence of various pulse-width modulation (PWM) schemes on CM noise and assesses their impact on the sizing requirements of CM chokes. Furthermore, the thesis explores the design and implementation of DC-side single-stage and two-stage EMI filters for motor drives. A novel approach is employed to reduce the footprint of the EMI filter printed circuit board (PCB), and minimize the volume of the filter enclosure of the EMI filter through an integrated magnetic methodology.

In conclusion, this research contributes valuable insights into the intricate realm of EMI management in SiC-fed trapezoidal back EMF BLDC motor drives, offering practical solutions for enhancing EMC compliance while maximizing the advantages of WBG power devices in motor drive applications.

Keywords: Brushless dc motor, Common-mode noise; conducted EMI noise; EMI filters; integrated magnetics; pulse-width modulation.

List of Publications

Journal

Article 1: S. Singh, N. B. Y. Gorla, K. Jayaraman and J. Pou, "Analysis and Mitigation of the Common-Mode Noise in a Three-Phase SiC-Based Brushless DC Motor Drive With 120° Conduction Mode," in IEEE Transactions on Power Electronics, vol. 37, no. 5, pp. 5514-5523, May 2022, doi: 10.1109/TPEL.2021.3133880.

Article 2: S. Singh, B. Dwiza, K. Jayaraman and P. Mishra, "Novel Single-Stage and Two-Stage Integrated Magnetic Chokes for DC-Side EMI Filter in Motor Drive Applications," in IEEE Transactions on Power Electronics, vol. 39, no. 1, pp. 570-581, Jan. 2024, doi: 10.1109/TPEL.2023.3321635.

Article 3: S. Singh, N. B. Y. Gorla, K. Jayaraman and J. Pou, "Analysis and Mitigation of Common-Mode Noise with Different Modulation Strategies in SiC-Fed Three-Phase Brushless DC Motor Drive," in IEEE Journal of Emerging and Selected Topics in Power Electronics, doi: 10.1109/JESTPE.2023.3344532.

Article 4: S. Singh, B. Dwiza, N. B. Y. Gorla, K. Jayaraman and J. Pou, "High-Density Two-Stage Passive EMI Filter for DC-Side Application," in IEEE Industrial Electronics letter. submitted

Conference Proceeding

Article 1: S. Singh, B. Dwiza, N. B. Gorla and J. Kalaiselvi, "Toroidal-EE-Based Integrated Common-mode Choke for dc-side EMI filter," 2023 IEEE IAS Global Conference on Renewable Energy and Hydrogen Technologies (GlobConHT), Male, Maldives, 2023, pp. 1-5, doi: 10.1109/GlobConHT56829.2023.10087379.

Article 2: S. Singh, B. Dwiza, N. B. Y. Gorla, and K. Jayaraman "Design of Common-Mode Transformer for Damping of High-Frequency Leakage Current in PAM Inverter-Fed Three-Phase Brushless dc Motor Drive System," ONCON, 2023.

Article 3: S. Singh, N. B. Yadav Gorla and J. Kalaiselvi, "Comparative Analysis of Two-Phase and Three-Phase Common-Mode Equivalent Circuit for Three-Phase Brushless DC Motor Drive," 2022 IEEE International Conference on Power Electronics, Drives and Energy Systems (PEDES), Jaipur, India, 2022, pp. 1-4, doi:10.1109/PEDES56012.2022.10080062.

Contents

Declaration	iv
Acknowledgement	v
Certificate	vi
Lay Summary	vii
Abstract	viii
List of Publications	ix
List of Figures	xv
List of Tables	xxi
1 Introduction	1
1.1 Introduction to EMI	1
1.2 Literature Review	6
1.3 Motivation and Objectives	10
1.4 Scope of the Thesis and the Organization	11
2 Analysis and Mitigation of CM Noise in BLDC Motor Drive	13
2.1 Introduction	13
2.2 CM Noise Analysis	13
2.2.1 Dummy Parasitic Impedance (DPI) Network	14
2.2.2 Six-Step Commutation (SSC)	17
2.2.3 Bipolar Pulsewidth Modulation (BPWM)	18
2.2.4 CM Equivalent Circuit	22
2.3 CM Noise Mitigation with CM Choke and CM LC Filter	24
2.3.1 CM Noise Mitigation with CM Choke	26
2.3.2 CM Noise Mitigation with CM LC Filter	27
2.4 Conclusion	29
3 Impact of PWM Schemes on CM Voltage, CM Current, and CM Choke for Three-Phase BLDC Motor Drive	31
3.1 Introduction	31
3.2 PWM Schemes for Three-Phase BLDC Drive	31

3.3	CM Voltages Estimation with Various PWM Schemes	33
3.3.1	CM Voltage with Unipolar PWM Schemes	34
3.3.2	CM Voltage with Bipolar PWM Schemes	36
3.3.3	Envelope of CM Voltage	38
3.4	Experimental Validation of v_{cm} Expressions	40
3.4.1	Time Domain Results	40
3.4.2	Frequency Domain Results	42
3.5	High-Frequency Leakage Current and CM Choke Requirement	44
3.5.1	Impact of PWMs Schemes on i_{cm_BLdc}	44
3.5.2	Selecting correct CM choke and DM choke material	47
3.6	Effects of PWM on Motor and CM Performance	55
3.7	Conclusion	56
4	DC-side EMI Filters With Integrated Magnetics Chokes	57
4.1	Introduction	57
4.2	Integrated Choke for Single-Stage EMI Filter	57
4.2.1	CM Inductance	59
4.2.2	DM inductance	60
4.2.3	Magnetic Flux Density and Saturation	61
4.3	Integrated Choke for Two-Stage EMI Filter	64
4.3.1	CM Inductance	65
4.3.2	DM inductance	66
4.3.3	Magnetic Flux Density and Saturation	66
4.4	Experiment Results and Discussion	68
4.4.1	Estimation of inductances and attenuation performance of integrated chokes	71
4.4.2	Comparison of PCB Area, Volume, and Weight of EMI filters with conventional and presented chokes	75
4.4.3	Losses comparison	76
4.5	Conclusion	76
5	ER and Rectangular Core Based Integrated Chokes for DC-side EMI filters	79
5.1	Introduction	79
5.2	Toroidal-EE-Based Integrated CM Choke for DC-side Single-Stage EMI filters	79
5.2.1	Design of Integrated Choke	79
5.2.2	Experimental Validation	83

5.3	Integrated Choke for High-Density Two-Stage Passive DC-Side EMI Filters	85
5.3.1	Design of Integrated Choke	85
5.3.2	Estimation of L_{cm} Inductance	86
5.3.3	Magnetic Flux Density and Saturation	87
5.4	Experimental Verification	89
5.4.1	Estimated and measured value of L_{cm} inductance	89
5.4.2	Attenuation performance of EMI filters with conventional and integrated chokes	90
5.4.3	Comparison of PCB Area, Volume, and Weight of EMI filters with conventional and integrated chokes	91
5.5	Conclusion	91
6	Conclusion and Future Work	93
6.1	Conclusion	93
6.2	Future work	95
	References	97

List of Figures

1.1	CM noise (pink) and DM noise (green) propagation paths of EUT.	2
1.2	Three-phase SiC-inverter fed BLDC motor drive system.	2
1.3	Three-phase BLDC motor drive system where the dc-link voltage is varied by controlling the duty ratio of the dc-dc converter.	3
1.4	Three-phase BLDC motor drive system with fixed dc-link voltage.	3
1.5	Methods used for driving BLDC motor. (a) SSC, (b) H-PWM-L-ON, (c) H-ON-L-PWM, (d) PWM-ON, (e) ON-PWM, (f) bipolar PWM, (g) C-BPWM for one switching cycle, (h), M-BPWM for one switching cycle and (i) A-BPWM for one switching cycle	4
1.6	Conducted emission limit for (a) class A, and (b) class B equipment.	6
2.1	(a) Circuit diagram of SiC-based BLDC motor drive with phase-to-ground parasitic capacitances C_{ag} , C_{bg} and C_{cg} and (b) DPI network.	14
2.2	experimental setup of a three-phase BLDC drive with DPI network.	14
2.3	(a) Circuit arrangement to measure the CM impedance of the motor, (b) measured CM impedance of the motor, (c) circuit arrangement to measure the impedance of the DPI network, and (d) measured impedance of the DPI network.	15
2.4	(a) Circuit arrangement to measure i_{cm_BLdc} and i_{cm_DPI} , (b) i_{cm_BLdc} and i_{cm_DPI} , (c) enlarged waveform showing positive peaks of i_{cm_BLdc} and i_{cm_DPI} current of 'A' region, (d) enlarged waveform showing negative peaks of i_{cm_BLdc} and i_{cm_DPI} current of 'B' region, and (e) frequency spectrum of i_{cm_BLdc} and i_{cm_DPI}	17
2.5	(a) Three-phase BLDC drive with DPI network for analyzing the CM currents, (b) v_{cg} along with the currents through each phase-to-ground of DPI network (i.e., i_{ag_DPI} , i_{bg_DPI} and i_{cg_DPI}), (c) enlarged waveforms of v_{ag} , v_{bg} , v_{cg} at t_1 , (d) enlarged waveforms of v_{cg} , i_{ag_DPI} , i_{bg_DPI} and i_{cg_DPI} at t_1 , (e) enlarged waveforms v_{ag} , v_{bg} , v_{cg} at t_2 , and (f) enlarged waveforms of v_{cg} , i_{ag_DPI} , i_{bg_DPI} and i_{cg_DPI} at t_2	18
2.6	Three-phase BLDC drive with DPI network for analyzing the CM currents with BPWM. (a) v_{bg} and v_{cg} voltage waveforms indicating floating and conduction periods in v_{cg} along with corresponding DPI network currents i_{bg_DPI} and i_{cg_DPI} , (b) enlarged waveforms of v_{bg} and v_{cg} showing positive and negative dv/dt instances in conduction period along with i_{bg_DPI} and i_{cg_DPI} currents at that instances, and (c) indicating the effect of mutual inductance and capacitance, v_{og} and back EMF on v_{cg} in floating period along with i_a and i_b phase currents.	19

2.7	(a) Circuit diagram for determining the effect of mutual inductance on the floating phase voltage v_{cg} , (b) circuit diagram for determining the effect of ground parasitic capacitances on floating phase voltage v_{cg} , and (c) DPI currents i_{ag_DPI} , i_{bg_DPI} and i_{cg_DPI} at an instant when v_{cg} is floating.	20
2.8	Experimental waveform of v_{cm} and i_{cm_BLdc} for SSC and BPWM. (a) Three-phase CM equivalent circuit for both SSC and BPWM, (b) waveforms of (v_{cm}) and (i_{cm_BLdc}) along with phase-to-ground voltages (v_{ag} , v_{bg} , v_{cg}), (c) enlarged waveform showing the charging nature of i_{cm_BLdc} due to positive dv/dt in v_{cm} , (d) enlarged waveform showing the discharging nature of i_{cm_BLdc} due to negative dv/dt in v_{cm} , (e) (v_{cm}) and (i_{cm_BLdc}) profiles along with phase-to-ground voltages (v_{ag} , v_{bg} , v_{cg}), and (f) enlarged waveforms of C region showing v_{ag} , v_{bg} , v_{cg} , v_{cm} and i_{cm}	22
2.9	Bare CM noise for (a) SSC case with 150 V and 310 V dc link voltages and (b) BPWM case with a duty ratio of 30%, 50%, 70%, and 100%.	23
2.10	(a) Block diagram of three-phase BLDC drive with EMI filter, (b) simplified CM noise model for BLDC motor, (c) CM choke configuration, (d) simplified CM circuit with CM choke, and (e) CM impedance profile of motor (Z_{CM_BLdc}), CM choke (Z_{CM_choke}) and motor CM choke (Z_{CM_mod}).	24
2.11	Experimental results for SSC - dc voltage = 310 V, speed = 3500 rpm and torque = 0.316 Nm, and BPWM - dc voltage = 310 V, speed = 1860 rpm, torque = 0.28 Nm, and duty = 50%: (a) Time domain profile of i_{cm_BLdc} without and with CM choke for SSC, (b) time-domain profile of i_{cm_BLdc} without and with CM choke for BPWM with 50% duty ratio, (c) frequency domain profile without and with CM choke for SSC, and (d) frequency domain profile without CM choke for BPWM with 100% duty ratio, with CM choke for BPWM with 100% and 50% duty ratio.	25
2.12	(a) LC circuit configuration and (b) simplified CM equivalent circuit with LC circuit configuration.	27
2.13	Experimental results for SSC - dc voltage = 310 V, speed = 3500 rpm and torque = 0.316 Nm, and BPWM - dc voltage = 310 V, speed = 1860 rpm, torque = 0.28 Nm, and duty = 50%: (a) Time domain profile of i_{cm_BLdc} without and with LC filter for SSC (b) time-domain profile of i_{cm_BLdc} without and with LC filter for BPWM with 50% duty ratio, (c) frequency domain profile without and with LC filter for SSC, and (d) frequency domain profile without LC filter for BPWM with 100% duty ratio, with LC filter for BPWM with 100% and 50% duty ratio.	28
3.1	Three-phase SiC-fed BLDC motor drive system with sector information.	32

3.2	(a) Phase current, back-emf and sector information of phases a , b and c with SSC scheme, (b) gating signals of H-PWM-L-ON scheme, (c) gating signals of PWM-ON scheme, and (d) gating signals of bipolar PWM scheme.	32
3.3	Gating signals in a switching cycle with (a) C-BPWM scheme and (b) M-BPWM scheme.	33
3.4	(a) Trapezoidal waveform indicating the rise time (t_r) and fall time (t_f), (b) envelope of the trapezoidal waveform in the frequency domain, (c) effect of amplitude (A) on the envelope, and (d) effect of switching frequency (f_{sw}) on the envelope.	37
3.5	Experimental setup of a three-phase SiC-fed BLDC drive.	38
3.6	Estimated time domain profile for v_{cm} , (a) v_{cm_hwpwm} , (b) v_{cm_pwm} , (c) v_{cm_cbpwm} , and (d) v_{cm_mbpwm}	38
3.7	Experimental time domain profiles of, (a) v_{cm_hwpwm} , (b) zoomed v_{cm_hwpwm} in Sectors 2 and 3, (c) v_{cm_pwm} , (d) zoomed v_{cm_pwm} in Sectors 2 and 3, (e) v_{cm_cbpwm} , (f) zoomed v_{cm_cbpwm} in Sectors 2 and 3, (g) v_{cm_mbpwm} , and (h) zoomed v_{cm_mbpwm} in Sectors 2 and 3, for $V_{dc} = 310$, $d = 0.5$ and $f_{sw1} = 10$ kHz.	39
3.8	Experimental and estimated frequency spectra of v_{cm} at $f_{sw1}=10$ kHz shown in blue and green, respectively and $f_{sw2}=100$ kHz shown in pink and red, respectively, (a) v_{cm_hwpwm} , (b) v_{cm_pwm} , (c) v_{cm_mbpwm} , and (d) v_{cm_cbpwm}	42
3.9	CM voltage for C-BPWM, (a) v_{cm_cmpwm} at $f_{sw}=100$ kHz and (b) enlarge view of v_{cm_cmpwm}	43
3.10	(a) Parasitic capacitance in three-phase BLDC motor drive, (b) CM equivalent circuit, and (c) Z_{cm_BLdc} impedance profile.	44
3.11	Frequency spectra of i_{cm_BLdc} for different modulation schemes at 10 kHz f_{sw} with and without CM choke, (a) H-PWM-L-ON, (b) PWM-ON, (c) C-BPWM, and (d) M-BPWM.	45
3.12	Frequency spectra of the i_{cm_BLdc} for different modulation schemes at 100 kHz f_{sw} with and without CM choke, (a) H-PWM-L-ON, (b) PWM-ON, (c) C-BPWM, and (d) M-BPWM.	46
3.13	Frequency spectra indicating the f_{sw} component and its multiples of the i_{cm_BLdc} with H-PWM-L-ON, PWM-ON, C-BPWM and M-BPWM schemes at (a) $f_{sw1} = 10$ kHz and (b) $f_{sw2} = 100$ kHz.	47
3.14	Required attenuation and f_c at (a) $f_{sw1} = 10$ kHz and (b) $f_{sw2} = 100$ kHz.	47
3.15	(a) Variation of permeability concerning frequency for different magnetic materials and (b) effect of saturation flux density for temperature.	48
3.16	(a) Comparison for iron powder core for DM choke.	50
3.17	Flowchart employed for CM choke design.	51
3.18	CM chokes for $f_{sw1} = 10$ kHz and $f_{sw2} = 100$ kHz with H-PWM-L-ON, PWM-ON, C-BPWM, and M-BPWM schemes.	54

4.1	Integrated choke for single-stage EMI filter. (a) ER, I, and toroidal cores arrangement, (b) electrical equivalence, (c) winding structure and terminal connections, (d) flux due to i_{cm} and i_{dm} currents in the presented choke, (e) magnetic equivalent circuit of ER and I cores with i_{cm} current, (f) magnetic equivalent circuit of the toroidal core with i_{cm} current, (g) terminal connection to measure $L_{cm(ss)}$, (h) magnetic equivalent circuit of ER and I cores with i_{dm} current, and (i) terminal connection to measure $L_{dm(ss)}$ inductance.	58
4.2	(a) Magnetic flux and flux density in various cross-sectional areas of the presented choke, (b) exploded view of the magnetic structure with dimensions of the ER, I, and toroidal cores for ANSYS 3D model, (c) CM flux distribution in ER and I cores, (d) CM flux distribution in the toroidal core, (e) DM flux distribution in ER and I cores, and (f) DM flux distribution in toroidal core.	61
4.3	Integrated choke for two-stage EMI filter. (a) ER and two toroidal cores arrangement, (b) electrical equivalence, (c) winding structure and terminal connections, (d) flux due to i_{cm} and i_{dm} currents in the presented choke, (e) magnetic equivalent circuit of ER cores with i_{cm} current, (f) magnetic equivalent circuit of the toroidal core with i_{cm} current, (g) terminal connection to measure $L_{cm(ts)}$, (h) magnetic equivalent circuit of ER cores with i_{dm} current, and (i) terminal connection to measure $L_{dm(ts)}$ inductance.	63
4.4	(a) Magnetic flux and flux density in various cross-sectional areas of the presented choke (b) exploded view of the magnetic structure with dimensions of the ER and toroidal cores for ANSYS 3D model, (c) CM flux distribution in ER cores, (d) CM flux distribution in the two toroidal core, (e) DM flux distribution in ER cores, and (f) DM flux distribution in the two toroidal core.	64
4.5	(a) Experimental diagram to measure CM and DM noise for BLDC drive system, (b) laboratory setup for EMI test, (c) bare CM noise, and (d) bare DM noise. . .	67
4.6	(a) Single-stage EMI filter and (b) two-stage EMI filter.	69
4.7	Design flowchart and dimensions of the integrated chokes. (a) Design flowchart of integrated choke for single-stage EMI filter, (b) design flowchart of integrated choke for two-stage EMI filter, (c) dimensions for integrated choke for single-stage EMI filter, and (d) dimension for integrated choke for two-stage EMI filter. . . .	71
4.8	DC-side EMI filters. (a) Single-stage EMI filter and (b) two-stage EMI filter. . .	72
4.9	Measured impedance (solid line) and phase (dotted line) of presented and conventional EMI choke. (a) CM impedance of presented and conventional EMI choke for single-stage, (b) DM impedance of presented and conventional EMI choke for single-stage, (c) CM impedance of presented and conventional EMI choke for two-stage, and (d) DM impedance of presented and conventional EMI choke for two-stage.	73

4.10	EMI performance of the filter. (a) CM performance of conventional and presented single-stage EMI filter (b) DM performance of conventional and presented single-stage EMI filter, (c) CM performance of conventional and presented two-stage EMI filter, and (d) DM performance of conventional and presented two-stage EMI filter.	74
4.11	Thermal performance of the filter. (a) Conventional single-stage EMI filter (b) integrated single-stage EMI filter, (c) conventional two-stage EMI filter, and (d) integrated two-stage EMI filter.	74
5.1	(a) Prototype of integrated choke, (b) electrical equivalence of the integrated choke, and (c) winding structure and terminal connection of integrated choke. . .	80
5.2	(a) Magnetic equivalent circuit with i_{cm} current excitation, (b) terminal connections for the integrated choke to measure the L_{cm_prop} inductance, (c) magnetic equivalent circuit with i_{dm} current excitation, (d) simplified magnetic circuit with the i_{dm} current excitation, and (e) terminal connections for the integrated choke to measure the L_{dm_prop} inductance.	82
5.3	Comparison of (a) CM impedance profile of conventional and presented integrated choke, (b) DM impedance profile of conventional and presented integrated choke, and (c) experimental setup of a three-phase Sic-fed BLDC drive.	82
5.4	(a) Bare CM noise, CM noise with conventional choke, and CM noise with integrated choke for three-phase BLDC motor, (b) Bare DM noise, DM noise with conventional choke, and DM noise with integrated choke, (c) EMI filter with conventional and integrated chokes, (d) thermal image of integrated choke, and (e) thermal image of conventional choke.	84
5.5	Integrated choke. (a) toroidal and rectangular cores arrangement, (b) electrical equivalence, (c) winding structure and terminal connections, (d) flux due to i_{cm} and i_{dm} currents in the integrated choke, (e) magnetic equivalent circuit of the rectangular core with i_{cm} current, (f) magnetic equivalent circuit of the toroidal core with i_{cm} current, and (g) terminal connection to measure L_{cm} inductance. .	85
5.6	(a) Magnetic flux in various cross-sectional areas of the integrated choke, (b) exploded view of the magnetic structure with dimensions of the rectangular and toroidal cores for ANSYS 3D model, (c) CM flux distribution in toroidal cores, (d) CM flux distribution in the rectangular core, (e) DM flux distribution in toroidal cores, and (f) DM flux distribution in rectangular core.	86
5.7	(a) Experimental setup, (b) CM spectra of conventional and presented integrated EMI choke, and (c) DM spectra of conventional and presented integrated EMI choke.	88

5.8	(a) DC-side two-stage EMI filter, (b) measured CM impedance of conventional and presented integrated EMI choke, and (c) measured DM impedance of conventional and presented integrated EMI choke.	89
5.9	DC side two-stage EMI filter. (a) Conventional filter and (b) presented integrated filter.	90

List of Tables

2.1	Specifications of BLDC motor	15
3.1	Phase-to-Ground Voltages in Sector 1 with C-BPWM Scheme	36
3.2	Phase-to-Ground Voltages in Sector 1 with M-BPWM Scheme	37
3.3	BLDC Motor Specifications	40
3.4	Parameters of CM Choke	53
4.1	Core Properties	70
4.2	Estimated and Measured $L_{cm(ss)}$, $L_{dm(ss)}$, $L_{cm(ts)}$, and $L_{dm(ts)}$ Inductance . . .	72
4.3	Conventional CM and DM choke details	73
4.4	Comparison Between Conventional and Presented EMI Filter	75
4.5	Loss Comparison Between Conventional and Presented EMI Filters.	76
5.1	Estimated and Measured $L_{cm-prop}$, $L_{cm-conv}$, $L_{dm-prop}$ and $L_{dm-conv}$ inductance .	83
5.2	Magnetic Core Properties	91
5.3	Comparison Between Conventional and presented Integrated EMI Filter	91

Abbreviations

EMI	Electromagnetic interference
CM	Common-mode
DM	Differential mode
PCB	Printed circuit board

Chapter 1

Introduction

1.1 Introduction to EMI

Electromagnetic Interference (EMI) is an undesirable phenomenon characterized by undesired electromagnetic noise that detrimentally impacts or disrupts the operational efficacy of nearby systems, including the power converter itself. EMI study is grouped into four categories namely conducted susceptibility, radiated susceptibility, conducted emissions, and radiated emissions. The susceptibility or immunity issues represent the ability of electrical equipment to reject the noise in the presence of external electromagnetic disturbances such as conducted emissions (CE) and radiated emissions (RE). CE refers to the electromagnetic energy generated by a power electronic converter, which propagates through a conductive medium. On the other hand, RE encompasses all unintentional electromagnetic energy emanating from the electronic device. These emissions collectively contribute to the overall EMI, potentially compromising the integrity and functionality of adjacent electronic systems.

To ensure the proper functioning of electronic systems, these emissions are subject to regulation and must comply with the principles of electromagnetic compatibility (EMC). EMC is defined as the ability of a device or system to operate effectively in its electromagnetic environment without causing unacceptable electronic disturbances to anything within that environment. The range specified for CE by the standards is 150 kHz to 30 MHz. CE tests are carried out to measure the amount of CE noise generated by the equipment under test (EUT). CE is decoupled and characterized as common-mode (CM) and differential-mode (DM) noise. The CM noise propagates between the power line and the system ground and the DM noise propagates between the power lines, as shown in Figure 1.1. The CM and DM noise deteriorates the system performance and if unaddressed may cause serious EMI issues with nearby equipment.

The CM and DM noise are analyzed in a wide variety of applications; however, this thesis is focused on the three-phase silicon carbide (SiC) inverter-fed brushless DC (BLDC) motor drive system. The goal of studying conducted EMI in a three-phase SiC-fed BLDC motor drive is to restrict the CE of the motor drive within the

desired standard limits, which can be achieved by thoroughly understanding the CE generation mechanism and exploring the suitable mitigation techniques.

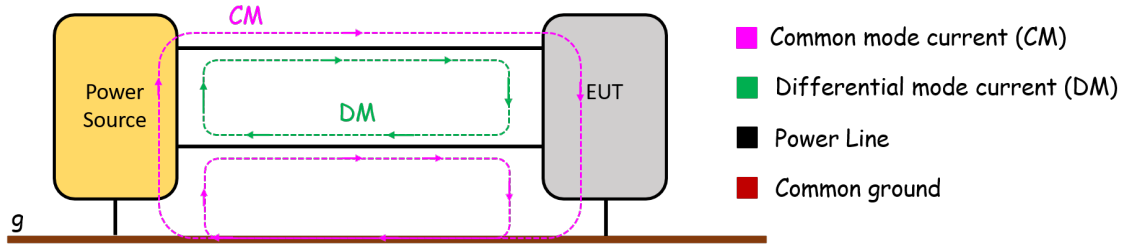


Figure 1.1: CM noise (pink) and DM noise (green) propagation paths of EUT.

The system under analysis is shown in Figure 1.2 which represents a three-phase BLDC motor drive. The inverter consists of six SiC switches and a DC-link capacitor (C_{dc}). The dominant parasitic capacitance of the motor and inverter are shown in Figure 1.2. The line impedance stabilization network (LISN) is connected to decouple the noise from the outside disturbance and to offer a constant impedance for CM and DM noise in the presence of a spectrum analyzer to measure the EMI noise. Figure 1.2 shows the DC and AC EMI filter's placement in the BLDC motor drive to achieve the desired CE standard limits. Further, a brief description of the BLDC motor drive and the EMI filter are discussed.

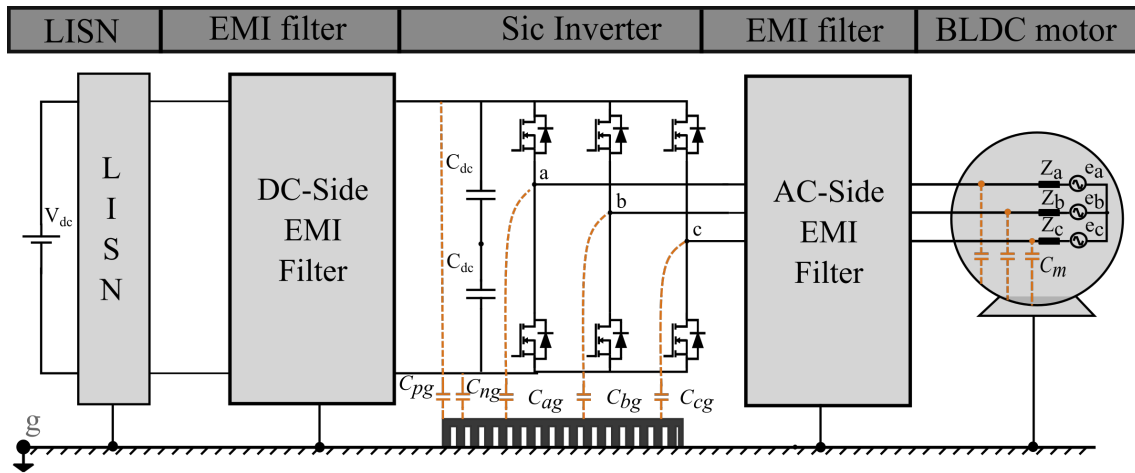


Figure 1.2: Three-phase SiC-inverter fed BLDC motor drive system.

1. BLDC motor drive:

The BLDC motor drive comprises a three-phase inverter and a BLDC motor, as illustrated in Figure 1.2. In the operation of a three-phase BLDC motor drive, two phases conduct simultaneously, presenting six possible ways to energize the coil pairs. The rotor initiates rotation by commutating the phases every 60° electrical.

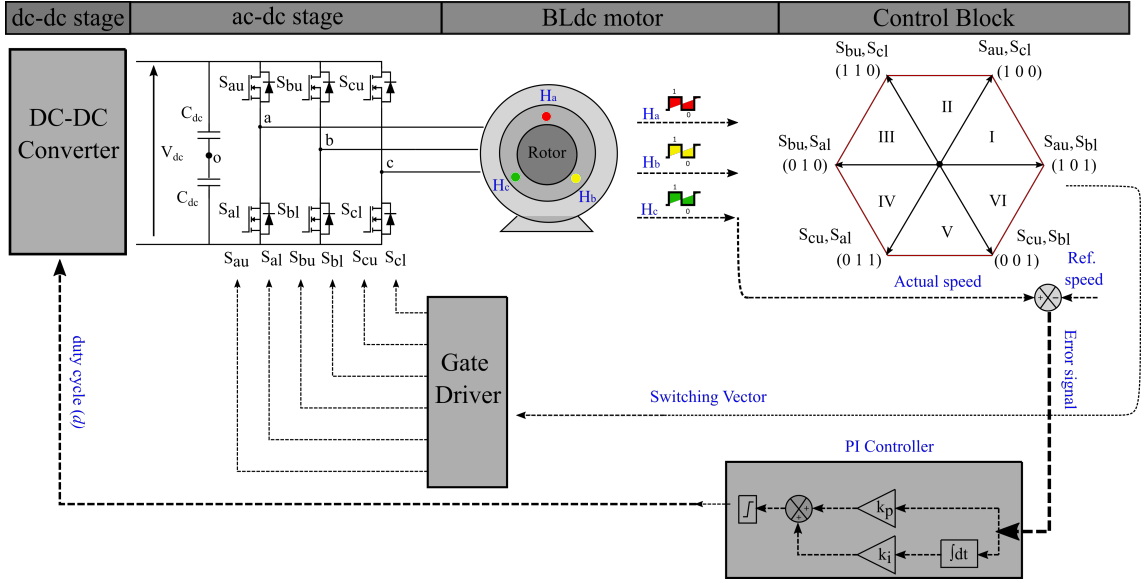


Figure 1.3: Three-phase BLDC motor drive system where the dc-link voltage is varied by controlling the duty ratio of the dc-dc converter.

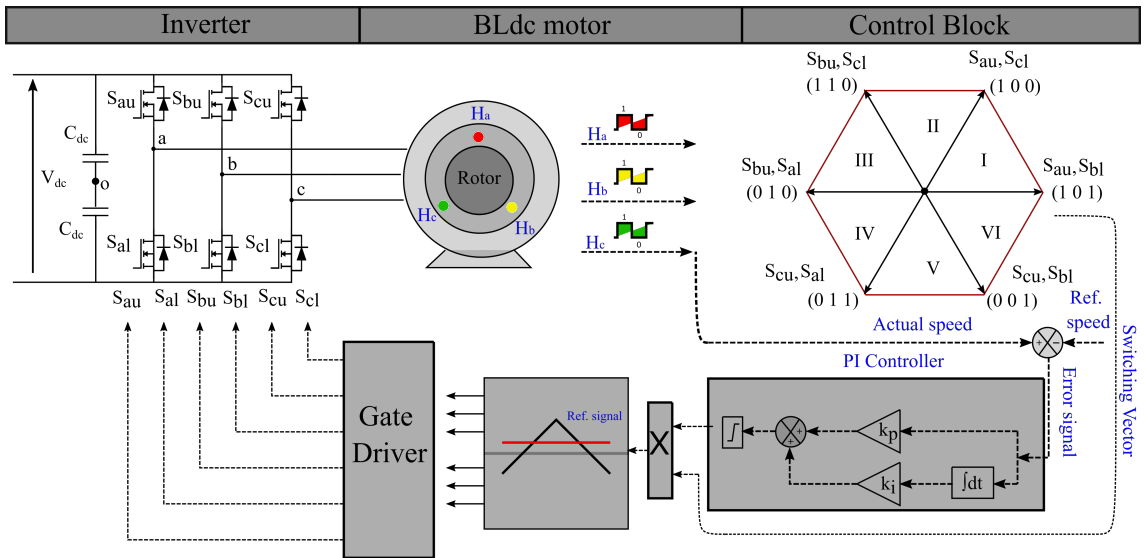


Figure 1.4: Three-phase BLDC motor drive system with fixed dc-link voltage.

For driving the BLDC motor, both Pulse Amplitude Modulation (PAM) and Pulse-Width Modulation (PWM) techniques are employed as shown in the Figures. 1.3 and 1.4, respectively. As evident from Figure. 1.3, with the PAM technique, the BLDC motor is controlled by tracking the rotor position with the help of a hall sensor. Based on the rotor position, the switches of the corresponding phase are switched. The entire logic is developed in the microcontroller, which intakes the hall sensor output and generates six controlled pulses for controlling the three-phase inverter. Figure 1.5(a) illustrates the ideal voltage and phase current waveforms of the three-phase BLDC motor operated with six-step commutation (SSC) which comprises six

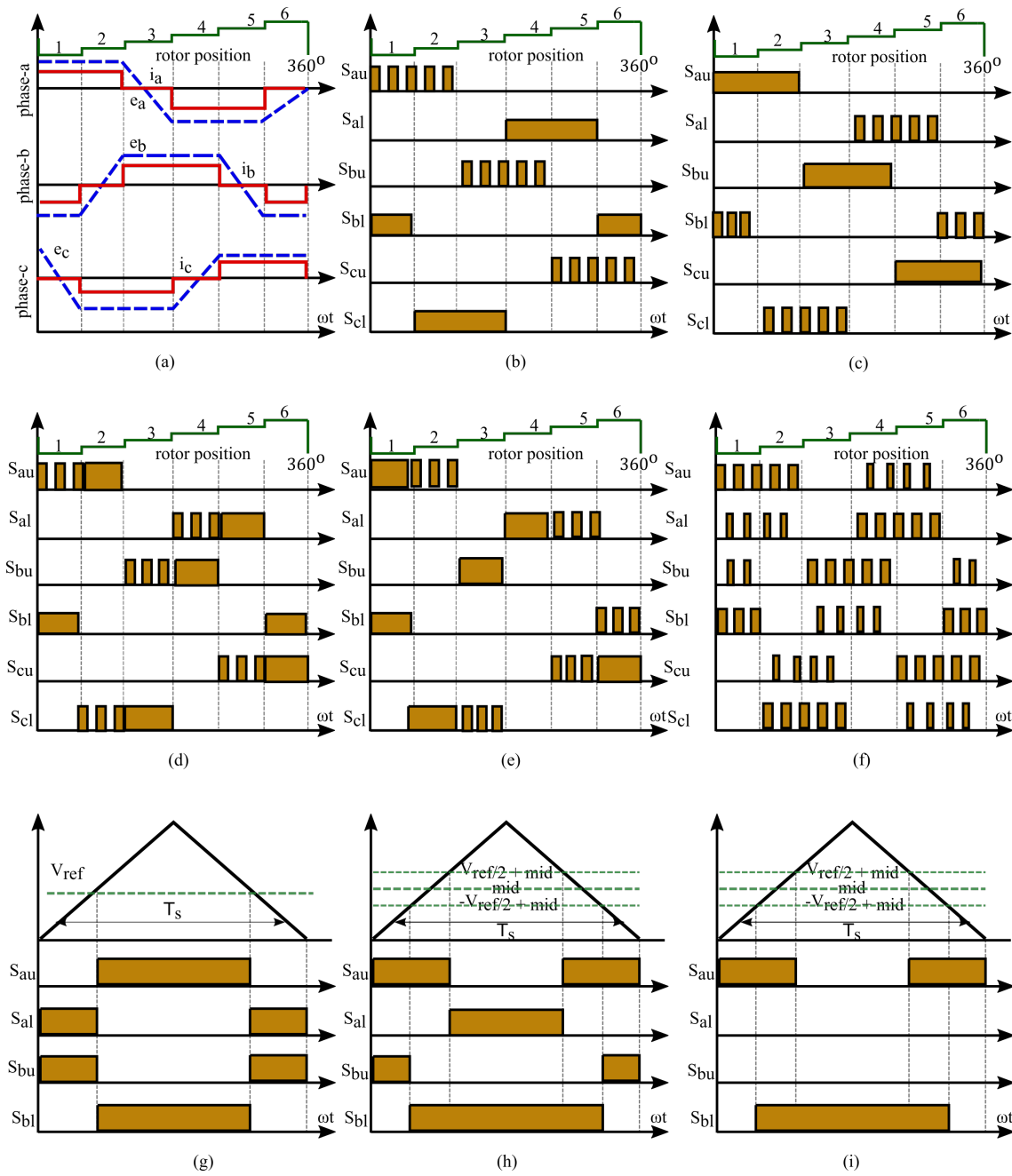


Figure 1.5: Methods used for driving BLDC motor. (a) SSC, (b) H-PWM-L-ON, (c) H-ON-L-PWM, (d) PWM-ON, (e) ON-PWM, (f) bipolar PWM, (g) C-BPWM for one switching cycle, (h), M-BPWM for one switching cycle and (i) A-BPWM for one switching cycle

sectors. The drive cycle of a BLDC motor is divided into six sectors, which is commonly known as a six-step commutation (SSC). Each 180° electrical is divided into a conduction interval for 120° electrical and a floating period for 60° electrical as shown in Figure 1.5(a). Therefore, in an SSC-operated BLdc drive, switches corresponding to two phases conduct simultaneously with the third phase floating. In this case, the DC-link voltage is varied using a DC-DC converter for controlling the speed of the motor, such a method is categorized as PAM technique.

In the case of fixed DC-link voltage, PWM methods are employed to drive the BLDC motor, as illustrated in Figure 1.4. The various PWM for BLDC motor drives are shown in Figures 1.5(b)-(i). Figures 1.5(b)-(e), illustrate unipolar PWM schemes, in which either the high side or the low side switch is controlled by PWM. The popular unipolar PWM methods are H-PWM-L-ON, H-ON-L-PWM, PWM-ON, and ON-PWM as shown in Figures 1.5(b)-(e), respectively. In H-PWM-L-ON and H-ON-L-PWM either the high side switch or the low side switch is controlled by PWM switching for 120° period, as shown in Figures 1.5(b) and (c), respectively. In the case of PWM-ON, the first 60° of the time period is controlled by PWM switching and for the other 60° time period the switch is clamped to a positive DC-link or a negative DC-link, as shown in Figure 1.5(d). In the case of ON-PWM the first 60° of the period is clamped to a DC-link positive or negative line and for the next 60° of the period it is controlled by PWM switching, as shown in Figure 1.5(e). Figure 1.5(f) illustrates the gate signals for 360° electrical with bipolar PWM technique. As shown in Figure 1.5(f), both the high and low side switches of one of the phases are controlled by a PWM signal, and the duty ratio is derived from the speed reference. The control signals for the other two phases are shifted by 120° and 240° electrical. The various switching patterns for the bipolar PWM technique, shown in Figure 1.5(f), are given in Figures 1.5(g)-(i) for one switching cycle. The conventional bipolar PWM, abbreviated as either BPWM or C-BPWM, generates a symmetric gate pulse during the conducting phase as shown in Figure 1.5(g). However, in the case of modified bipolar PWM (M-BPWM), the complementary switching mode enables bipolar voltage output by operating four switches complementarily. The non-complementary switching mode is shown in Figure 1.5(i) outputs only unipolar voltage by operating only two switches non-complementarily. The advantages of PAM [1], [2] and PWM are extensively discussed in [3], [1], [4], [5], and [2].

2. EMI Filter:

EMI filters are primarily employed to suppress electromagnetic noise generated during the operation of the motor drive system. In the motor drive systems, either the DC side or AC side or both AC and DC side EMI filters are employed. Both the AC and DC side EMI filters suppress the EMI noise helping to meet these regulatory requirements and enhance the reliability of the system. The conducted emission limit for EN5022 for class A and class B equipment is shown in Figures 1.6(a) and (b) respectively.

Passive EMI filters use capacitors, inductors, and resistors to filter out

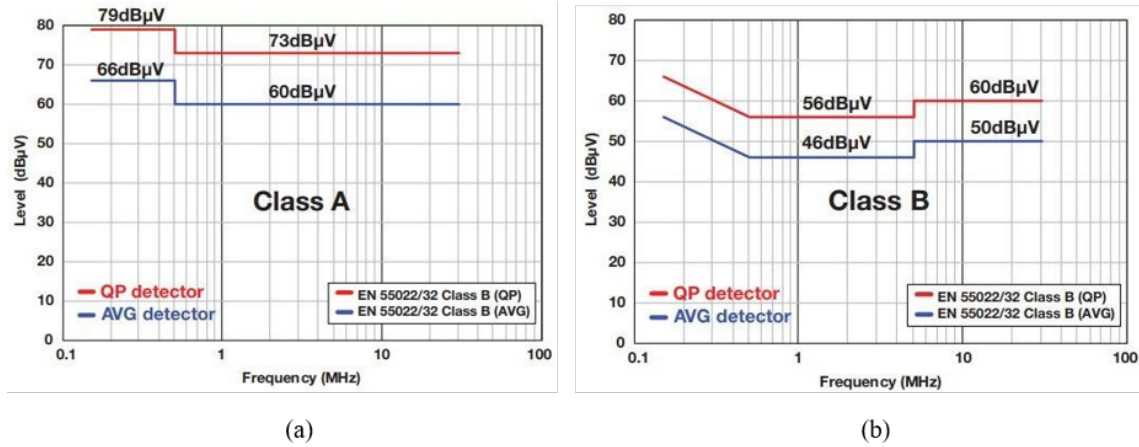


Figure 1.6: Conducted emission limit for (a) class A, and (b) class B equipment.

unwanted high-frequency components. Various filter topologies have been extensively discussed in [6]. However, the conventional passive EMI filters are bulky and occupy large space which reduces the power density of the converter. Thus, the passive integrated EMI filters are explored to improve the power density of the converter. Various passive integrated EMI filters are reported in the literature and are discussed in Chapter 1.2 of the thesis.

Thus, EMI filters are an integral part of ensuring the smooth and interference-free operation of motor drive systems.

1.2 Literature Review

BLDC motor drive with trapezoidal back electromagnetic force (EMF) profile has been widely adopted in various industrial and residential applications because of its significant advantages such as high torque-to-weight ratio, better efficiency, and less acoustic noise [7],[8],[9]. Moreover, the BLDC motors that were so far confined to low-voltage drives (e.g., 48 V) are now in consideration for high-voltage drives (200 V and above) in applications such as electric vehicles (EVs) and solar water pumps [10]. Extensive research has been carried out on high-voltage BLDC motors to optimize the efficiency without compromising the power density and torque ripple [11].

Due to rapid advancement in semiconductor technology, wide-bandgap (WBG) power devices are preferred to achieve increased power density and efficiency in power converters, even while operating in harsh environmental conditions [12]. Thus, WBG devices such as silicon carbide (SiC) and gallium nitride (GaN) are increasingly used for motor drive applications [13]. The operation of SiC-based BLDC drive with high switching frequency is desirable as it improves the torque

ripple performance of the motor [14]. However, an increase in switching frequency parallel with high operating voltages and faster switching transitions amplify the CM issues [15]. The CM voltages with a high-voltage slew rate (i.e., dv/dt) excite the motor's and converter's parasitic elements, leading to high-frequency leakage currents through the ground. These leakage currents through the ground result in CM noise, which can deteriorate the system performance and degrade the reliability of the whole system [16]. The instantaneous dv/dt responsible for the CM noise is dictated by both switching transients as well as PWM methods [17].

In the three-phase BLDC motor drive with 120° commutation schemes, two phases of the motor conduct at any given time, while the third one remains floating. In [18] and [19], the CM noise analysis of the BLDC motor is performed by considering the excitation of parasitic elements due to the high dv/dt associated with the two conducting phases. However, the CM noise analysis considering the impact of mutual inductance and parasitic capacitance of the floating phase is neglected in the previous study.

The CM filters are incorporated in the drive to limit the impact of CM noise on the rest of the system, especially, communication channels and digital controllers. In [18] and [19], a CM noise mitigation technique using delay compensation for BPWM-operated low-voltage three-phase BLDC drive is reported. Such active methods rely on precision sensing and signal conditioning of CM voltage for mitigation of the noise. Moreover, the proposed active attenuation method is very specific and cannot be used for other PWM schemes. Unlike active filters, passive EMI filters are reliable and cost-effective when designed appropriately as they are realized using passive elements such as inductors, capacitors, and damping resistors [20]. However, a lack of in-depth analysis on the propagation of CM noise and a clear understanding of the source of the noise mislead the design of CM filters for BLDC motor drives.

In three-phase BLDC motor drives, PWM schemes are primarily derived from 120° square-wave commutation, which is widely adopted for low and high power drives [21]. The PWM schemes for BLDC motor drive can be grouped into two classes, viz., (i) unipolar PWM schemes and (ii) bipolar PWM schemes. The emphases of various PWM schemes discussed in the literature have been on minimizing the current or torque ripple, and either reducing or achieving an even distribution of power losses in the drive. By modulating the pulse-width of active devices for the first 60° period (electrical) while continuously turning on the device for the remaining 60° period, it is shown that the torque ripple is minimized compared to bipolar PWM schemes [4], [5], and [2]. A modulation strategy focusing on loss minimization is discussed in [21], [22], and [2]; however, the discussed PWM scheme is intended to improve the speed control performance and loss minimization, to improve the efficiency of the motor

drive system. The CM noise analysis for a BLDC motor drive in context with various PWM schemes is seldom reported. The critical issue of CM voltage is extensively studied for induction motor (IM) drives. Several advanced PWM schemes, such as active zero voltage cancellation PWM [23], have been discussed to reduce the impact of CM voltage on IM motor performance. However, the knowledge of CM voltage analysis for an IM drive cannot be directly translated to a BLDC motor drive due to the differences in motor operation and PWM schemes. Moreover, the larger leakage currents through the ground, which result in CM noise of the BLDC motor drive, induce undesired shaft voltages that lead to circulating bearing current, which in turn accelerates the aging of the motor bearings [24].

As BLDC motor drives are expanding the application area, knowledge of the CM noise in this drive operated at high switching frequencies is lacking in academia and industry. Based on the application, the conducted EMI noise standards have been established by agencies, such as the International Special Committee on Radio Interference (CISPR) and DO-160, to restrict the CM emissions within permissible levels [25]. A CM choke is often installed to keep the leakage currents within limits, for which the CM voltage is considered a key design factor. The volume of the choke can be evaluated by estimating the CM voltage, which helps in designing an optimal filter in terms of size and weight [26]. In [23], it is shown that the volt-seconds applied across a CM choke are PWM dependent and significantly affect the volume of the CM choke. Therefore, an accurate estimate of CM noise as a function of the PWM scheme for BLDC drives is essential to estimate the relative volume of the CM choke. Thus, a comprehensive study of the CM voltage, leakage current, and CM choke requirement for the BLDC drives considering various PWM schemes at higher switching frequencies, are to be explored.

In general, to suppress the detrimental impact of the CM and DM noise on the system's performance, passive EMI filters are widely used as they are simple to design, reliable, and cost-effective. Multi-stage passive EMI filters have gained more interest in recent times as compared to single-stage EMI filters to meet the higher CM and DM noise attenuation requirements along with improved power density [27]. To maintain the CM and DM noise below the desired EMI standard limit, either passive or active EMI filters are adopted. The active EMI filters effectively reduce the EMI filter volume [28], [29], [30]. However, the active EMI filter requires an auxiliary power supply, increases cost, and has some design limitations due to the parasitic parameters of the components such as sensors and the high-frequency loop gain [31]. Hence, passive EMI filters are widely adapted as these filters are simple to design, reliable, and cost-effective. The passive EMI filters (single-stage and two-stage) are comprised of DM choke, CM choke, X-capacitor, and Y-capacitor [27]. The X-capacitor is connected between the lines and hence mitigates the DM

noise [27]. The Y-capacitor is connected between the line and the ground terminals and hence mitigates the CM noise [27]. The maximum permissible leakage current to ground reduces the flexibility in choosing the desired value of Y-capacitor [27]. Moreover, the need for huge capacitors in high DC voltage applications limits the selection of X capacitors [27]. To overcome the above-mentioned design constraints, adequate DM and CM inductance are provided using the DM and CM chokes, respectively, for achieving the desired EMI standard limits. However, due to these DM and CM chokes, the passive EMI filters occupy a substantial volume of the power converter [32]. Therefore, the volume and the printed circuit board (PCB) area of the passive EMI filters have to be minimized to improve the power density of the converter [32].

Hence, the magnetic integration approach of designing integrated chokes is widely explored as an alternative to conventional CM and DM chokes. Employing the integrated choke reduces the volume and occupied PCB area of the passive EMI filters. One way to design the integrated choke is to increase the DM inductance of the conventional toroidal CM choke either by inserting a solenoid [33] or a DM choke [32] or an additional CM choke [34] in the window area of the toroidal CM choke. The integrated choke design presented in [32], [33], and [34] are not suitable for the conventional toroidal CM chokes with lower window area. Moreover, the integrated chokes discussed in [33] and [34] alter the DM flux through the toroidal CM choke and thus increase the risk of magnetic core saturation [35]. Such an arrangement also limits the performance of the CM choke as the number of turns on the outer core reduces because of the lesser diameter of the inner core which improves the DM performance [32].

A new integrated choke structure using an EQ (a cross between E cores and pot cores) core is presented in [36] to improve the DM performance of the conventional CM choke. However, it does not improve the box volume or the PCB area compared to its equivalent conventional passive EMI filter. Multiple stacked configurations of the toroidal CM choke are discussed in [37] to achieve higher DM inductance. However, such stacked configurations increase the box volume and the weight of the EMI filter. The integrated chokes with core structural modifications, to reduce the EMI filter size, discussed in [38], [39], and [40] increase the design complexities and cost as these are not commercially available. Integrated chokes combining EE core and I core are presented in [41] for single-stage and two-stage EMI filters to reduce the filter volume. However, it increases the filter weight and design complexity for two-stage EMI filters. Another integrated choke with improved DM performance is presented in [42]. However, the used CM inductor has a lesser number of turns as compared to the conventional structure using the same wire length. Therefore, it indicates that the integrated choke discussed in [42] requires a less reluctance core

to keep the same CM inductance as the conventional structure and thus increases the core saturation issue. The integrated EE chokes, to achieve both CM and DM suppression, are discussed in [43] and [44]. These structures using the same magnetic material and air-gap length result in a large core size with more CM turns in the limbs of the magnetic structure with air-gap [33]. Thus, a new method of magnetic core arrangement and winding placement needs to be explored for various conditions to improve the performance of the filter with a reduction in the PCB area and filter box volume.

1.3 Motivation and Objectives

The increasing adoption of BLDC motors in high-voltage applications, such as electric vehicles, solar water pumps, and compressors has led to a growing need for efficient motor drive systems. The utilization of WBG power devices, specifically SiC and GaN, presents opportunities for improved power density and efficiency in BLDC motor drives. However, the integration of these advanced technologies in high-voltage applications introduces challenges related to EMI noise.

While previous research has addressed CM noise in low-voltage BLDC drives, there is a lack of in-depth analysis and understanding of CM noise propagation taking into account the impact of the floating phase. Moreover, the existing active CM noise mitigation techniques are often specific to PWM schemes, limiting their applicability. Furthermore, the impact of higher switching frequencies on CM voltage and current in SiC-fed BLDC drives, along with the requirements for CM choke, has not been thoroughly investigated. This knowledge gap poses challenges for the design of effective CM filters to meet EMI standards.

In addition, the CM and DM chokes in the passive EMI filters occupy substantial volume and PCB area, thereby reducing the power density of the converter. Hence, the integrated magnetic approach to design various integrated chokes, that can replace the conventional chokes, with reduced volume and PCB area in the passive EMI filters are to be explored.

Thus, the objective of this thesis is summarized as follows.

1. *Analysis of CM Noise:*

- (a) Conduct a detailed analysis of the propagation of CM noise.
- (b) Identify the sources of CM noise considering the impact of floating phase.
- (c) Development of CM equivalent circuit based on the analysis and experimental studies.

2. *Impact of PWM Schemes on CM Noise:*

- (a) Analyze the CM voltage based on switching functions for various PWM schemes and validate the results experimentally.
- (b) Evaluate the impact of switching frequencies on CM voltage and current for various PWM schemes.
- (c) Examine the requirements for CM choke at higher switching frequencies for various PWM schemes.

3. DC-side Passive Integrated EMI Filters:

- (a) Investigate novel integrated choke designs, aiming to reduce the volume and PCB area of the EMI filters.
- (b) Investigate integrated chokes for both single-stage and two-stage EMI filter volume and PCB area reduction.
- (c) Theoretical estimation and experimental validation for the CM and DM inductance of the designed integrated choke structures.

1.4 Scope of the Thesis and the Organization

The thesis focuses on the CM noise phenomena in a three-phase SiC-fed BLDC motor drive and develops an integrated EMI choke to mitigate the CM and DM noise at the DC side of the inverter with reduced PCB area and filter box volume.

In Chapter 2, an in-depth theoretical analysis of the CM noise in BLDC drive is presented considering two commonly used schemes in 120° conduction mode, (i) six-step commutation (SSC) and (ii) bipolar PWM (BPWM). By Considering the impact of the floating phase, the CM noise in the BLDC drive is modeled through mathematical equations, and the CM equivalent circuit is presented. Finally, a step-by-step design procedure of the CM filter for the BLDC drive is discussed to validate the CM equivalent circuit.

In Chapter 3, the impact of unipolar and bipolar PWM schemes on the CM voltage is investigated. Firstly, a generalized mathematical expression for CM voltage in terms of switching functions is derived and validated through experiments for various PWM schemes in a BLDC drive. Further, the impact of CM voltage on CM current is thoroughly analyzed for 10 kHz and 100 kHz switching frequencies. The CM choke requirements with bipolar and unipolar PWM schemes for different switching frequencies are compared.

In Chapter 4, two novel integrated magnetic chokes for single- and two-stage EMI filters are discussed. Magnetic equivalent circuits for both the proposed integrated

EMI chokes have been presented to estimate the inductance and magnetic flux density of the chokes. The performance of the proposed integrated chokes is experimentally presented and validated on a three-phase SiC inverter-fed BLDC motor drive. The proposed integrated choke for the single-stage EMI filter and the two-stage EMI filter reduces the PCB area and filter box volume when compared to their equivalent conventional EMI filters.

Chapter 5 introduces an ER core-based integrated EMI choke to enhance the DM inductance of conventional EMI chokes with large CM choke sizes. Additionally, a rectangular magnetic core-based integrated EMI choke for a two-stage EMI filter is explored, specifically designed for low-voltage DC-side applications.

In Chapter 6, the thesis concludes by summarizing key findings and insights. The discussion also outlines avenues for future research, providing a comprehensive view of potential extensions and improvements to the study

Chapter 2

Analysis and Mitigation of CM Noise in BLDC Motor Drive

2.1 Introduction

In this chapter, a dummy parasitic impedance (DPI) network is designed to mimic the CM impedance of the BLDC motor. The DPI network plays a vital role in investigating the influence of the floating phase on the CM noise of the BLDC motor drive operating with SSC and BPWM schemes. From the CM noise analysis, with the help of the DPI network, a CM equivalent circuit of a three-phase BLDC drive is developed. The CM filters are designed to mitigate the CM noise by considering the derived CM equivalent circuit, thereby validating the equivalent circuit developed.

2.2 CM Noise Analysis

The lumped parameter model of the BLDC motor is shown in Figure 2.1(a). The circuit model considers the effect of (i) phase-to-ground parasitic capacitors, C_{ag} , C_{bg} and C_{cg} , and (ii) per-phase inductance and back EMF, which are modelled as Z_{mi} and e_i , respectively, where $i = a, b, c$. Two modulation schemes in 120° commutation mode, (i) SSC and (ii) BPWM are considered for CM analysis. The switching action of the active devices results in high dv/dt applied across the phase and ground terminals (v_{ag} , v_{bg} and v_{cg}) of the motor. Such dv/dt excites the motor parasitic capacitances, causing inevitable ground currents, i_{cm_BLdc} .

To understand the propagation of CM noise in the BLDC drive, it is necessary to analyze the currents through C_{ag} , C_{bg} and C_{cg} individually. As the parasitic components are not physical elements, it is impossible to measure the currents through them. Even if i_{cm_BLdc} is measured, the effect of dv/dt on each phase-to-ground parasitic capacitance of the motor and its contribution towards the i_{cm_BLdc} cannot be predicted. Therefore, a DPI network is shown in Figure 2.1(b) to emulate the currents flowing through C_{ag} , C_{bg} , and C_{cg} up to a desired frequency. It is to be noted that the proposed DPI network is used as a platform to understand the propagation of CM currents in the BLDC drive.

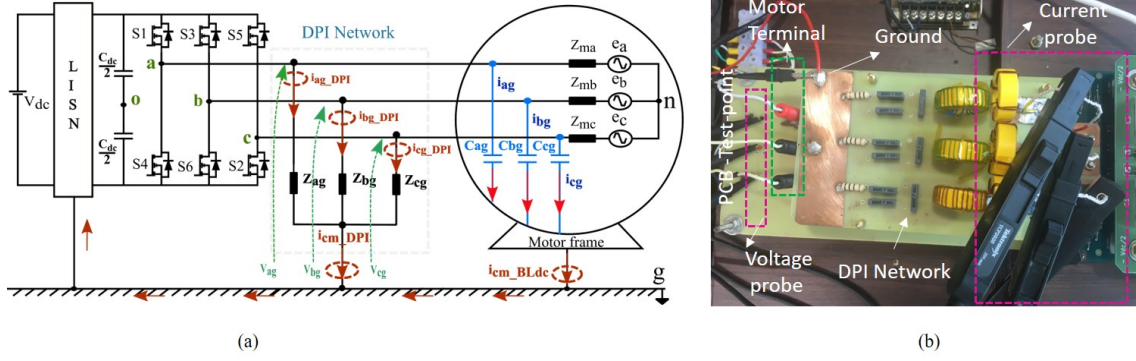


Figure 2.1: (a) Circuit diagram of SiC-based BLDC motor drive with phase-to-ground parasitic capacitances C_{ag} , C_{bg} and C_{cg} and (b) DPI network.

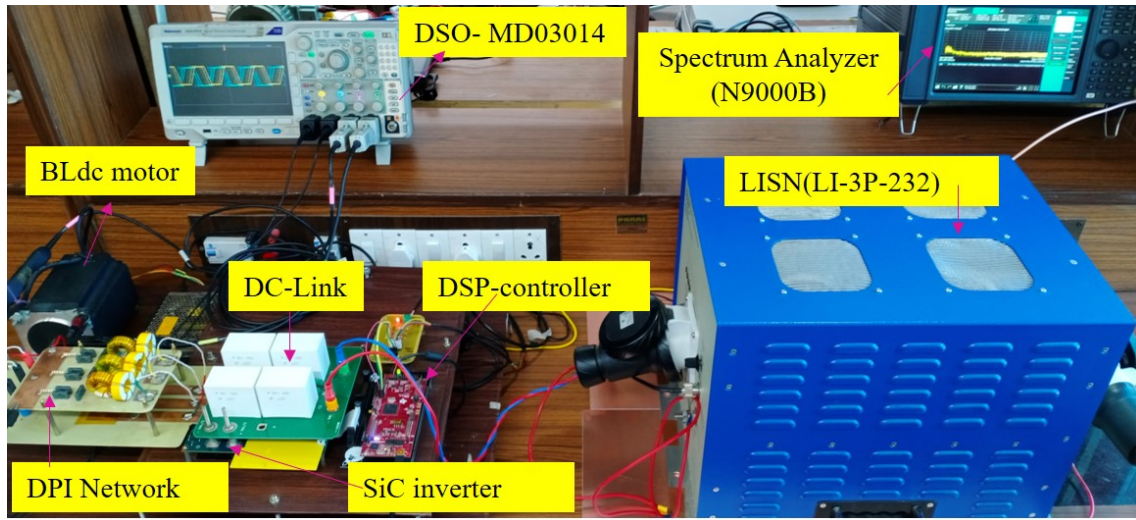


Figure 2.2: experimental setup of a three-phase BLDC drive with DPI network.

2.2.1 Dummy Parasitic Impedance (DPI) Network

A three-phase BLDC motor with the specifications shown in Table 2.1 is connected to a three-phase SiC-based inverter as shown in Figure. 2.2. LISN (LI-3P-232) is connected on the dc side of the inverter to decouple the motor's CM noise and the noise from the dc source. High-performance ac/dc probes (TCP202A) are used to measure the currents flowing from the motor frame to the ground. The current probe is particularly chosen as it has a measurement bandwidth of 50 MHz with desired accuracy between 10 mA and 15 A. The digital signal processor (DSP) TMS320F28379D is used for controlling the motor. The circuit arrangements to measure the motor CM impedance (Z_{CM_BLdc}) using the network analyzer NH4L-IAI2 and the measured impedance are illustrated in Figures 2.3 (a) and (b), respectively. In this paper, each phase of the DPI network is modeled as a fourth-order passive network, as shown in Figure 2.3(c). The DPI network is designed to emulate the CM impedance of the motor to understand the propagation

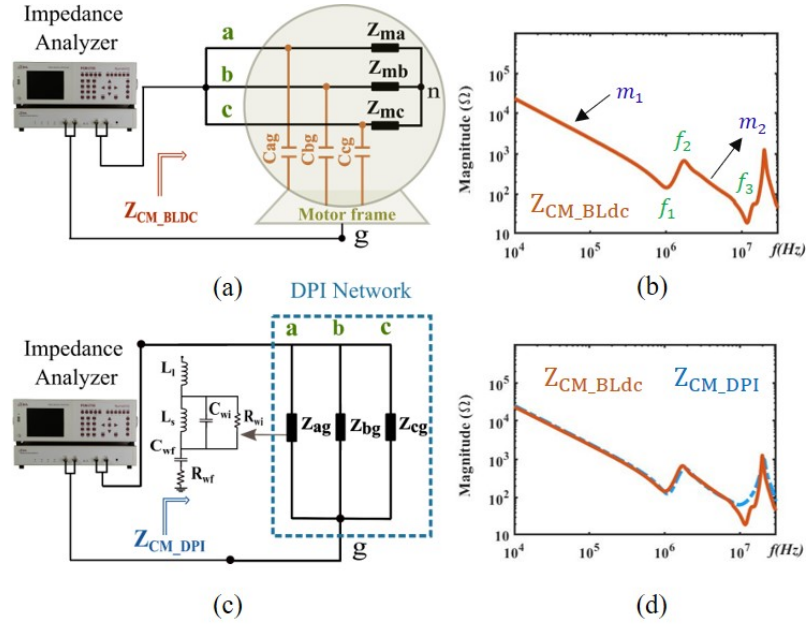


Figure 2.3: (a) Circuit arrangement to measure the CM impedance of the motor, (b) measured CM impedance of the motor, (c) circuit arrangement to measure the impedance of the DPI network, and (d) measured impedance of the DPI network.

Table 2.1: Specifications of BLDC motor

Parameter	Value
Rated dc voltage, V_{dc}	310 V
Rated power, P	1.5 kW
Rated current, I	6.3 A
Nominal Toque, T	4.3 Nm
Rated Speed, N	3500 rpm
Number of poles	8
Torque constant, k_T	0.79 Nm/A
Back EMF constant, k_E	55 V/krpm

of the CM noise in the motor. From the measured impedance profile of Z_{CM_BLdc} , the values of L_l , L_s , R_{wf} , R_{wi} , C_{wf} and C_{wi} parameters of the DPI network are designed as follows:

(a) At medium frequencies, the capacitance C_{wi} defines the slope m_2 in Z_{CM_BLdc} , as shown in Figure 2.3(b). Hence, C_{wi} is calculated from Z_{CM_BLdc} as,

$$C_{wi} = \frac{1}{2\pi f |3Z_{CM_BLdc}|_{atf}}, \text{ for } f_2 \ll f \ll f_3. \quad (2.1)$$

(b) At low frequencies, the combined capacitance $C_{wi} + C_{wf}$ defines the slope m_1 .

Thus, the expression of C_{wf} is written as,

$$C_{wf} = \frac{1}{2\pi f |3Z_{CM_BLdc}|_{atf}} - C_{wi}, \text{ for } f \ll f_1. \quad (2.2)$$

(c) The total capacitance ($C_{wi} + C_{wf}$) and the inductance L_s create a resonance at f_1 , and R_{wf} defines the impedance Z_1 at this resonance frequency f_1 . Thus, L_s and R_{wf} are calculated from f_1 and Z_1 as,

$$L_s = \frac{1}{4\pi^2 f_1^2 (C_{wi} + C_{wf})}, \text{ and} \quad (2.3)$$

$$R_{wf} = |3Z_{CM_BLdc}|_{atf_1}. \quad (2.4)$$

(d) At high frequencies, the inductance L_l creates a resonance with the series combination of C_{wf} and C_{wi} at f_3 as shown in Figure 2.3(b). Thus, L_l is calculated from f_2 using,

$$L_l = \frac{1}{4\pi^2 f_3^2 \left(\frac{C_{wi} C_{wf}}{C_{wi} + C_{wf}} \right)}. \quad (2.5)$$

(e) L_s and C_{wi} create a resonance at f_2 . R_{wi} defines the magnitude of Z_{CM_BLdc} at this frequency and is given as,

$$R_{wi} = |3Z_{CM_BLdc}|_{atf_2}. \quad (2.6)$$

As shown in Figure 2.3(d), the CM impedance of the DPI network (Z_{CM_DPI}) replicates the CM impedance of the BLDC motor, (Z_{CM_BLdc}). From (2.1)-(2.6), the values of L_l , L_s , R_{wf} , R_{wi} , C_{wf} and C_{wi} parameters are estimated to be 4 μ H, 112 μ H, 430 Ω , 2000 Ω , 144 pF, and 80 pF, respectively.

As the DPI network is modelled to predict the behaviour of currents through C_{ag} , C_{bg} and C_{cg} , the total ground current of DPI network (i.e., i_{cm_DPI}) and that of the BLDC motor (i.e., i_{cm_BLdc}) shown in Figure. 2.4(a) should follow the same pattern. The experimental waveforms of i_{cm_DPI} and i_{cm_BLdc} for SSC are shown in Figures. 2.4(b)-(d). From Figure. 2.4(c), it is observed that both i_{cm_BLdc} and i_{cm_DPI} have their positive peaks at the same instant. While in Figure. 2.4(d), both i_{cm_BLdc} and i_{cm_DPI} have their negative peaks at the same instant. From the presented results, it is observed that the measured i_{cm_BLdc} and i_{cm_DPI} are identical; hence, the DPI network is used for further analysis. As shown in Figure. 2.4(e), the frequency spectrum of both i_{cm_BLdc} and i_{cm_DPI} are approximately identical up to 10 MHz. A maximum of 3 dB amplitude difference is seen in the frequencies between 10 kHz and 10 MHz, this would not alter the nature of the currents through the DPI and

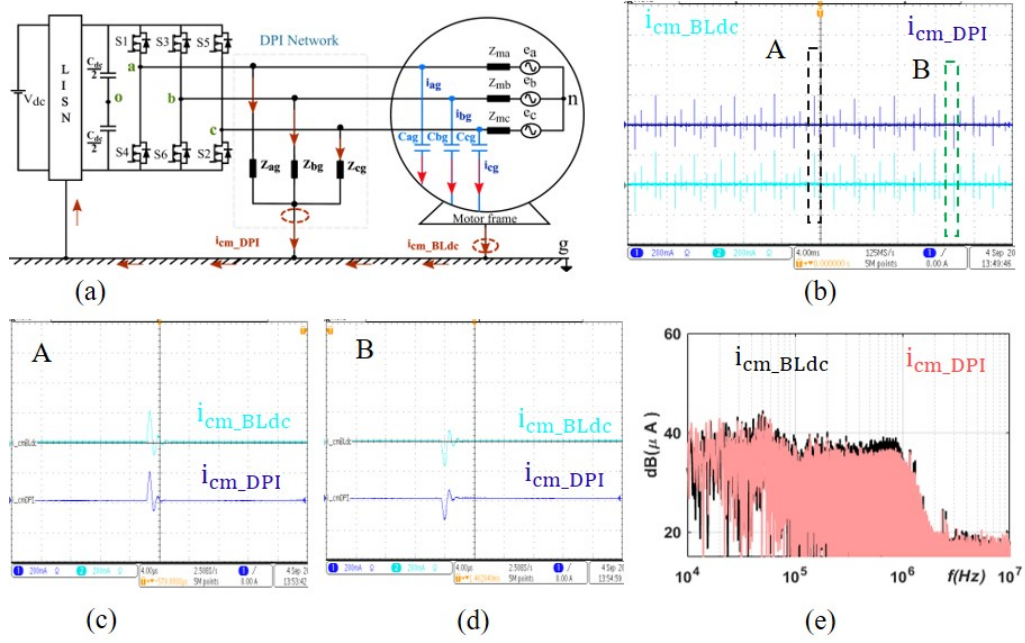


Figure 2.4: (a) Circuit arrangement to measure i_{cm_BLdc} and i_{cm_DPI} , (b) i_{cm_BLdc} and i_{cm_DPI} , (c) enlarged waveform showing positive peaks of i_{cm_BLdc} and i_{cm_DPI} current of 'A' region, (d) enlarged waveform showing negative peaks of i_{cm_BLdc} and i_{cm_DPI} current of 'B' region, and (e) frequency spectrum of i_{cm_BLdc} and i_{cm_DPI} .

the motor ground parasitic capacitances as they are excited by the same source (i.e., same dv/dt).

2.2.2 Six-Step Commutation (SSC)

To understand the propagation of CM currents in each phase of the SSC-operated BLDC drive, the DPI network is connected along with the motor, as shown in Figure. 2.5(a). In a fundamental cycle of the SSC, each phase undergoes two conduction and two floating periods [45]. For instance, the conduction and floating periods of phase c during the positive half cycle of the fundamental period are illustrated in Figure. 2.5(b). Though the floating period is divided into commutation and back EMF periods, the high dv/dt during the commutation period dominates the transition and contributes to the CM noise. As shown in Figure. 2.5(b), the commutation instances t_1 and t_2 contributing to the CM noise are analyzed further. Following are the inferences from the experimental results:

1. The dv/dt in v_{cg} at t_1 and t_2 causes disturbances in v_{ag} and v_{bg} , as shown in Figures. 2.5(c) and (e). In particular, the noncommutating phases experience an opposite transition as that of the commutating phase. It can be understood that the commutations in any one of the phases is reflected as voltage oscillations in the remaining phases due to v_{og} fluctuation, thereby, exciting all the phases-to-ground parasitic capacitances (i.e., C_{ag} , C_{bg} and C_{cg}).

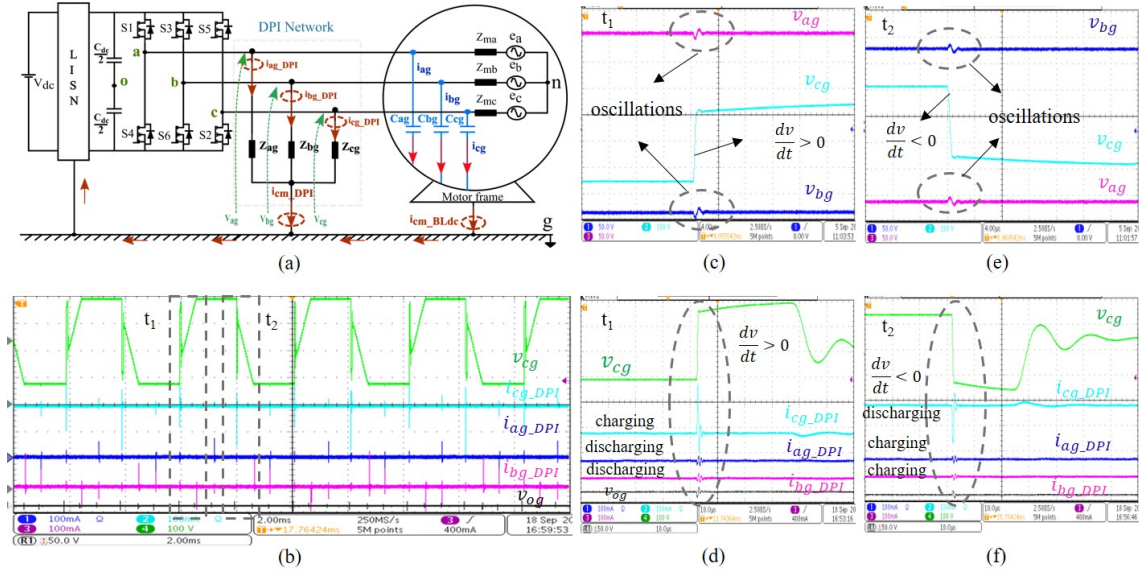


Figure 2.5: (a) Three-phase BLDC drive with DPI network for analyzing the CM currents, (b) v_{cg} along with the currents through each phase-to-ground of DPI network (i.e., i_{ag_DPI} , i_{bg_DPI} and i_{cg_DPI}), (c) enlarged waveforms of v_{ag} , v_{bg} , v_{cg} at t_1 , (d) enlarged waveforms of v_{cg} , i_{ag_DPI} , i_{bg_DPI} and i_{cg_DPI} at t_1 , (e) enlarged waveforms v_{ag} , v_{bg} , v_{cg} at t_2 , and (f) enlarged waveforms of v_{cg} , i_{ag_DPI} , i_{bg_DPI} and i_{cg_DPI} at t_2 .

2. At t_1 , the currents i_{ag_DPI} , i_{bg_DPI} and i_{cg_DPI} during commutation in phase c , are shown in Figure. 2.5(d). At this instant, v_{cg} has positive dv/dt while v_{ag} and v_{bg} experience negative dv/dt as explained earlier. Therefore, i_{cg_DPI} through Z_{cg} is a charging current that flows in the direction towards the ground, while the currents i_{ag_DPI} and i_{bg_DPI} are discharging currents and flow away from the ground.
3. It can be observed from Figure 2.5(f) that the negative dv/dt in v_{cg} drives i_{cg_DPI} in phase c of the DPI network. The positive dv/dt induced in v_{ag} and v_{bg} causes i_{ag_DPI} and i_{bg_DPI} in phases a and b of the DPI network.

The i_{ag_DPI} , i_{bg_DPI} and i_{cg_DPI} are measured to provide an insight on the nature of i_{ag} , i_{bg} and i_{cg} of the motor, respectively. Therefore, it can be concluded that all three phases of the BLDC motor contribute to the CM noise in the case of SSC. The direction of currents in each phase is dictated by the direction of dv/dt .

2.2.3 Bipolar Pulsewidth Modulation (BPWM)

In BPWM-operated BLDC drive, the high-side switches (S_1 , S_3 and S_5) and the low-side switches (S_4 , S_6 and S_2) are controlled using PWM signals [45]. Similar to the SSC, two out of the three phases of the motor are conducting, while the third phase remains floating in BPWM. Unlike the SSC, the pole of the conducting phase alternates between $\pm V_{dc}/2$ with respect to 'o' at the switching frequency (10 kHz)

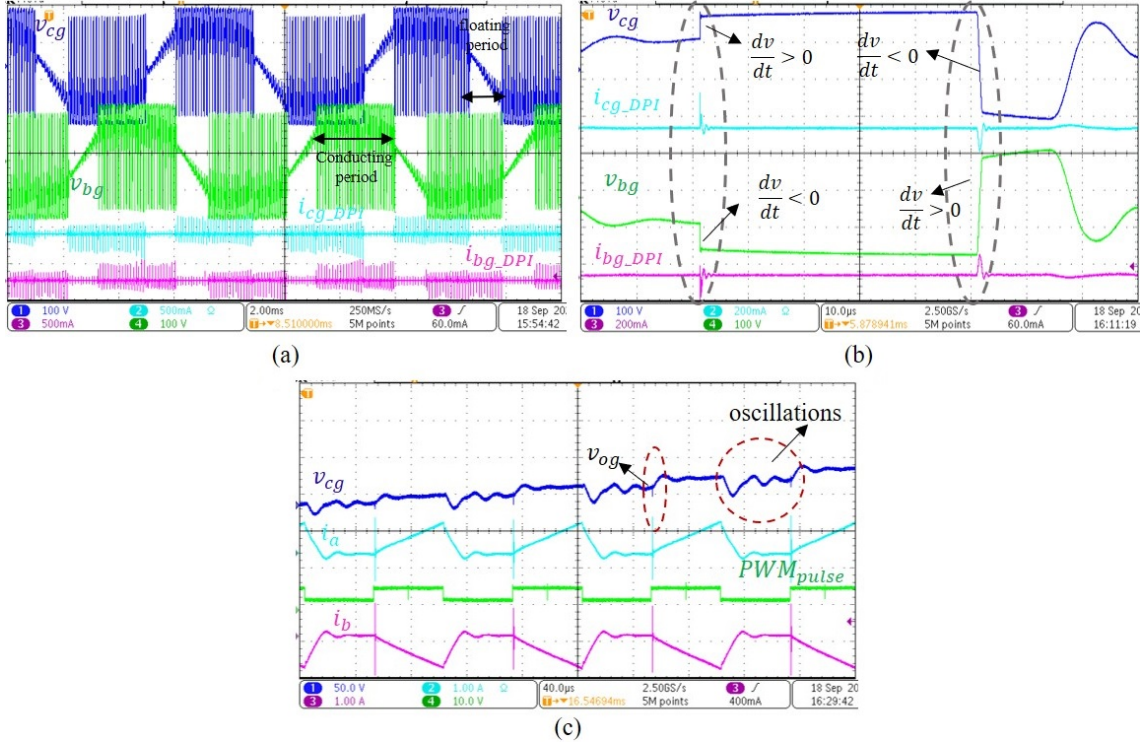


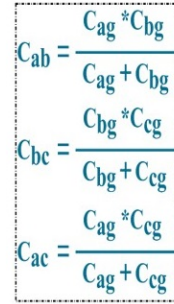
Figure 2.6: Three-phase BLDC drive with DPI network for analyzing the CM currents with BPWM. (a) v_{bg} and v_{cg} voltage waveforms indicating floating and conduction periods in v_{cg} along with corresponding DPI network currents i_{bg_DPI} and i_{cg_DPI} , (b) enlarged waveforms of v_{bg} and v_{cg} showing positive and negative dv/dt instances in conduction period along with i_{bg_DPI} and i_{cg_DPI} currents at that instances, and (c) indicating the effect of mutual inductance and capacitance, v_{og} and back EMF on v_{cg} in floating period along with i_a and i_b phase currents.

in BPWM. The dv/dt in the conduction period coupled with the parasitic elements of the motor causes undesirable i_{cm_BLdc} .

Impact of conducting phase on CM noise with BPWM:

The dv/dt in the conducting phase excites the corresponding phase-to-ground parasitic capacitance. In an ideal condition, the charging and discharging currents through the ground should become canceled because of complementary pole voltages. As discussed in [18], due to non-idealities in the turn-on and turn-off transitions of the complementary switching devices, and propagation delays from the gate drivers, the resultant ground current will not be zero. The effect of dv/dt in the conducting phase of the motor in the BPWM case is captured in Figure. 2.6(a) and the following are the inferences.

1. The waveforms of v_{bg} , v_{cg} , i_{bg_DPI} and i_{cg_DPI} are illustrated in Figure. 2.6(a). It is observed that in the conduction period of v_{bg} , due to the dv/dt incurred through PWM switching, a nonzero i_{bg_DPI} flows through Z_{bg} of the DPI network. A similar observation is made for phase c .



2. The enlarged waveforms of v_{bg} and v_{cg} during the conduction period are shown in Figure. 2.6(b). The i_{bg_DPI} is seen at the instances where $dv/dt \neq 0$ during the conduction period of v_{bg} . A similar pattern is observed in i_{cg_DPI} with a finite dv/dt in v_{cg} , as shown in Figure. 2.6(b).

As discussed in Chapter 2.2.2, the floating period of the BLDC motor is divided into commutation and back EMF periods. The analysis of CM noise during the commutation period in the BPWM case is similar to that of the SSC, i.e., dv/dt induced in the floating phase to ground voltage contributes to the i_{cm_BLdc} . However, unlike the back EMF period of SSC, the CM noise during the back EMF period of the BPWM case cannot be neglected. The factors contributing to the CM currents during the back EMF period are (i) the mutual inductance between the floating phase and conducting phases and (ii) the phase-to-ground parasitic capacitance. To understand the impact of mutual inductance during the back EMF period, the phase-to-ground voltage of the floating phase is derived from the simplified circuit shown in Figure. 2.7(a). By applying Kirchhoff's voltage law (KVL) to loop 1 connecting the nodes $g-o-a-n-c-g$ and loop 2 connecting the nodes $g-o-b-n-c-g$, the voltage v'_{ca} is obtained as,

$$v'_{cg} = (L_{bc} - L_{ac}) \frac{di'_{ab}}{dt} + v_{og} + e_c \quad (2.7)$$

where L_{ac} and L_{bc} are the mutual inductances between phases c and a , and phases c and b , respectively. The self-inductance and the mutual-inductance are a function of the angular position of the rotor, θ_r [46]-[47]. Considering the effect of θ_r the mutual inductances of L_{bc} and L_{ac} are expressed as,

$$L_{bc} = -M_s - L_g \cos(2(\theta_r + \frac{\pi}{6} - \frac{2\pi}{3})) \quad (2.8)$$

$$L_{ac} = -M_s - L_g \cos(2(\theta_r + \frac{\pi}{6} + \frac{2\pi}{3})) \quad (2.9)$$

substituting the value of L_{bc} and L_{ac} in (2.7), the simplified expression for v'_{cg} is expressed as,

$$v'_{cg} = \sqrt{3}L_g \sin(2\theta_r + (\pi/3)) \frac{di'_{ab}}{dt} + v_{og} + e_c \quad (2.10)$$

where L_g is the fluctuation in inductance with change in θ_r . From (2.10), i'_{ab} and θ_r influence the floating phase voltage and it is responsible for the CM noise during the back EMF period, as shown in Figure. 2.6(c).

To analyze the impact of phase-to-ground parasitic capacitance on the CM noise, the considered equivalent circuit of the BLDC motor when phase c is floating, is shown in Figure. 2.7(b). By applying KVL to loop 1 connecting the nodes g - c - b - o - g and loop 2 connecting the nodes g - c - a - o - g , the voltage v''_{cg} is derived as,

$$v''_{cg} = v_{og} + \frac{1}{2}(v_{C_{bc}} - v_{C_{ac}}) \quad (2.11)$$

where $v_{C_{bc}}$ and $v_{C_{ac}}$ are the voltages across C_{bc} and C_{ac} , respectively, and can be written as,

$$v_{C_{bc}} = \frac{1}{C_{bc}} \int i_{c1} dt \text{ and } v_{C_{ac}} = \frac{1}{C_{ac}} \int i_{c1} dt. \quad (2.12)$$

Substituting (2.12) into (2.11), v''_{cg} can be simplified as,

$$v''_{cg} = v_{og} + \frac{1}{2} \left(\frac{C_{ac} - C_{bc}}{C_{ac} * C_{bc}} \right) \int i_{c1} dt \quad (2.13)$$

From (2.13), it can be understood that the high dv/dt oscillations in the back EMF period are because of the excitation of phase-to-ground capacitors (that act as phase-to-phase capacitors) during switching.

Thus, (2.7) and (2.13) provide insight on the two components of floating phase

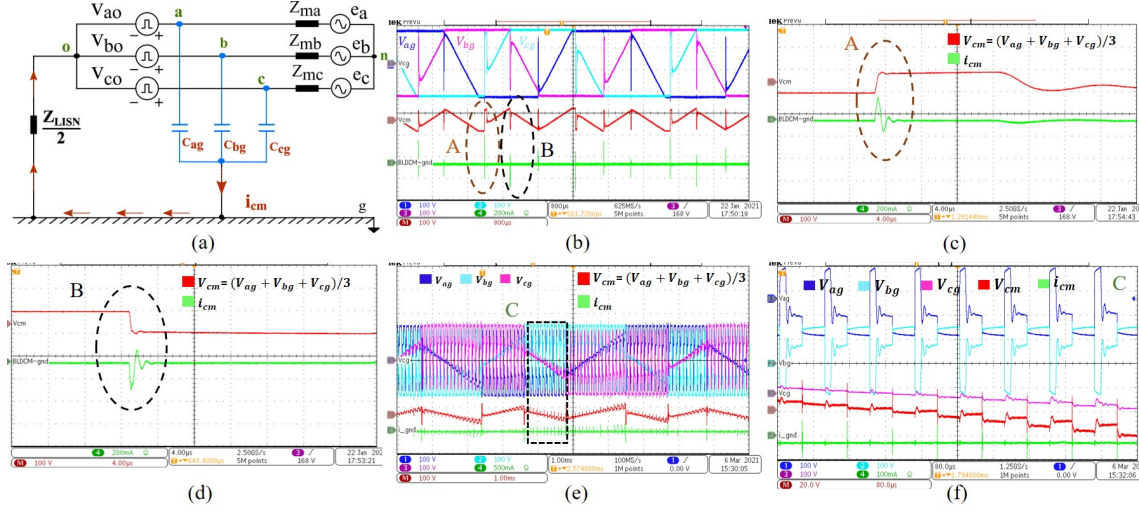


Figure 2.8: Experimental waveform of v_{cm} and i_{cm_BLdc} for SSC and BPWM. (a) Three-phase CM equivalent circuit for both SSC and BPWM, (b) waveforms of (v_{cm}) and (i_{cm_BLdc}) along with phase-to-ground voltages (v_{ag} , v_{bg} , v_{cg}), (c) enlarged waveform showing the charging nature of i_{cm_BLdc} due to positive dv/dt in v_{cm} , (d) enlarged waveform showing the discharging nature of i_{cm_BLdc} due to negative dv/dt in v_{cm} , (e) (v_{cm}) and (i_{cm_BLdc}) profiles along with phase-to-ground voltages (v_{ag} , v_{bg} , v_{cg}), and (f) enlarged waveforms of C region showing v_{ag} , v_{bg} , v_{cg} , v_{cm} and i_{cm} .

voltage due to mutual inductance v'_{cg} and capacitances between the phases v''_{cg} of the motor. Hence, the resultant floating phase voltage consists of (i) switching frequency component due to the mutual inductance and oscillation due to the capacitance between the phases, (ii) oscillations corresponding to v_{og} , and (iii) back EMF (e_c) component, as shown in Figure. 2.6(c). The waveforms of i_{ag_DPI} , i_{bg_DPI} and i_{cg_DPI} when v_{cg} is floating is shown in Figure 2.7(c). It is observed that all three phase-to-ground impedances of the DPI network are energized during this instant. Therefore, it can be concluded that similar to the SSC case, all three three-phases contribute to the CM noise in the BPWM-operated BLDC drive.

2.2.4 CM Equivalent Circuit

Considering the experimental data and the presented analysis, the CM equivalent circuit for the BLDC motor is proposed, as shown in the Figure. 2.8(a). As discussed in Chapters 2.2.2 and 2.2.3, the parasitic capacitors between all phases and ground become excited simultaneously due to the dv/dt in each phase. Therefore, the CM equivalent circuit must consist of all pole voltages and phase-to-ground parasitic capacitances of the motor. Hence, i_{cm_BLdc} can be written as,

$$\vec{i}_{cm} = \vec{i}_{ag} + \vec{i}_{bg} + \vec{i}_{cg} \quad (2.14)$$

Since the time varying nature of v_{ag} , v_{bg} and v_{cg} causes the parasitic currents, (2.14) can be rewritten as,

$$\vec{i}_{cm} = \frac{\vec{v}_{ag}}{Z_{C_{ag}}} + \frac{\vec{v}_{bg}}{Z_{C_{bg}}} + \frac{\vec{v}_{cg}}{Z_{C_{cg}}} \quad (2.15)$$

where $Z_{C_{ag}} = 1/\omega C_{ag}$, $Z_{C_{bg}} = 1/\omega C_{bg}$ and $Z_{C_{cg}} = 1/\omega C_{cg}$.

If v_{cm} is the total CM voltage of a three-phase BLDC motor drive, the i_{cm_BLdc} in (2.15) can be modified as,

$$\frac{\vec{v}_{cm}}{Z_{cm_BLdc}} = \frac{\vec{v}_{ag}}{Z_{C_{ag}}} + \frac{\vec{v}_{bg}}{Z_{C_{bg}}} + \frac{\vec{v}_{cg}}{Z_{C_{cg}}} \quad (2.16)$$

Considering the symmetry of the drive, the per-phase CM impedance is equal to thrice the Z_{CM_BLdc} , therefore, v_{cm} is simplified as,

$$\vec{v}_{cm} = \frac{\vec{v}_{ag} + \vec{v}_{bg} + \vec{v}_{cg}}{3} \quad (2.17)$$

The measured v_{ag} , v_{bg} and v_{cg} along with the v_{cm} in case of SSC are shown in Figure. 2.8(b). It can be observed from the figure that only the floating periods of v_{ag} , v_{bg} and v_{cg} appear in v_{cm} and dv/dt , which results in i_{cm_BLdc} only appearing during the commutation intervals. Also, the charging and discharging nature of i_{cm_BLdc} due to positive and negative dv/dt in v_{cm} are shown in Figures. 2.8(c) and (d), respectively. The experimental results confirm the analysis that the commutations during the floating period are responsible for i_{cm_BLdc} in SSC-operated BLDC drives. The waveforms of v_{cm} and i_{cm_BLdc} for the BPWM case are shown in Figure. 2.8(e). Unlike SSC, in BPWM due to the effect of commutation, mutual inductance, and parasitic capacitance, the high dv/dt exist in the floating period (i.e., both commutation and back EMF period) of v_{ag} , v_{bg} and v_{cg} . The effect of this high dv/dt in floating period of v_{ag} , v_{bg} and v_{cg} is seen in v_{cm} , which results in i_{cm_BLdc} .

The v_{cm} and i_{cm_BLdc} waveforms are shown in Figure. 2.8(f). The experimental

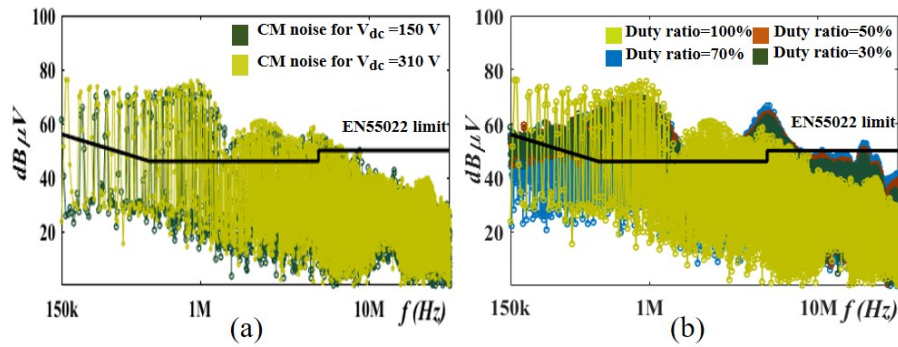


Figure 2.9: Bare CM noise for (a) SSC case with 150 V and 310 V dc link voltages and (b) BPWM case with a duty ratio of 30%, 50%, 70%, and 100%.

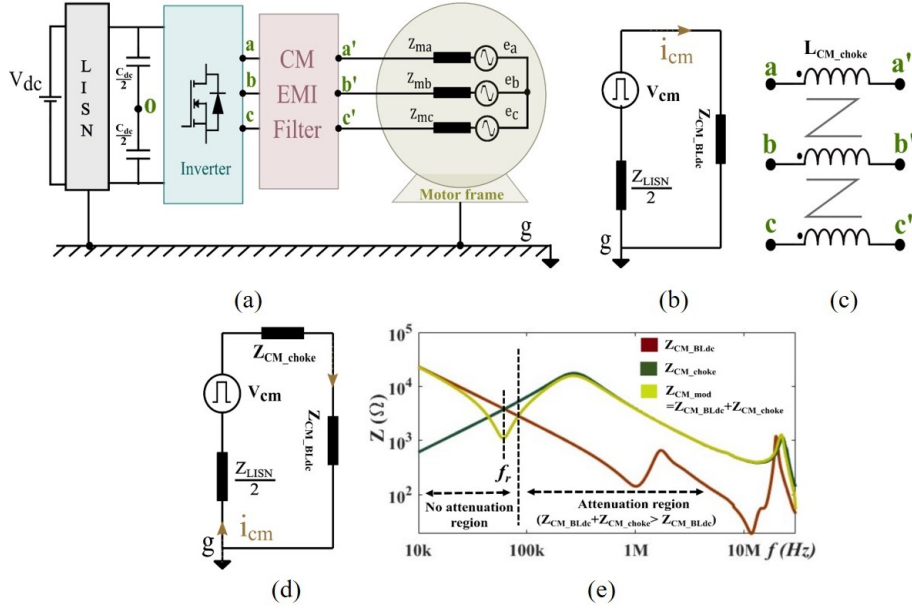


Figure 2.10: (a) Block diagram of three-phase BLDC drive with EMI filter, (b) simplified CM noise model for BLDC motor, (c) CM choke configuration, (d) simplified CM circuit with CM choke, and (e) CM impedance profile of motor (Z_{CM_BLdc}), CM choke (Z_{CM_choke}) and motor CM choke (Z_{CM_mod}).

results confirm the analysis that both the commutation and back EMF periods with high dv/dt are responsible for i_{cm_BLdc} in the BPWM-operated BLDC drive.

Considering the above analysis, the required filters are discussed further to keep the CM noise within the acceptable limits suggested by EN550022 standards [48].

2.3 CM Noise Mitigation with CM Choke and CM LC Filter

In BLDC motor drives, it is generally believed that the ground current flows through only two phases at an instant. Therefore, the active compensation techniques were explored [18], ignoring the passive filtering techniques due to their disadvantage of under usage for two phase-to-ground excitations in a three-phase system. However, the presented analysis validates the current flow to the ground through all three phases for a three-phase BLDC drive. So, the passive CM filtration techniques are proven to be the feasible techniques for three-phase BLDC drive, thus avoiding the complexity involved in active filtration techniques. Hence, further the (i) CM choke and (ii) LC filter is designed to validate the passive CM attenuation methods to reduce the CM noise.

The dc link voltage of the BLDC motor drive is supplied either from a fixed or regulated voltage source depending on the application. The SSC is employed in

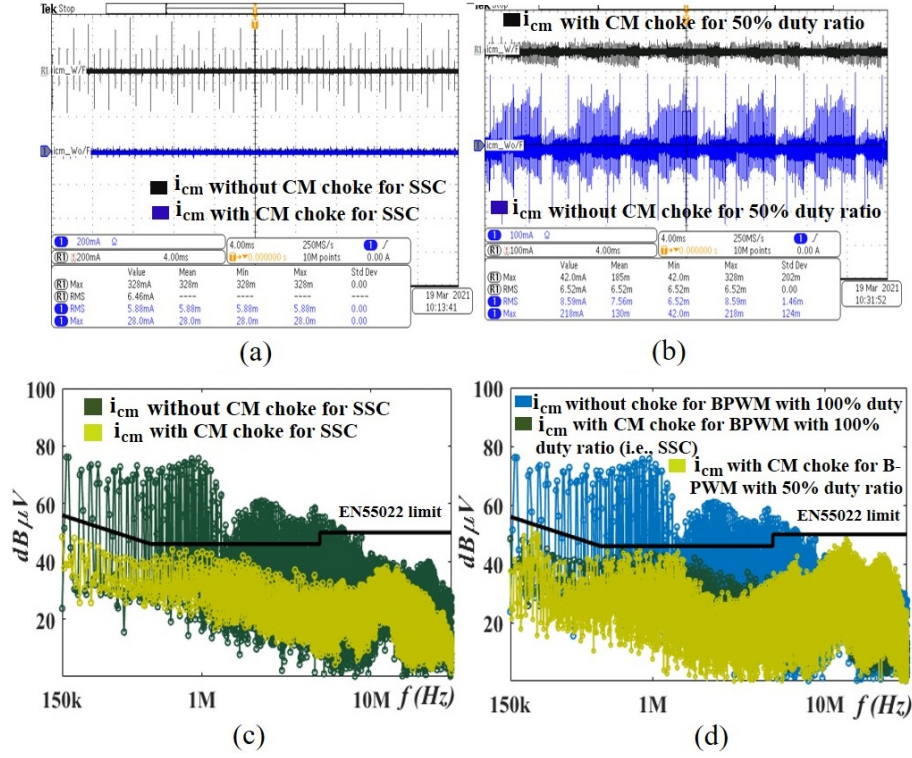


Figure 2.11: Experimental results for SSC - dc voltage = 310 V, speed = 3500 rpm and torque = 0.316 Nm, and BPWM - dc voltage = 310 V, speed = 1860 rpm, torque = 0.28 Nm, and duty = 50%: (a) Time domain profile of $i_{cm-BLdc}$ without and with CM choke for SSC, (b) time-domain profile of $i_{cm-BLdc}$ without and with CM choke for BPWM with 50% duty ratio, (c) frequency domain profile without and with CM choke for SSC, and (d) frequency domain profile without CM choke for BPWM with 100% duty ratio, with CM choke for BPWM with 100% and 50% duty ratio.

applications where the dc link voltage of the drive is regulated by a front-end converter to control the speed and torque of the motor, for instance, in solar water pumps [10, 49]. Therefore, the CM noise in SSC case is measured with 150 V and 310 V dc link voltages, as shown in the Figure. 2.9(a). Among the two considered dc link voltages, 310 V is observed to be the worst-case scenario and is considered for filter design. Similarly, the BPWM-operated BLDC motor drive will be fed with a fixed dc link voltage, while the speed and torque are regulated by controlling the duty ratio. The CM noise of the drive in the BPWM case is obtained with different duty ratios (viz., 30%, 50%, 70%, and 100%) as shown in Figure. 2.9(b). It can be observed from the figure that with an increase in the duty ratio, the CM noise increases, attaining a maximum when the duty ratio equals 100% case. As shown in Figures. 2.9(a) and (b), the CM noises in the BLDC drive in both SSC and BPWM cases do not comply with EN550022 standards. To meet the standards, a CM filter is placed between the inverter and motor terminals, as shown in Figure. 2.10(a). Two CM filter configurations, viz., (i) CM choke and (ii) LC filter, are studied in

this paper. The attenuation requirements at any specific frequency is given by

$$\begin{aligned} Attn_{reqcm}(f)[dB\mu V] &= A_{(cm,max)}[dB\mu V] \\ &\quad - Limit_{EN55022(AVG.)} + 6dB\mu V(margin) \end{aligned} \quad (2.18)$$

From (2.18), the attenuation required, excluding the 6 dB μ V margin, is calculated as 22.238 dB at 160 kHz by considering the frequency spectrum at 310 V (worst-case scenario) as shown in Figure. 2.9(a).

2.3.1 CM Noise Mitigation with CM Choke

A simplified single-phase CM equivalent circuit, CM choke configuration, and simplified equivalent circuit with CM choke are illustrated in Figures. 2.10(b), (c), and (d), respectively. From Figures. 2.10(b) and (d), the attenuation offered by the CM choke is expressed as

$$Attn_{choke} = 20 \log \left(1 + \frac{Z_{CM_choke}}{Z_{CM_BLdc} + \frac{Z_{LISN}}{2}} \right) \quad (2.19)$$

From (2.19), it can be observed that with an increase in the impedance of the CM choke, the filter attenuation increases. Therefore, the CM choke should be designed such that,

$$Z_{CM_choke} + Z_{CM_BLdc} \gg Z_{CM_BLdc} \quad (2.20)$$

Design guidelines for CM choke

The following steps are suggested for CM choke design in BLDC drives.

Step 1: From the Z_{CM_BLdc} plot shown in Figure. 2.10(e), the resonant frequency (f_r) is selected such that it is one-third of the highest frequency component. In the figure, the highest frequency component is 160 kHz, therefore, f_r is fixed as 53.33 kHz. Selecting f_r less than one-third of the highest frequency component favors the attenuation at the expense of choke size.

Step 2: The impedance of CM choke is calculated at f_r as,

$$Z_{CM_choke} = Z_{CM_BLdc} \big|_{f=f_r} \quad (2.21)$$

Step 3: The inductance of CM choke is obtained from Z_{CM_BLdc} as,

$$L_{CM_choke} = \frac{Z_{CM_choke}}{2 \times \pi \times f_r} = \frac{Z_{CM_BLdc} \big|_{f=f_r}}{2 \times \pi \times f_r} \quad (2.22)$$

Following the design guidelines, a CM choke of 10 mH is required to attenuate

the CM noise and meet the EN550022 standards. The modified CM impedance of the BLDC motor with CM choke, Z_{CM_mod} , is shown in Figure. 2.10(e). It can be observed from this figure that the designed Z_{CM_mod} resonates at f_r and its impedance increases for frequencies beyond f_r . The measured i_{cm} profiles with and without the CM choke are presented in Figure. 2.11. Following are some of the inferences.

1. The i_{cm} profiles with and without CM choke for the SSC case are presented in Figure. 2.11(a). It can be seen from this figure that the peak of i_{cm} is reduced by 300 mA owing to the significant reduction in CM noise.
2. The i_{cm} profiles with and without CM choke for BPWM at 50% duty cycle case are presented in Figure. 2.11(b). In this case, it is observed that the i_{cm} peak has reduced by 176 mA.
3. The frequency spectrum of i_{cm} is shown in Figure. 2.11(c) for SSC case, and in Figure. 2.11(d) for BPWM with 50% and 100% duty ratios. The designed

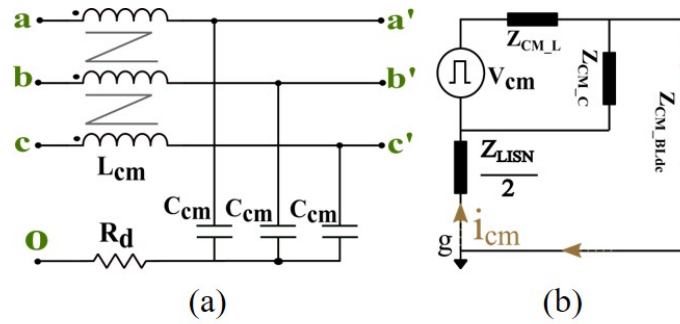


Figure 2.12: (a) LC circuit configuration and (b) simplified CM equivalent circuit with LC circuit configuration.

CM choke has successfully confined the CM noise within the EN55022 limit.

Although CM choke has a simple construction, its large inductance requirement limits its usage in applications having volume constraints.

2.3.2 CM Noise Mitigation with CM LC Filter

The use of LC filters in three-phase drives is widely explored in the literature. Extending the same design procedure to the BLDC drive operated with 120° conduction mode might mislead the design value. It also results in one of the winding of the CM choke/capacitor underutilized at any given point of time due to the assumption that the CM current through the floating phase is zero[18]. With the presented analysis in Chapters 2.2.4, it is clear that all three phases contribute

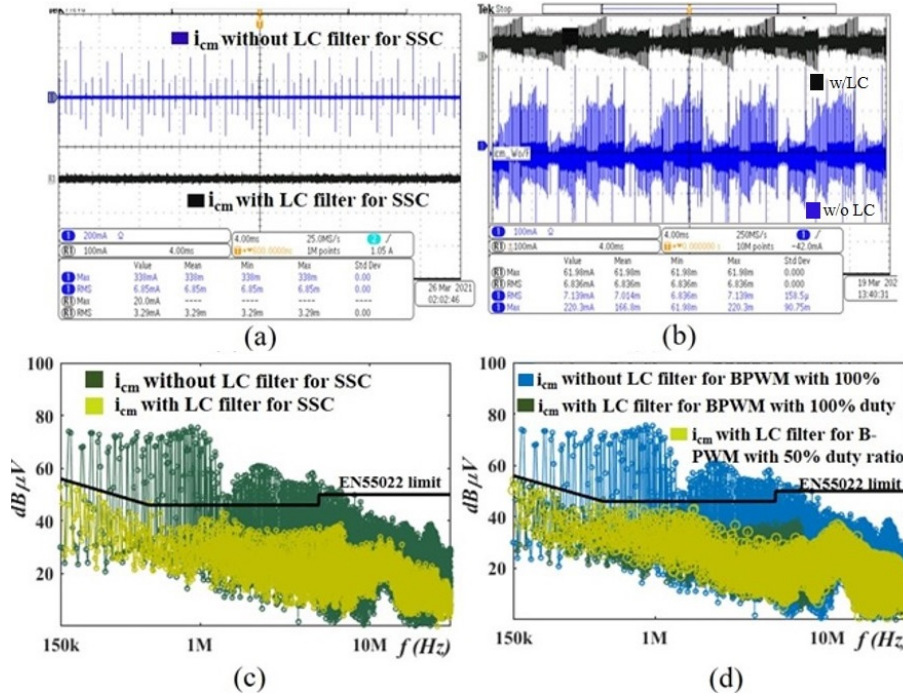


Figure 2.13: Experimental results for SSC - dc voltage = 310 V, speed = 3500 rpm and torque = 0.316 Nm, and BPWM - dc voltage = 310 V, speed = 1860 rpm, torque = 0.28 Nm, and duty = 50%: (a) Time domain profile of i_{cm_BLdc} without and with LC filter for SSC (b) time-domain profile of i_{cm_BLdc} without and with LC filter for BPWM with 50% duty ratio, (c) frequency domain profile without and with LC filter for SSC, and (d) frequency domain profile without LC filter for BPWM with 100% duty ratio, with LC filter for BPWM with 100% and 50% duty ratio.

to CM currents and therefore, the design procedure of the CM filter can be directly adapted from IM drives[50].

The connection and configuration of the LC filter are shown in Figure. 2.12(a), and a simplified single-phase CM equivalent circuit with an LC filter is shown in Figure. 2.12(b). Since the Z_{CM_C} branch is capacitive, it offers less impedance to the noise compared to the combined impedances of the motor and LISN. Therefore, most of the i_{cm_BLdc} is diverted to Z_{CM_C} branch, thereby, reducing the ground current through the motor.

Design of CM LC filter

The following guidelines are suggested for the design of the LC filter.

Step 1: The cut-off frequency (f_o) of the LC filter is calculated for the required attenuation ($Attn_{reqcm}$) as,

$$f_o \leq \frac{f}{10(Attn_{reqcm}/40)} \quad (2.23)$$

where f is the highest frequency component to be attenuated i.e., $f = 160$ kHz.

Step 2: After calculating f_o , C_{cm} and L_{cm} are obtained as [50],

$$L_{cm} = \frac{1}{4\pi^2 f_o^2 (3C_{cm})} \quad (2.24)$$

Step 3: The damping resistance, R_d , is chosen from the damping ratio, ζ , as [20],

$$R_d = 2\zeta \left(\sqrt{\frac{L_{cm}}{3C_{cm}}} \right). \quad (2.25)$$

For the required attenuation of 22.238 dB with SSC, the cut-off frequency, f_o , calculated using (2.23) is 44.48 kHz. The resultant filter parameters are $3C_{cm} = 4$ nF, $L_{cm} = 3.2$ mH and $R_d = 75 \Omega$. The measured i_{cm} profiles with and without the LC filter are presented in Figure. 2.13. Following are some of the inferences.

1. The i_{cm} profiles with and without LC filter for SSC case are presented in Figure. 2.13(a). It can be seen from this figure that the peak of i_{cm} is reduced by 318 mA owing to the significant reduction in CM noise.
2. The i_{cm} profiles with and without LC filter for BPWM at 50% duty cycle case are presented in Figure. 2.13(b). In this case, it is observed that the i_{cm} peak has reduced by 158 mA.
3. The frequency spectrum of i_{cm} is shown in Figure. 2.13(c) for SSC case, and in Figure. 2.13(d) for BPWM with 50% and 100% duty ratios. The designed LC filter has successfully confined the CM noise within the EN55022 limit.

2.4 Conclusion

Three-phase BLDC motor drives are becoming popular in high-voltage applications such as electric vehicles and solar water pumps. In this paper, the propagation of CM noise in the BLDC motor has been discussed with mathematical analysis and experimental validation. Two widely used modulation schemes for the BLDC motor are studied; (i) SSC and (ii) BPWM. A DPI network is designed to emulate the motor phase-to-ground parasitic capacitances and provide insights on each phase-to-ground current that contributes to the CM noise in the motor. From the analysis, a generalized CM equivalent circuit is proposed including all the three-phase-to-ground parasitic capacitances of the motor. The provided analysis clarifies the misconception that only two phases contribute to the CM current in the BLDC motor. Additionally, it is shown that the CM noise in the 120° modulation schemes is predominantly due to the floating phase of the motor, especially in high-voltage SiC-based BLDC drives. Finally, the design of the CM choke and LC

filter (passive filter schemes) is presented to attenuate the CM noise in the BLDC motor drive.

Chapter 3

Impact of PWM Schemes on CM Voltage, CM Current, and CM Choke for Three-Phase BLDC Motor Drive

3.1 Introduction

In this chapter, a comprehensive study of the CM voltage, leakage current, and CM choke requirement for the BLDC drives considering various PWM schemes is analyzed in detail. The above-mentioned analysis is performed for the most commonly adopted PWM schemes namely, H-PWM-L-ON, PWM-ON, C-BPWM, and M-BPWM. For the BLDC motor operating with these PWM schemes, the analytically estimated CM voltage in terms of switching functions is experimentally validated. Furthermore, the impact of switching frequency on the volume of the CM choke with various PWM schemes is discussed in detail.

3.2 PWM Schemes for Three-Phase BLDC Drive

A three-phase BLDC motor drive consists of a three-phase inverter and a BLDC motor, as shown in Figure 3.1. Six active devices, S_{iu} and S_{il} , $i = \{a, b, c\}$, form three phase legs of the inverter, which are connected to the three phases of the BLDC motor. The high-side (HS) switches (S_{au} , S_{bu} , S_{cu}) and low-side (LS) switches (S_{al} , S_{bl} , S_{cl}) are modulated to impose the desired voltages across the motor terminals. The gate signals are generated as per the sector information obtained from the hall sensors (H_a , H_b , H_c), as shown in Figure 3.1.

As per the sector information, the two motor phase windings are excited simultaneously, known as conducting phases. When the HS and LS switches of a particular phase are turned off, the corresponding phase is said to be the floating phase. Three-phase BLDC motor drives use a six-step commutation (SSC) scheme to control the speed and rotational direction with variable DC-link voltage applications.

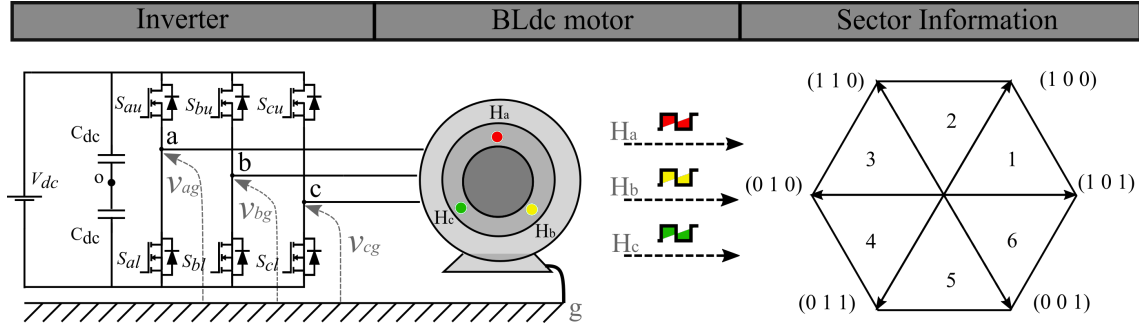


Figure 3.1: Three-phase SiC-fed BLDC motor drive system with sector information.

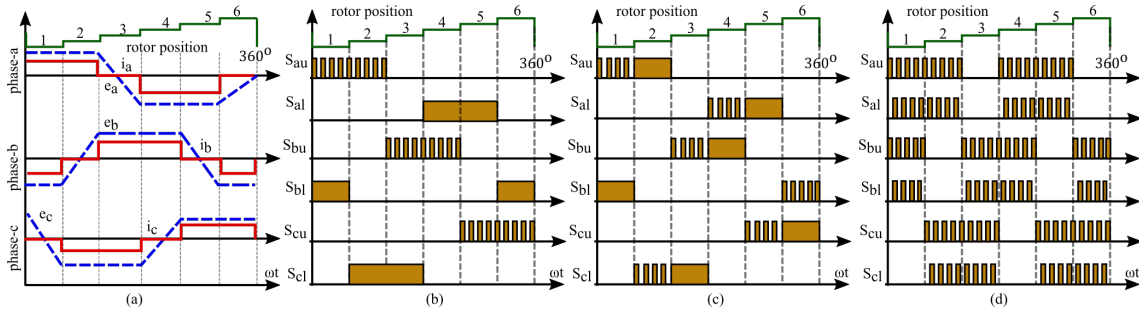


Figure 3.2: (a) Phase current, back-emf and sector information of phases a , b and c with SSC scheme, (b) gating signals of H-PWM-L-ON scheme, (c) gating signals of PWM-ON scheme, and (d) gating signals of bipolar PWM scheme.

This results in trapezoidal back electromotive force (emf) and a quasi-square phase current as shown in Figure 3.2(a).

In contrast to SSC, various PWM strategies to operate BLDC motor drives with fixed DC-link voltage are discussed in [2], and can be broadly classified as unipolar and bipolar schemes. These schemes are realized by controlling the switches in conducting phases either in PWM-mode or continuously turned on for a stipulated time period, called, on-mode or a combination of PWM and on-modes, as illustrated in Figures 3.2(b)-(d). For instance, the HS switches are controlled through PWM while the LS switches are operated in on-mode, referred to as the H-PWM-L-ON scheme, as shown in Figure 3.2(b). Similarly, both HS and LS switches are operated in PWM-mode for the first 60° conduction period while in on-mode for the remaining period, referred to as PWM-ON scheme, as illustrated in Figure 3.2(c). H-PWM-L-ON and PWM-ON are two popular PWM strategies under unipolar schemes.

In bipolar schemes, the HS and LS switches of the conducting phases are operated in PWM mode for the 120° conduction period, as illustrated in Figure 3.2(d). The classifications of bipolar PWM schemes can be understood by analyzing the gating signals in one switching cycle (T_s) as shown in Figure 3.3. The bipolar PWM shown in Figure 3.3(a) is referred to as conventional bipolar PWM (C-BPWM). While the bipolar PWM scheme shown in Figure 3.3(b) is termed as a modified bipolar

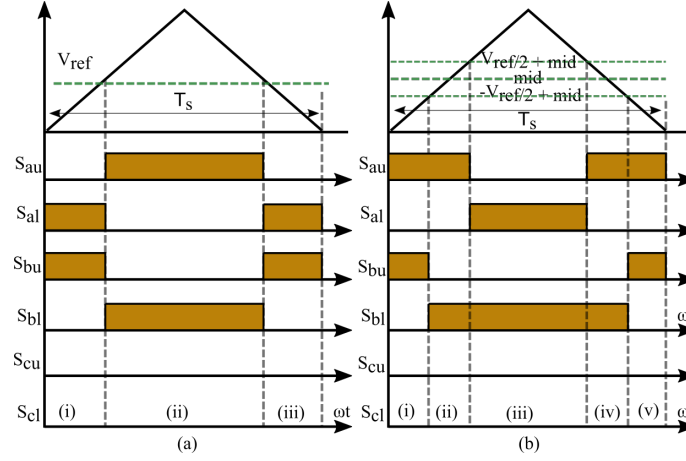


Figure 3.3: Gating signals in a switching cycle with (a) C-BPWM scheme and (b) M-BPWM scheme.

PWM (M-BPWM). The M-BPWM improves the current ripple and provides four quadrants of operation for the BLDC drive.

PWM schemes have a significant influence on the CM voltage, however, the relationship is often overlooked while selecting an appropriate modulation scheme for an application. A lack of in-depth understanding of the generated CM voltage with different PWM schemes may lead to the design and selection of oversized CM filters. Therefore, it is necessary to analyze and derive suitable analytical CM voltage expressions for various PWM schemes. Such a mathematical formulation can help to analyze the adverse effects of the CM voltage on the leakage currents that could help to optimally design the CM choke.

3.3 CM Voltages Estimation with Various PWM Schemes

The generalized CM voltage (v_{cm}) expression for a three-phase BLDC motor drive in terms of its phase-to-ground voltages is given by [51],

$$v_{cm} = \frac{v_{ag} + v_{bg} + v_{cg}}{3} \quad (3.1)$$

where, v_{ag} , v_{bg} and v_{cg} are the phase-to-ground voltages of phases a , b and c , respectively. In various PWM schemes, the inverter switches are operated either in PWM mode or on mode based on the modulation scheme employed. Thus, the

possible phase-to-ground voltages can be written as,

$$v_{kg} = \begin{cases} +\frac{V_{dc}}{2}, & S_{iu} \text{ on, } S_{il} \text{ off} \\ -\frac{V_{dc}}{2}, & S_{iu} \text{ off, } S_{il} \text{ on} \\ (2s_{iu} - 1)\frac{V_{dc}}{2}, & \text{PWM for HS switch, } S_{iu} \\ -(2s_{il} - 1)\frac{V_{dc}}{2}, & \text{PWM for LS switch, } S_{il} \\ e_j + \frac{1}{2} \sum_{i=cond. ph.} \vec{v}_{ig}, & \text{floating phase } j \end{cases} \quad (3.2)$$

where, suffix k represents all the phases, while i and j denote the conducting and floating phases, respectively ($k, i, j \in [a, b, c]$); V_{dc} is the DC-link voltage; s_{iu} and s_{il} are the gate signals of switches S_{iu} and S_{il} , respectively; and e_j is the back-emf of the floating phase j .

3.3.1 CM Voltage with Unipolar PWM Schemes

Further, a generalized expression for v_{cm} is derived for H-PWM-L-ON and PWM-ON schemes.

H-PWM-L-ON Scheme

In Sector 1 with H-PWM-L-ON scheme, the HS switch of phases a is operated in PWM-mode, the LS switch of phase b is operated in on-mode, and phase c is the floating phase, as shown in Figure 3.2(b). Hence, the phase-to-ground voltages of phases a , b and c in Sector 1 are given by,

$$v_{ag} = (2s_{au} - 1)\frac{V_{dc}}{2}, \quad (3.3)$$

$$v_{bg} = -\frac{V_{dc}}{2}, \text{ and} \quad (3.4)$$

$$v_{cg} = e_c + \frac{1}{2}[v_{ag} + v_{bg}] \quad (3.5)$$

Thus, the CM voltage with H-PWM-L-ON scheme in Sector 1 ($v_{cm_hpwmlon_1}$) can be written as,

$$\begin{aligned} v_{cm_hpwmlon_1} &= \frac{1}{3}((2s_{au} - 1)\frac{V_{dc}}{2} + v_{cg} - \frac{V_{dc}}{2}) \\ &= \frac{1}{3}e_c + \frac{1}{2}V_{dc}[s_{au} - 1] \end{aligned} \quad (3.6)$$

Similarly, the phase-to-ground voltages and v_{cm} can be derived for other sectors. It can be understood from the derived expressions that, the v_{cm} constitute a back-emf component corresponding to the floating phase and the pulse voltage

that corresponds to the PWM mode in one of the conducting phases. Thus, the generalized expression of v_{cm} in terms of back-emf and the pulse voltage for the H-PWM-L-ON scheme is given by,

$$v_{cm_hpmwlon} = \frac{1}{3}e_j + \frac{1}{2}V_{dc}[s_{iu} - 1] \quad (3.7)$$

where suffixes i and j denote the conducting phases and the floating phase, respectively.

PWM-ON Scheme

In Sector 1 with the PWM-ON scheme, the HS switch of phase a is operated in PWM-mode, the LS switch of phase b is operated in on-mode, and phase c is floating. Hence, the phase-to-ground voltages of phases a , b and c in Sector 1 are given by,

$$v_{ag} = (2s_{au} - 1)\frac{V_{dc}}{2}, \quad (3.8)$$

$$v_{bg} = -\frac{V_{dc}}{2}, \text{ and} \quad (3.9)$$

$$v_{cg} = e_c + \frac{1}{2}[v_{ag} + v_{bg}] \quad (3.10)$$

Therefore, the CM voltage in Sector 1 with PWM-ON ($v_{cm_pwmon.1}$) can be written as,

$$\begin{aligned} v_{cm_pwmon.1} &= \frac{1}{3}((2s_{au} - 1)\frac{V_{dc}}{2} - \frac{V_{dc}}{2} + v_{cg}) \\ &= \frac{1}{3}e_c + \frac{1}{2}V_{dc}[s_{au} - 1] \end{aligned} \quad (3.11)$$

Similarly, in Sector 2, the HS switch of phase a is operated in on-mode, phase b is floating, and phase c is operated in PWM mode. Thus, the phase-to-ground voltages and CM voltage in Sector 2 ($v_{cm_pwmon.2}$) are given by,

$$v_{ag} = \frac{V_{dc}}{2}, \quad (3.12)$$

$$v_{bg} = e_b + \frac{1}{2}[v_{ag} + v_{cg}], \quad (3.13)$$

$$v_{cg} = -(2s_{bl} - 1)\frac{V_{dc}}{2}, \text{ and} \quad (3.14)$$

$$\begin{aligned} v_{cm_pwmon.2} &= \frac{1}{3}(\frac{V_{dc}}{2} + v_{bg} - (2s_{bl} - 1)\frac{V_{dc}}{2}) \\ &= \frac{1}{3}e_b - \frac{1}{2}V_{dc}[s_{bl} - 1] \end{aligned} \quad (3.15)$$

Table 3.1: Phase-to-Ground Voltages in Sector 1 with C-BPWM Scheme

Voltage Mode	(i)	(ii)	(iii)
v_{ag}	$-\frac{V_{dc}}{2}$	$\frac{V_{dc}}{2}$	$-\frac{V_{dc}}{2}$
v_{bg}	$\frac{V_{dc}}{2}$	$-\frac{V_{dc}}{2}$	$\frac{V_{dc}}{2}$
v_{cg}	e_c	e_c	e_c
v_{cm}	$\frac{e_c}{3}$	$\frac{e_c}{3}$	$\frac{e_c}{3}$

From (3.11) and (3.15), the generalised expression of v_{cm} for PWM-ON case is given by,

$$v_{cm_pwm\ on} = \begin{cases} \frac{1}{3}e_j + \frac{1}{2}V_{dc}(s_{iu} - 1) & \text{for Sectors 1,3,5} \\ \frac{1}{3}e_j - \frac{1}{2}V_{dc}(s_{il} - 1), & \text{for Sectors 2,4,6} \end{cases} \quad (3.16)$$

Similar to the H-PWM-L-ON case, the generalized expression for $v_{cm_pwm\ on}$ has both back-emf and pulse voltage components.

3.3.2 CM Voltage with Bipolar PWM Schemes

A generalized expression for v_{cm} is deduced for C-BPWM and M-BPWM cases.

C-BPWM Scheme

With the C-BPWM scheme, there exist three modes in one switching cycle for each sector, as indicated in Figure 3.3(a). In Mode (i) of Sector 1, the LS switch of phase a and the HS switch of phase b conduct, as shown in Figure 3.3(a), while phase c is floating. Therefore, the v_{ag} , v_{bg} , and v_{cg} in Mode (i) of Sector 1 are given in Table 3.1. In the same way, v_{ag} , v_{bg} and v_{cg} in Modes (ii) and (iii) of Sector 1 are obtained as given in Table 3.1. Thus, the generalized expression of CM voltage with C-BPWM scheme (v_{cm_cbpwm}) in all the sectors is given by,

$$v_{cm_cbpwm} = \frac{1}{3}e_j \quad (3.17)$$

where j represents the floating phase.

M-BPWM Scheme

Similar to C-BPWM, M-BPWM constitutes five modes in one switching cycle for each sector, as indicated in Figure 3.3(b). In Mode (i) of Sector 1, HS of phases a and b conduct; in Mode (ii) HS of phase a and LS of phase b conduct; in Mode (iii)

Table 3.2: Phase-to-Ground Voltages in Sector 1 with M-BPWM Scheme

VoltageMode	(i)	(ii)	(iii)	(iv)	(v)
v_{ag}	$\frac{V_{dc}}{2}$	$\frac{V_{dc}}{2}$	$-\frac{V_{dc}}{2}$	$\frac{V_{dc}}{2}$	$\frac{V_{dc}}{2}$
v_{bg}	$\frac{V_{dc}}{2}$	$-\frac{V_{dc}}{2}$	$-\frac{V_{dc}}{2}$	$-\frac{V_{dc}}{2}$	$\frac{V_{dc}}{2}$
v_{cg}	$e_c + \frac{V_{dc}}{2}$	e_c	$e_c - \frac{V_{dc}}{2}$	e_c	$e_c + \frac{V_{dc}}{2}$
v_{cm}	$\frac{e_c}{3} + \frac{V_{dc}}{2}$	$\frac{e_c}{3}$	$\frac{e_c}{3} - \frac{V_{dc}}{2}$	$\frac{e_c}{3}$	$\frac{e_c}{3} + \frac{V_{dc}}{2}$

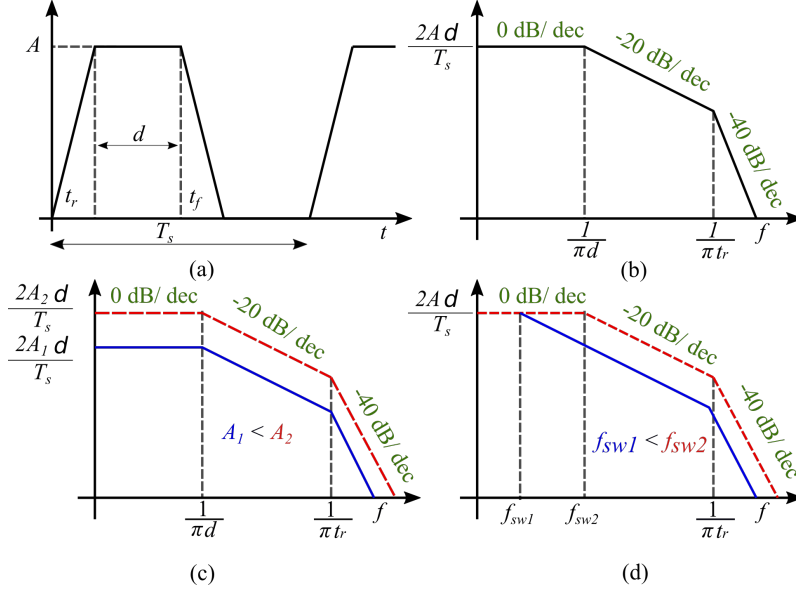


Figure 3.4: (a) Trapezoidal waveform indicating the rise time (t_r) and fall time (t_f), (b) envelope of the trapezoidal waveform in the frequency domain, (c) effect of amplitude (A) on the envelope, and (d) effect of switching frequency (f_{sw}) on the envelope.

HS of phases a and b conduct; while, in Modes (iv) and (v) switching operations are similar to that of Mode (ii) and Mode (i), respectively. In all five modes, phase c is the floating phase. The voltages v_{ag} , v_{bg} , and v_{cg} in all the five modes of Sector 1 are given in Table 3.2.

Thus, the generalized CM voltage expression for the M-BPWM scheme (v_{cm_mbpwm}) in all the sectors is given by,

$$v_{cm_mbpwm} = \begin{cases} \frac{e_j}{3} + \frac{V_{dc}}{2} & S_{iu} \text{ on} \\ \frac{e_j}{3} - \frac{V_{dc}}{2} & S_{il} \text{ on} \\ \frac{e_j}{3} & S_{iu} \text{ and } S_{il} \text{ on} \end{cases} \quad (3.18)$$

In the case of C-BPWM, the pole voltages cancel out due to their complementary nature. Whereas in the case of M-BPWM, the v_{cm} has a higher amplitude of pulse voltage that dominates the v_{cm} . Thus, CM noise is significantly higher in the case

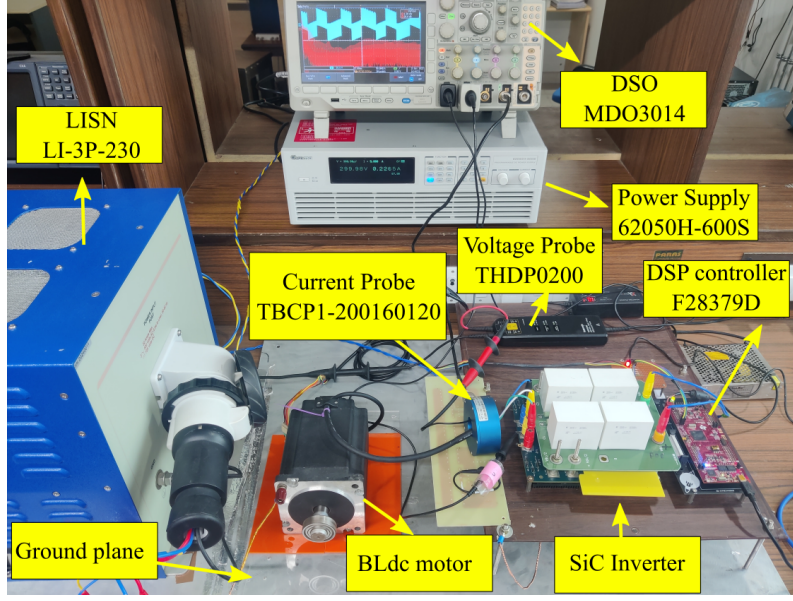


Figure 3.5: Experimental setup of a three-phase SiC-fed BLDC drive.

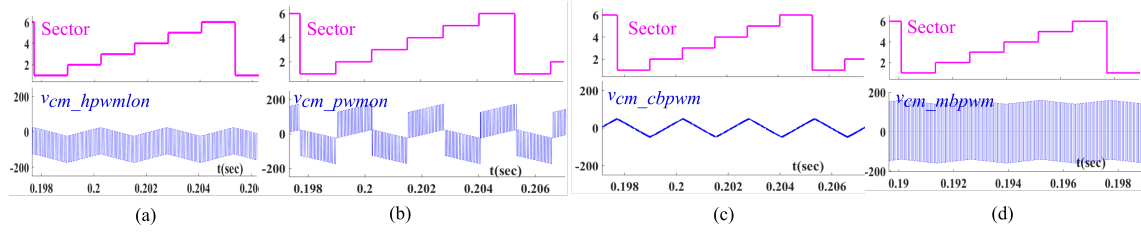


Figure 3.6: Estimated time domain profile for v_{cm} , (a) $v_{cm_hpwmlon}$, (b) v_{cm_pwmon} , (c) v_{cm_cbpwm} , and (d) v_{cm_mbpwm} .

of M-BPWM compared to C-BPWM. However, the current/torque ripple is lower in the case of M-BPWM compared to C-BPWM [52]. Further, the envelope of v_{cm} and the different parameters affecting the envelope are explained.

3.3.3 Envelope of CM Voltage

The envelope of CM voltage in all the above-discussed PWM schemes depends on parameters such as amplitude and frequency of the CM voltage. These envelopes of CM voltage provide a figure of merit for CM voltage performance. As understood from Chapters 3.3.1 and 3.3.2, the nature of the v_{cm} is dominated by the pulse voltage with a constant pulse width over a fundamental cycle for H-PWM-L-ON, PWM-ON, and M-BPWM. A trapezoidal waveform accounting for the rise time (t_r) and fall time (t_f) of v_{cm} , as shown in Figure 3.4(a), is considered and the Fourier series is utilized to estimate the boundary of v_{cm} , as shown in Figure 3.4(a). To simplify the analysis, the rise and fall times of the waveform are assumed to be

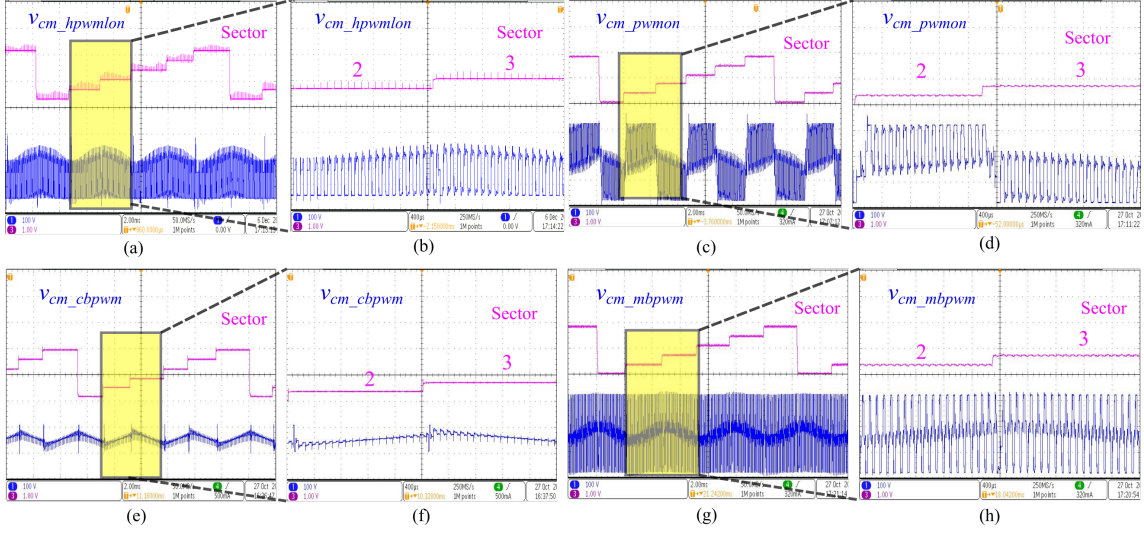


Figure 3.7: Experimental time domain profiles of, (a) $v_{cm_hpwmlon}$, (b) zoomed $v_{cm_hpwmlon}$ in Sectors 2 and 3, (c) v_{cm_pwmon} , (d) zoomed v_{cm_pwmon} in Sectors 2 and 3, (e) v_{cm_cbpwm} , (f) zoomed v_{cm_cbpwm} in Sectors 2 and 3, (g) v_{cm_mbpwm} , and (h) zoomed v_{cm_mbpwm} in Sectors 2 and 3, for $V_{dc} = 310$, $d = 0.5$ and $f_{sw1} = 10$ kHz.

equal. Thus, the pulse voltage envelope ($v_{cm_envelop}$) is expressed as [53]

$$v_{cm_envelop} = 20 \log_{10} \left(\frac{2Ad}{T_s} \right) + 20 \log_{10} \text{sinc}(\pi df) + 20 \log_{10} \text{sinc}(\pi t_r f) \quad (3.19)$$

where, d is the duty ratio and A is the amplitude of the waveform, as indicated in Figure 3.4(a). The spectrum boundary is shown in Figure 3.4(b). From (3.19), it is clear that with the increase in the amplitude of CM voltage the envelope is shifted upwards, as shown in Figure 3.4(c). Similarly, an increase in f_{sw} increases the CM voltage at higher frequencies, as shown in Figure 3.4(d). Thus, it is expected that with the increase in f_{sw} and A , the CM voltage envelope will shift upward in all the frequency ranges, thereby indicating an increase in the CM noise.

The following inferences can be made from Chapter 3.3.

1. The absolute peak-to-peak amplitude of v_{cm} in all sectors is $V_{dc}/2$ in the unipolar PWM schemes, as evident from (3.7) and (3.16).
2. The absolute peak-to-peak amplitude of v_{cm} for M-BPWM scheme is V_{dc} , as evident from (3.18). However, for C-BPWM the peak voltage reduces significantly due to the complimentary pole voltages as evident from (3.17).
3. The pulse waveform of $v_{cm_hpwmlon}$, v_{cm_pwmon} , and v_{cm_mbpwm} can be modeled as a trapezoidal waveform to estimate their envelope in frequency-domain.

Table 3.3: BLDC Motor Specifications

Parameter	Value
Rated DC-link voltage of inverter, V_{dc}	310 V
Rated power of the motor and inverter, P	1.5 kW
Rated current of motor, I	6.3 A
Nominal load torque, T	4.3 Nm
Rated speed of motor, N	3500 rpm
Number of poles	8
Torque constant, k_T	0.79 Nm/A
Back-emf constant, k_E	55 V/krpm

3.4 Experimental Validation of v_{cm} Expressions

The experimental setup of a SiC-fed three-phase BLDC motor drive with motor specifications mentioned in Table 3.3 is illustrated in Figure 3.5. A high-performance radio frequency (RF) current probe TBCP1-200160120, and a differential voltage probe THDP0200, are used to measure the leakage current and v_{cm} , respectively. A digital controller TMS320F28379D from Texas Instruments is used for implementing the PWM schemes.

Further, the analytical expressions of v_{cm} derived in Chapter 3.3 are validated through experimental time domain profiles of v_{cm} . Additionally, the frequency domain analysis of v_{cm} for unipolar and bipolar PWM schemes is presented.

3.4.1 Time Domain Results

The time domain v_{cm} profiles are estimated from the v_{cm} expressions presented for H-PWM-L-ON, PWM-ON, C-BPWM and M-BPWM schemes in (3.7), (3.16), (3.17), and (3.18), respectively. The estimated CM voltage profiles are shown in Figures 3.6(a)-(d) for H-PWM-L-ON, PWM-ON, C-BPWM, and M-BPWM, respectively. Further, the estimated CM voltage is compared with the experimentally obtained CM voltage presented in Figure 3.7.

It is observed from Figure 3.7(a) that, in all the sectors, the $v_{cm_hwpwmlon}$ has a large amplitude of pulse voltage superimposed onto the back-emf voltage. This high pulse voltage corresponds to the $\frac{V_{dc}(s_{iu}-1)}{2}$ component in (3.7) that accounts for the switching operation in the HS switch. Thus, the time domain profile of $v_{cm_hwpwmlon}$ shown in Figure 3.7 (a) is in line with the derived analytical expression given by (3.7). The estimated waveform for $v_{cm_hwpwmlon}$ is shown in Figure 3.6(a). It is observed from Figures 3.6(a) and 3.7(a) that the estimated waveform of $v_{cm_hwpwmlon}$ matches closely with the experimental time-domain profile of $v_{cm_hwpwmlon}$. The enlarged view of $v_{cm_hwpwmlon}$ is shown in Figure 3.7 (b) for Sectors 2 and 3. It is clear from Figures

3.7 (a) and (b), that the $v_{cm_hpwm_lon}$ has a negative pulse voltage.

The experimental time-domain profile of $v_{cm_pwm_on}$ is shown in Figure 3.7(c), with the corresponding zoomed version of Sectors 2 and 3 shown in Figure 3.7(d). As evident from Figure 3.7(c), the negative pulse voltage is superimposed onto the back-emf voltage in Sectors 1, 3, and 5, while the positive pulse voltage is superimposed onto the back-emf voltage in sectors 2, 4 and 6. The positive and negative pulse voltages correspond to the $\frac{1}{2}V_{dc}(s_{il} - 1)$ and $-\frac{1}{2}V_{dc}(s_{il} - 1)$ components of $v_{cm_pwm_on}$ given by (3.16). Whereas, the back-emf voltage corresponds to the $\frac{e_i}{3}$ components of $v_{cm_pwm_on}$ given by (3.16). As depicted in Figure 3.7 (c), the maximum and minimum values of $v_{cm_pwm_on}$ are $V_{dc}/2$ and zero in Sectors 2, 4 and 6; while in Sectors 1, 3 and 5, the maximum and minimum values are zero and $-V_{dc}/2$, respectively. Thus, the analytical expressions derived and the estimated waveform shown in Figure 3.6 (b) for $v_{cm_pwm_on}$ in (3.16) match closely with the corresponding experimental waveform shown in Figure 3.7 (c).

As depicted in (3.17), the v_{cm_cbpwm} has the $e_j/3$ component, which corresponds to the back-emf voltage of the floating phase, which is validated from the experimental time-domain profile of v_{cm_cbpwm} shown in Figure 3.7(e). Thus, the v_{cm_cbpwm} given by (3.17) nearly matches the experimental time-domain profile of v_{cm_cbpwm} in all the sectors. In the zoomed version of v_{cm_cbpwm} shown in Figure 3.7(f), the pulse voltage superimposed on the back-emf voltage is due to the unequal t_r and t_f , commutation and mutual inductance in three-phase BLDC motor drive [51]. As these effects are not considered, the estimated voltage, shown in Figure 3.6(c), only reflects the back-emf.

The experimentally obtained time-domain profile of v_{cm_mbpwm} is shown in Figure 3.7(g). It is observed from Figure 3.7(g) that, the voltage v_{cm_mbpwm} is identical in all sectors. Moreover, as evident from Figure 3.7(h), the maximum and minimum values of v_{cm_mbpwm} are $V_{dc}/2$ and $-V_{dc}/2$, respectively. Assuming $e_i/3$ to be insignificant when compared to V_{dc} , the maximum and minimum values of v_{cm_mbpwm} match with the expression derived in (3.18). Thus, the v_{cm_mbpwm} expression derived in (3.18) along with the estimated voltage shown in Figure 3.6(d) is in line with the experimental time domain profile.

The following inferences can be made from the time domain results of v_{cm} with various PWM schemes.

1. The analytical expressions derived in (3.7), (3.16), (3.17), and (3.18), accurately depict the time domain profiles of $v_{cm_hpwm_lon}$, $v_{cm_pwm_on}$, v_{cm_cbpwm} and v_{cm_mbpwm} in all the sectors.
2. It is evident from Figure 3.7 that, the dv/dt transitions are lower in v_{cm_cbpwm} than in $v_{cm_hpwm_lon}$, $v_{cm_pwm_on}$ and v_{cm_mbpwm} . Hence, it can be concluded that

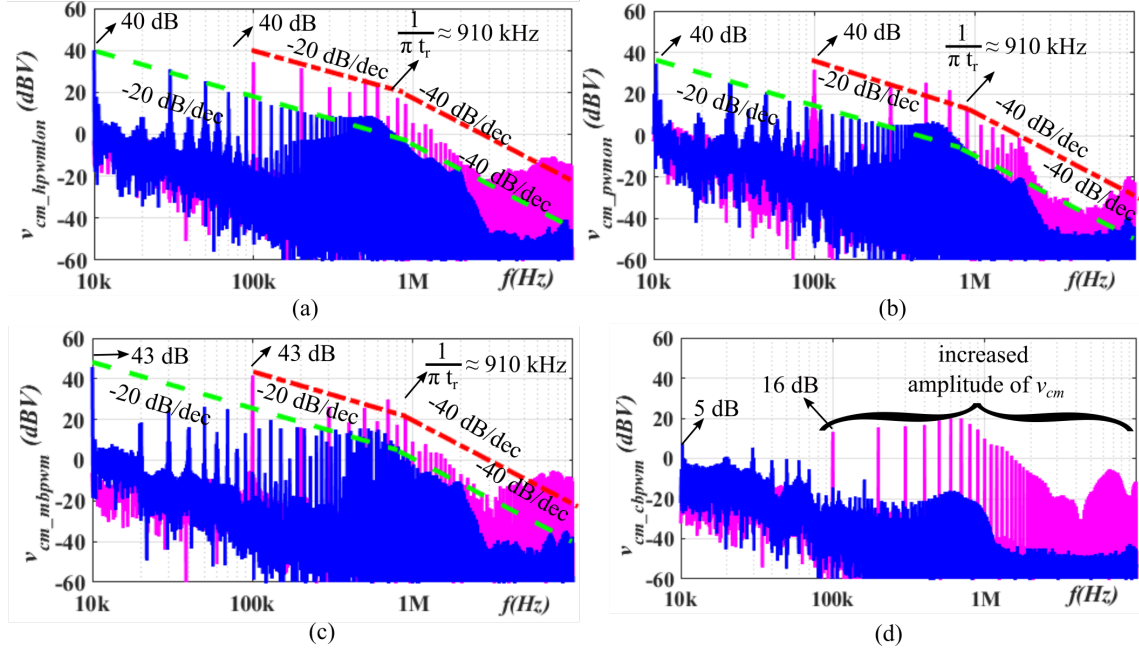


Figure 3.8: Experimental and estimated frequency spectra of v_{cm} at $f_{sw1}=10$ kHz shown in blue and green, respectively and $f_{sw2}=100$ kHz shown in pink and red, respectively, (a) $v_{cm_hpwmlon}$, (b) v_{cm_pwmon} , (c) v_{cm_mbpwm} , and (d) v_{cm_cbpwm} .

not all the bipolar schemes result in the reduction of CM noise in the BLDC drive.

3.4.2 Frequency Domain Results

To analyze the CM noise performance of the BLDC drive incorporating unipolar and bipolar schemes, the frequency spectra of the voltages $v_{cm_hpwmlon}$, v_{cm_pwmon} , v_{cm_mbpwm} and v_{cm_cbpwm} are shown in Figures 3.8(a), (b), (c), and (d), respectively, at $f_{sw1} = 10$ kHz. As the absolute peak-to-peak amplitude in $v_{cm_hpwmlon}$ and v_{cm_pwmon} are the same, the frequency spectra of $v_{cm_hpwmlon}$ and v_{cm_pwmon} are identical with an insignificant difference of around 4 dB. Moreover, as the absolute peak-to-peak amplitude of v_{cm_cbpwm} is lower and v_{cm_mbpwm} is higher than $v_{cm_hpwmlon}$ and v_{cm_pwmon} , the M-BPWM and C-BPWM schemes have the highest and least CM noise spectrum among the discussed PWM schemes, as evident from Figure 3.8.

The adoption of high switching frequency caters supremacy in terms of dynamic response, lower torque ripple, and motor efficiency, thereby elevating the system efficiency. Conversely, the high switching frequency degrades the CM performance. Further, the CM performance for various PWM schemes is verified at $f_{sw2} = 100$ kHz. The frequency spectra of $v_{cm_hpwmlon}$, v_{cm_pwmon} , v_{cm_mbpwm} and v_{cm_cbpwm} are shown in Figures 3.8(a), (b), (c), and (d), respectively, at $f_{sw2} = 100$ kHz. It is to be noted that, as the switching functions (s_{iu} , s_{il}) are independent of f_{sw} , thus, the analysis in Chapter 3.3 is valid.

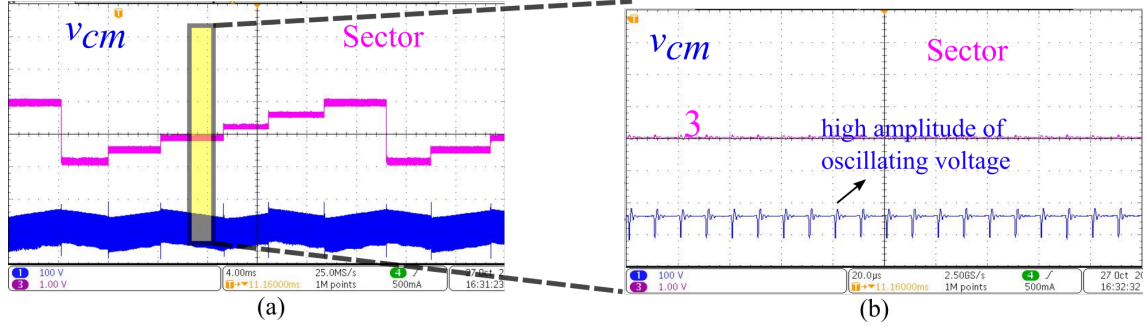


Figure 3.9: CM voltage for C-BPWM, (a) v_{cm_cbpwm} at $f_{sw}=100$ kHz and (b) enlarge view of v_{cm_cbpwm} .

As evident from Figure 3.8, the increase in f_{sw} from f_{sw1} to f_{sw2} increases the magnitude of v_{cm_hpwm} , v_{cm_pwmon} , and v_{cm_mbpwm} at higher frequency ranges; this is in line with the illustration in Figure 3.4(d). From Figures 3.8(a), (b) and (c), the estimated boundary of the envelope is quite close to the experimentally measured value. The estimated amplitude and the breakaway point are marked and shown in Figures 3.8(a), (b), and (c) for v_{cm_hpwm} , v_{cm_pwmon} , and v_{cm_mbpwm} , respectively. In the case of v_{cm_cbpwm} ideal, the CM voltage should only consist of the back-emf component. However, due to the non-idealities like unequal rise, fall, and delay times between top and bottom switches of a phase leg, and parasitic capacitance a high-frequency low amplitude voltage appears on top of the back-emf voltage as shown in Figure 3.7(e), and the enlarged view is shown in Figure 3.7(f) for $f_{sw}=10$ kHz. The v_{cm_cbpwm} for 100 kHz is shown in Figure 3.9(a) and the enlarged view is shown in Figure 3.9(b). It is clear from Figure 3.9(b) that the v_{cm_cbpwm} has a high amplitude of oscillating voltage component as compared to that of the v_{cm_cbpwm} at 10 kHz due to high di/dt and the fall of CM impedance. As a result, the spectrum of CM voltage increases with the increase in f_{sw} as shown in Figure 3.8 (d). It is clearly observed from Figures 3.7(f) and 3.9 (b), that the profile of voltage changes significantly. Thus, predicting the pattern or the structure of the signal is quite difficult in the case of C-BPWM.

The following inferences can be made from the frequency spectra of v_{cm} with various PWM schemes.

1. The increase in f_{sw} increases the CM noise in the BLDC motor drive with all the unipolar and bipolar schemes.
2. Irrespective of the f_{sw} , the C-BPWM and M-BPWM schemes show the best and worst CM noise performances, respectively. However, at higher f_{sw} , the v_{cm} for C-BPWM increases despite the complementary nature of the pole voltages due to the mismatch in t_r and t_f in the active devices of the conducting phase voltages.

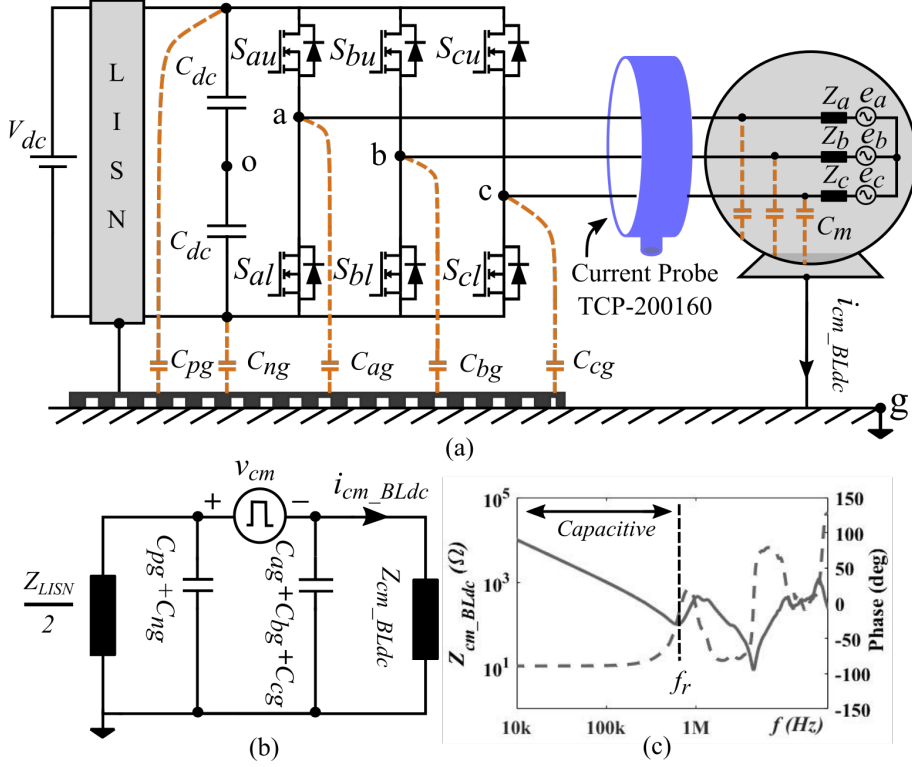


Figure 3.10: (a) Parasitic capacitance in three-phase BLDC motor drive, (b) CM equivalent circuit, and (c) Z_{cm_BLdc} impedance profile.

3.5 High-Frequency Leakage Current and CM Choke Requirement

As discussed in Chapter 3.3, v_{cm} of the BLDC motor drive system is affected by the PWM scheme, resulting in a different high-frequency leakage current (i_{cm_BLdc}) for various PWM schemes. Further, the i_{cm_BLdc} due to v_{cm} for H-PWM-L-ON, PWM-ON, C-BPWM, and M-BPWM is discussed in detail. Also, considering the stringent EMI regulations for the drive systems, understanding various factors influencing the i_{cm_BLdc} helps to understand the CM choke requirement.

3.5.1 Impact of PWMs Schemes on i_{cm_BLdc}

The dv/dt transitions in v_{cm} excite the BLDC motor phase-to-ground parasitic capacitance (C_m) and inverter parasitic capacitance ($C_{ag}, C_{bg}, C_{cg}, C_{pg}$, and C_{ng}), shown in Figure 3.10(a); this results in i_{cm_BLdc} through the ground. The corresponding CM equivalent circuit for a three-phase BLDC motor drive is shown in Figure 3.10(b). The i_{cm_BLdc} is derived from Figure 3.10(b) and is expressed as (3.20). Where $Z_{C1} = 1/(\omega C_1)$, $Z_{C2} = 1/(\omega C_2)$, $C_1 = C_{pg} + C_{ng}$, and $C_2 = C_{ag} + C_{bg} + C_{cg}$; while, the impedance Z_{cm_BLdc} is the CM impedance of the BLDC motor, that is measured using a network analyzer (NH4L-IAI2) and is shown in Figure 3.10(c). It is observed

$$i_{cm_BLdc} = \frac{(Z_{cm_BLdc} + Z_{C2})(0.5Z_{LISN} + Z_{C1})Z_{C2}v_{cm}}{\left[Z_{cm_BLdc}Z_{C2}(0.5Z_{LISN} + Z_{C1}) + 0.5Z_{LISN}Z_{C1}(Z_{cm_BLdc} + Z_{C2}) \right] (Z_{cm_BLdc} + Z_{C2})} \quad (3.20)$$

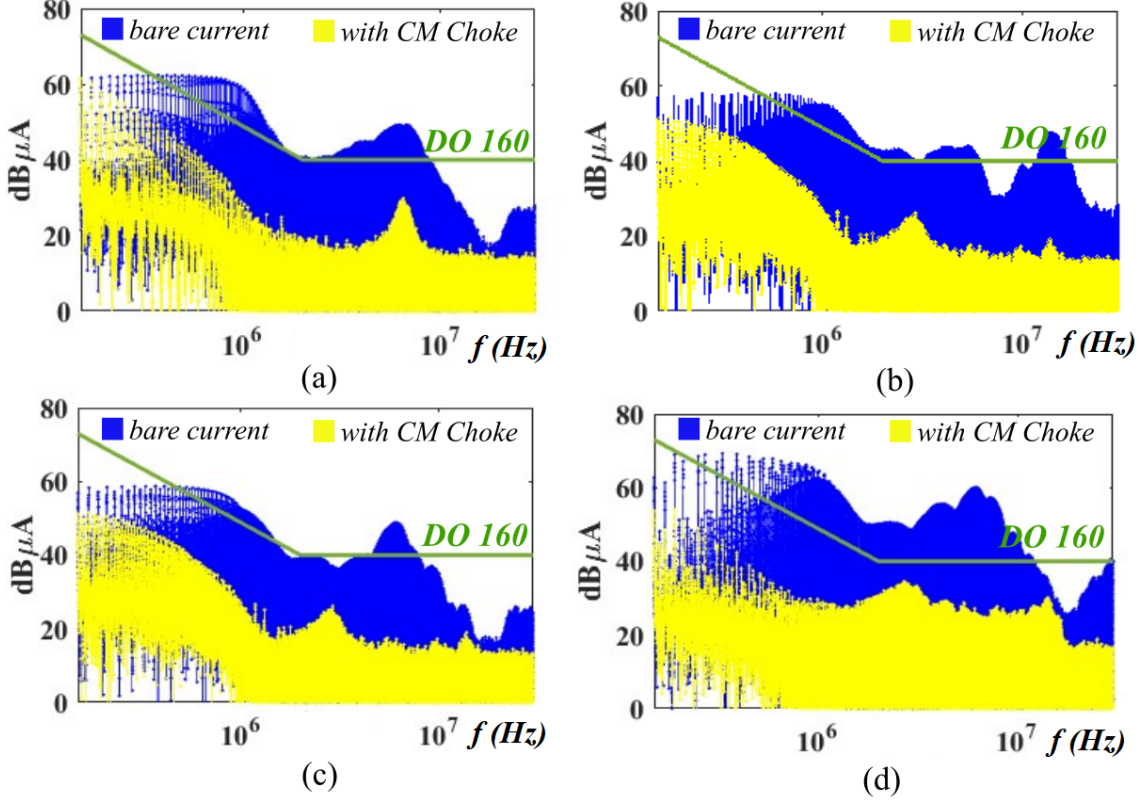


Figure 3.11: Frequency spectra of i_{cm_BLdc} for different modulation schemes at 10 kHz f_{sw} with and without CM choke, (a) H-PWM-L-ON, (b) PWM-ON, (c) C-BPWM, and (d) M-BPWM.

from Figure 3.10(c) that the impedance Z_{cm_BLdc} is capacitive in nature for $f < f_r$. The i_{cm_BLdc} given by (3.20) is dependent on v_{cm} and parasitic capacitance.

The experimentally measured i_{cm_BLdc} by clamping the wires of phases a , b and c in an RF current probe (TBCP-200160), as shown in Figure 3.10(a), is given in Figure 3.11 for $f_{sw1} = 10$ kHz. While the i_{cm_BLdc} for $f_{sw2} = 100$ kHz with H-PWM-L-ON, PWM-ON, C-BPWM and M-BPWM is shown in Figure 3.12. As illustrated in Figure 3.8, v_{cm} is high for $f_{sw2} = 100$ kHz when compared to $f_{sw1} = 10$ kHz; while the Z_{cm_BLdc} remains the same for various PWM schemes, as shown in Figure 3.10(c). Therefore, as observed from Figures 3.11 and 3.12, the magnitude of i_{cm_BLdc} is high for $f_{sw2} = 100$ kHz when compared to $f_{sw1} = 10$ kHz.

As observed from Figures 3.11(a) and (b), the i_{cm_BLdc} is almost identical for unipolar PWM schemes (i.e., H-PWM-L-ON and PWM-ON); while in bipolar PWM schemes, the i_{cm_BLdc} is less with C-BPWM due to lower magnitude of v_{cm_cbpwm} and is higher with M-BPWM scheme due to higher v_{cm_mbpwm} magnitude. Similarly, as evident from Figure 3.12, the H-PWM-L-ON, PWM-ON, and C-BPWM schemes

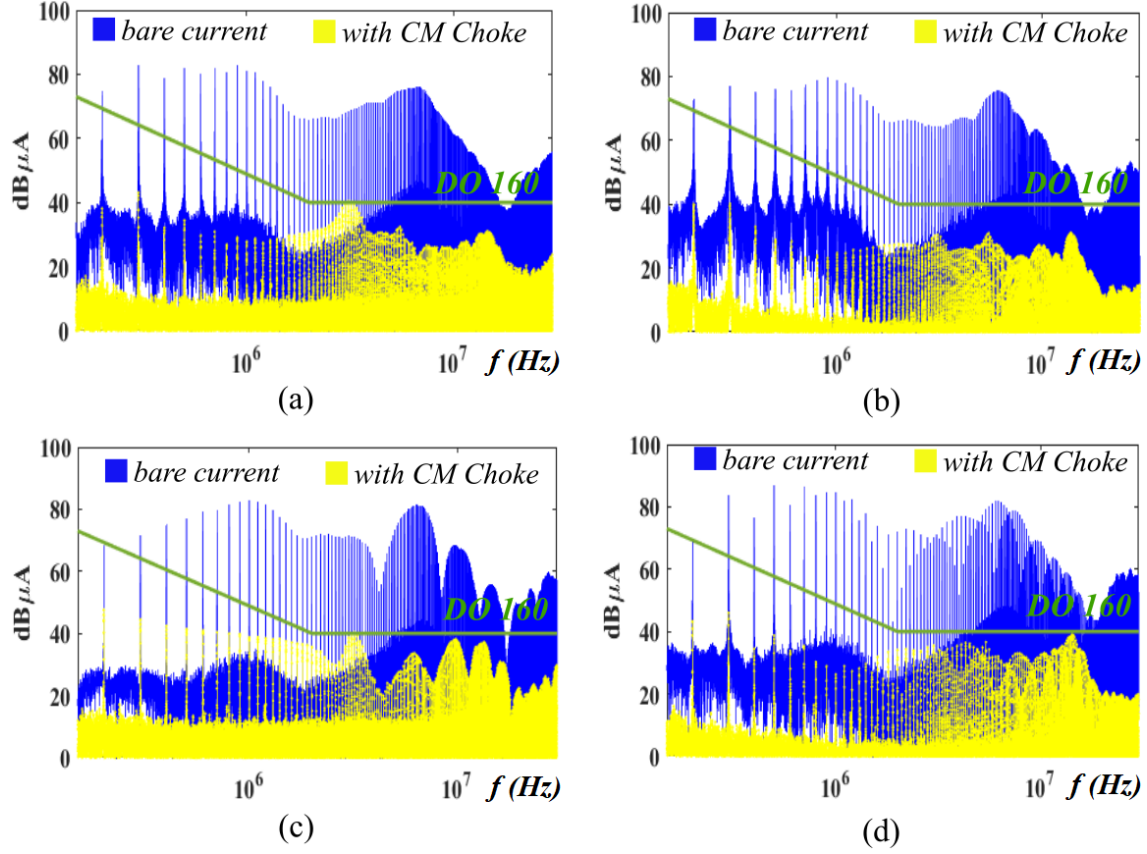


Figure 3.12: Frequency spectra of the i_{cm_BLdc} for different modulation schemes at 100 kHz f_{sw} with and without CM choke, (a) H-PWM-L-ON, (b) PWM-ON, (c) C-BPWM, and (d) M-BPWM.

give reduced i_{cm_BLdc} when compared to the M-BPWM scheme at $f_{sw2} = 100$ kHz. The Figures 3.13(a) and (b) show the frequency spectra of i_{cm_BLdc} at integral multiples of f_{sw} for $f_{sw1} = 10$ kHz and $f_{sw2} = 100$ kHz, respectively. It can be concluded from Figure 3.13 that the f_{sw} component in the i_{cm_BLdc} is higher with the M-BPWM scheme and lower with the C-BPWM scheme at both $f_{sw1} = 10$ kHz and $f_{sw2} = 100$ kHz. Thus, from the above discussion, the following inferences are obtained.

1. The C-BPWM gives a better CM noise performance at lower f_{sw} ; however, with the increase in the f_{sw} , the BLDC motor drive operating with the H-PWM-L-ON, PWM-ON, and C-BPWM schemes show similar CM noise performance.
2. Although the M-BPWM scheme is known to reduce the current ripple of the BLDC drive, it results in higher CM noise compared to the H-PWM-L-ON, PWM-ON, and C-BPWM schemes, for all the frequency ranges.

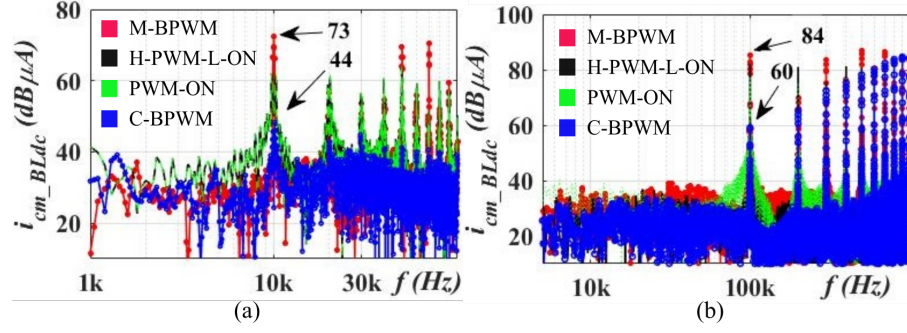


Figure 3.13: Frequency spectra indicating the f_{sw} component and its multiples of the i_{cm_BLdc} with H-PWM-L-ON, PWM-ON, C-BPWM and M-BPWM schemes at (a) $f_{sw1} = 10$ kHz and (b) $f_{sw2} = 100$ kHz.

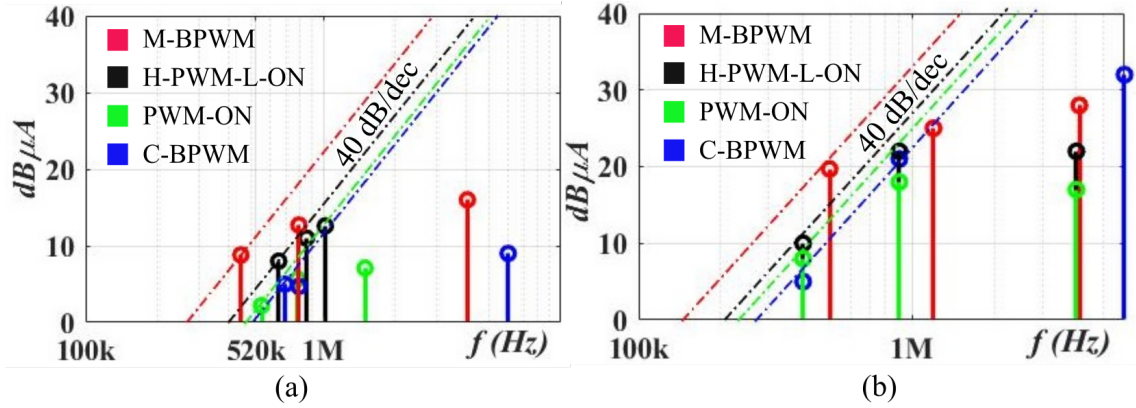


Figure 3.14: Required attenuation and f_c at (a) $f_{sw1} = 10$ kHz and (b) $f_{sw2} = 100$ kHz.

3.5.2 Selecting correct CM choke and DM choke material

Selecting the material for the suppression of EMI is of utmost importance, as it dictates several critical aspects of its performance. Firstly, the chosen material determines the maximum saturation flux density, which directly impacts the choke's ability to handle high levels of current while maintaining its functionality. Additionally, the material influences the number of turns required to achieve the desired common-mode (CM) inductance, and differential-mode (DM) inductance thereby affecting the overall size and efficiency of the choke. Moreover, the material's characteristics also play a significant role in how the CM choke behaves in varying temperature conditions. Different materials exhibit unique thermal properties, which can influence the choke's stability and reliability across a range of operating temperatures. In essence, the material selection for the CM choke is a multifaceted decision that directly influences its performance, size, and resilience under changing environmental conditions. Careful consideration of these factors is essential for designing an effective and reliable CM and DM choke for applications for suppressing electromagnetic interference. Further, the guidelines for selecting the CM choke and DM choke are discussed.

Guidelines for selecting CM choke.

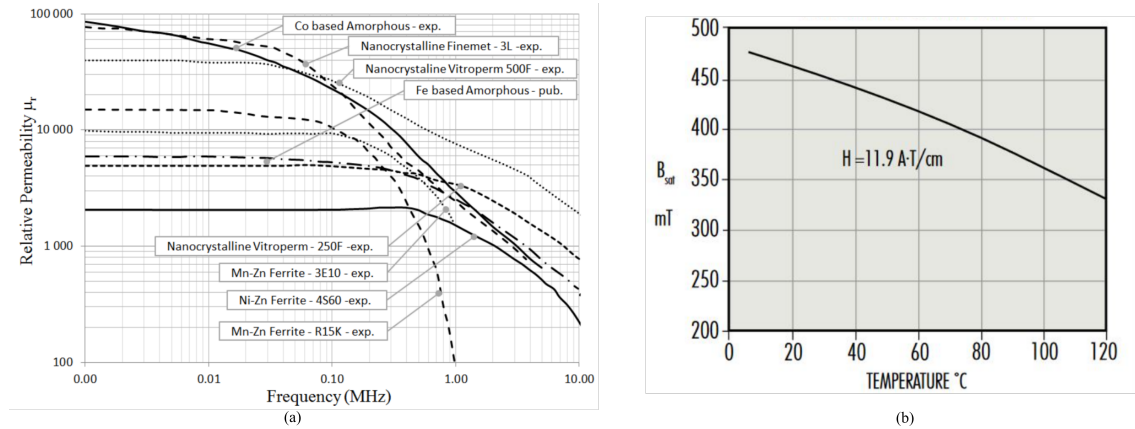


Figure 3.15: (a) Variation of permeability concerning frequency for different magnetic materials and (b) effect of saturation flux density for temperature.

Utilizing a toroidal ferrite-type material for CM choke applications is a common practice owing to its cost-effectiveness and robust performance across a wide frequency spectrum. Plots of relative permeability as a function of frequency are shown in Fig.3.15(a). These plots are a mix of published and experimental data. Ni-Zn ferrite exhibits the most consistent permeability profile across a broad frequency spectrum. Remarkably, its permeability remains nearly constant up to 500 kHz, making it a preferred choice for applications operating in the MHz range. However, it's imperative to acknowledge the inherent limitations of ferrite materials, particularly their relatively modest saturation flux density, typically around 0.4 Tesla. Notably, this saturation level is not static but varies with temperature, as demonstrated in Fig.3.15(b). In contrast, while amorphous metal and nanocrystalline materials boast the highest initial permeability, their permeability gradually decreases with increasing frequency. This characteristic may limit their suitability for high-frequency applications where stable permeability is crucial. However, increasing the number of turns slightly will compensate for its drop in permeability and will make the nano-crystalline core behave perfectly over the entire frequency range, and their saturation flux density, peaking at approximately 1.3 Tesla, remains impressively stable across a broad temperature range. This stability, coupled with superior performance metrics, positions nanocrystalline cores as a compelling choice for applications demanding high CM inductance within compact form factors.

Guidelines for selecting DM choke.

Powder cores are composed of soft-magnetic metallic powders, primarily iron, and its alloys, and additives like nickel, molybdenum, and silicon, bound together with a binder material. This structure results in low permeability and soft saturation

behavior making it a suitable choice for line inductors. The common type of power iron cores is Iron powder, Molypermalloy Powder (MPP), High Flux, Sendust (Kool M μ), XFlux core, and gaped iron core. A brief discussion of the types of powder cores is discussed below.

1. *MPP core*

MPP powder is an alloy comprising approximately 80% nickel, 17% iron, and 3% molybdenum. Its high nickel content influences both electrical and magnetic properties, contributing to its comparatively high price among powder core materials. MPP cores boast a maximum available permeability of $\mu=550$, notably higher than other powder cores. They exhibit the lowest losses among powder cores and demonstrate excellent inductance stability under DC bias and elevated temperatures.

2. *High Flux powder core*

High Flux powder composed of approximately 50% iron and 50% nickel, yields cores with an overall permeability ranging from 14 to 160. Notably, it enables a remarkably high flux level, double that of MPP, before reaching saturation. These characteristics render High Flux cores ideal for high DC-bias chokes, often allowing designers to reduce core size compared to MPP or Sendust alternatives. While High Flux material exhibits higher losses than MPP and Sendust, it fares better than XFlux under similar excitation conditions.

3. *Sendust powder core*

Sendust powder, composed primarily of iron, silicon, and aluminum, offers a cost-effective solution with a permeability range of 14 to 125, making it ideal for high-frequency SMPS storage chokes, especially with recent improvements allowing for higher currents and reduced power losses above 500 kHz.

4. *XFlux cores*

The iron-silicon alloy, containing about 6.5% silicon, ensures stable inductance over DC bias in high-flux cores. These cores, lacking nickel, serve as a cost-effective alternative when losses are not a primary concern. XFlux cores, on the other hand, exhibit relatively large loss generation. Consequently, they find application in scenarios where frequency remains below 30 kHz or when the amplitude of high-frequency current passing through the component is restricted.

5. *Iron-powder cores*

Iron-powder cores typically offer a permeability ranging from 4 to 100. They commonly utilize an organic binder, which can undergo thermal aging at

elevated temperatures. While iron-powder cores are cost-effective compared to other powder cores, they tend to incur higher core losses when compared to Sendust, High Flux, and MPP cores.

6. Gaped ferrites core

Gaped ferrites possess the ability to store energy due to their stable inductance up to specific currents. Consequently, they find utility in applications such as storage, differential mode filter chokes, or damping under DC bias. Moreover, the effective permeability of a gapped ferrite core often falls within the same range as powdered cores ($\mu=4\text{--}500$). Both core types are suitable for use at relatively high frequencies of several tens of kilohertz, owing to their high resistivity. However, at even higher frequencies, ferrites or Sendust powder cores emerge as the preferred solution. To summarize the above discussion a comparison figure of merit for DM choke selection is shown in Fig.3.16.

	MPP	High Flux	Kool M μ	Si-Fe	Iron powder
Permeability	14-550	14-160	14-160	19-125	4-100
Saturation (B sat)	0,7 T	1,5 T	1,0 T	1,6 T	1,2-1,4 T
Frequency Response - 60u flat to...	6 MHz	3 MHz	5 MHz	3 MHz	1 MHz – 1GHz
AC core loss	Lowest	Moderate	Low	High	Highest (and variable)
DC bias	Better	Best	Good	Best	Good
Alloy composition	Fe Ni Mo	Fe Ni	Fe Si Al	Fe Si	Fe

Figure 3.16: (a) Comparison for iron powder core for DM choke.

CM choke is widely adapted for passive CM mitigation technique, due to its simple design, reliability, and cost-effectiveness [54]. Further, the CM inductance (L_{cm}) requirement of the CM choke with various PWM schemes and for $f_{sw} = [10 \text{ kHz}, 100 \text{ kHz}]$ in a three-phase BLDC motor drive is discussed in detail.

From the frequency spectra of the i_{cm_BLdc} , shown in Figure 3.11, the cutoff frequencies (f_c) are estimated for H-PWM-L-ON, PWM-ON, C-BPWM and M-BPWM as 410 kHz, 480 kHz, 520 kHz, and 270 kHz, respectively, as shown in Figure 3.14(a). It is observed from the estimated f_c that the L_{cm} required to attenuate the i_{cm_BLdc} is almost the same for the H-PWM-L-ON and PWM-ON schemes. In addition, the L_{cm} required for C-BPWM is the lowest and, with the M-BPWM scheme, the L_{cm} required to attenuate the i_{cm_BLdc} is the highest among all the discussed unipolar and bipolar PWM schemes.

Similarly, the estimated f_c for $f_{sw2} = 100 \text{ kHz}$ for H-PWM-L-ON, PWM-ON, C-BPWM, and M-BPWM schemes are 225 kHz, 240 kHz, 258 kHz, and 150

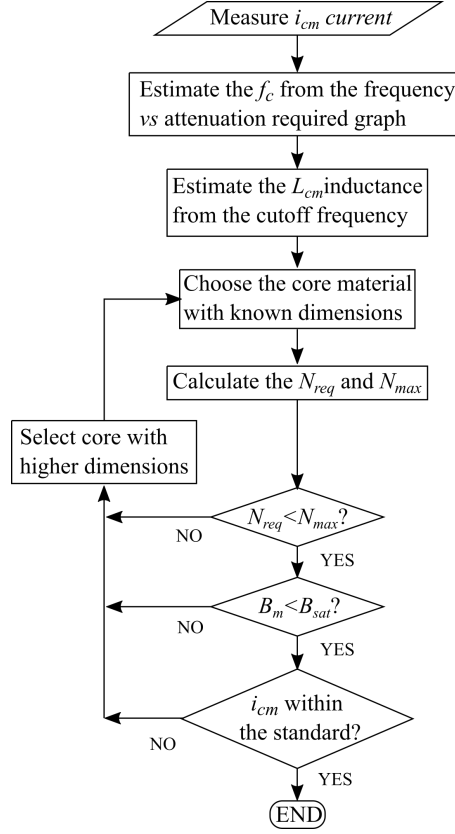


Figure 3.17: Flowchart employed for CM choke design.

kHz, respectively, as evident from Figure 3.14(b). Hence, the L_{cm} required to attenuate i_{cm_BLdc} with the M-BPWM scheme is higher than that of H-PWM-L-ON, PWM-ON, and C-BPWM schemes. Moreover, it can be concluded from Figure 3.14 that the estimated f_c with $f_{sw1} = 10\text{kHz}$ is higher when compared to that of $f_{sw2} = 100\text{ kHz}$ in all the discussed unipolar and bipolar PWM schemes. Therefore, the L_{cm} requirement to mitigate the i_{cm_BLdc} increases for $f_{sw2} = 100\text{ kHz}$ when compared to the $f_{sw1} = 10\text{ kHz}$.

The CM chokes are used to attenuate i_{cm_BLdc} with the H-PWM-L-ON, PWM-ON, C-BPWM, and M-BPWM schemes for $f_{sw1} = 10\text{ kHz}$ and $f_{sw2} = 100\text{ kHz}$. From the required attenuation plot shown in Figure 3.14, the f_c is estimated. From the estimated f_c , the required inductance to meet the standard is calculated using

$$L_{cm} = \frac{1}{4\pi^2 f_c^2 (3C_m)}. \quad (3.21)$$

The required number of turns (N_{req}) for a selected core with inductance per turn, A_L , is calculated from

$$N_{req} = \sqrt{\frac{L_{cm}(f_c)\mu(10kHz)}{A_L\mu(f_c)}} \quad (3.22)$$

Where μ is the permeability of the core. The maximum turns that can be

accommodated in the selected core are obtained from

$$N_{max} = \frac{W_f \pi (ID - d_{wire})}{d_{wire} * 360^\circ}. \quad (3.23)$$

where W_f is the winding factor, d_{wire} is the diameter of the wire which depends upon the motor current rating, and ID is the inner diameters of the CM choke, respectively.

The required number of turns (N_{req}) should be less than the maximum number of turns (N_{max}). Thus, the core dimension of the CM choke is chosen such that $N_{req} < N_{max}$.

The peak magnetic flux density (B_{pk}) in the core is estimated to verify the saturation of the core. The B_{pk} can be estimated by

$$B_{pk} = \frac{L_{cm} i_{cmpk} + L_{lk} i_{dmpk}}{N A_e} < B_{sat} \quad (3.24)$$

where B_{sat} is the saturation flux density of the core, which is provided by the manufacturer, the i_{dmpk} current is the peak DM current (motor-rated current), i_{cmpk} is the CM peak current, N is the number of turns and A_e is the cross-sectional area of the CM choke. Inductance L_{lk} is the leakage inductance of the CM choke and is estimated for each phase from [46]

$$L_{lk} = 2.5 \mu_o N^2 \frac{A_e}{l_{eff}} \left(\frac{l_e}{2} \sqrt{\frac{\pi}{A_e}} \right)^{1.45} \quad (3.25)$$

where θ is the maximum angle that the winding subtends on the core, l_{eff} is the effective mean length of the leakage path and is given by

$$l_{eff} = l_e \sqrt{\frac{\theta}{2\pi} + \frac{1}{\pi} \sin\left(\frac{\theta}{2}\right)} \quad (3.26)$$

where l_e is the effective length of the magnetic path of the core and it is expressed as

$$l_e = \frac{\pi(OD - ID)}{\ln(OD/ID)}. \quad (3.27)$$

where OD is the outer diameter. Thus, B_{pk} in the core should be less than the saturation flux density of the core (B_{sat}). A flowchart is provided for the design of the CM choke as shown in Figure 3.17. Following the flowchart, the CM choke is fabricated for various PWM schemes for 10 and 100 kHz cases, as shown in Figure 3.18.

The type A CM choke is used with C-BPWM, the type B CM choke is used with H-PWM-L-ON and PWM-ON schemes, and the type C CM choke is used with M-BPWM scheme for $f_{sw1} = 10$ kHz. It is to be noted that, for $f_{sw1} = 10$ kHz and

Table 3.4: Parameters of CM Choke

Type of CM Choke	PWM Schemes	Magnetic core Part no.	Dimensions (OD x ID x HT) (mm)	L_{cm} @ f_{sw} (mH)	Box volume (cm ³)
A	C-BPWM	T60004-L2025-W621-51	25x20x10	1.4	6.25
B	H-PWM-L-ON and PWM-ON	T60006-L2025-W451-03	28x12x12	3.8	9.41
C	M-BPWM	T60004-L2030-W676-51	30x25x17	10.5	15.30
D	H-PWM-L-ON, PWM-ON and C-BPWM	T60006-L2040-W452-03	43x28x19	6.2	35.13
E	M-BPWM	T60006-L2045-V102	48x26x19	13.4	43.78

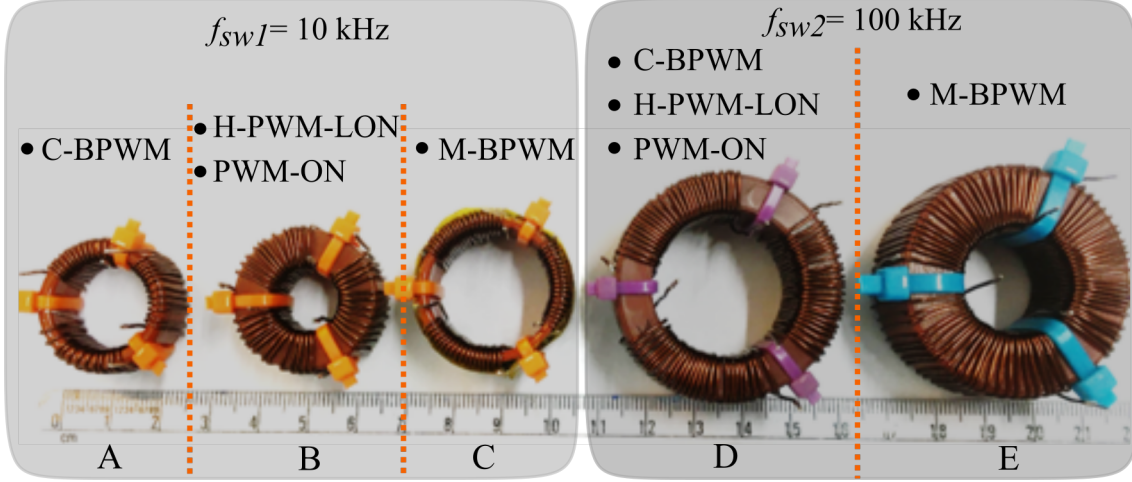


Figure 3.18: CM chokes for $f_{sw1} = 10$ kHz and $f_{sw2} = 100$ kHz with H-PWM-L-ON, PWM-ON, C-BPWM, and M-BPWM schemes.

$f_{sw2} = 100$ kHz, the CM choke type with H-PWM-L-ON and PWM-ON is the same; this is because of the same L_{cm} requirement. While the type D CM choke is used for the H-PWM-L-ON, PWM-ON, and C-BPWM schemes, and the type E choke is used to attenuate the i_{cm_BLdc} with the M-BPWM scheme for $f_{sw2} = 100$ kHz. The core models along with their dimensions for the type A, B, C, D, and E CM chokes are given in Table 3.4.

The attenuated i_{cm_BLdc} current with H-PWM-L-ON, PWM-ON, C-BPWM, M-BPWM techniques for $f_{sw} = 10$ kHz and 100 kHz is shown in Figures 3.11 and 3.12, respectively. It is observed from Figures 3.11 and 3.12 that, the CM chokes reduced i_{cm_BLdc} current below the limit line. To ensure the core saturation, the peak CM current (i_{cmpk}) is investigated from f_{sw} component for both $f_{sw} = 10$ kHz and 100 kHz. The i_{cmpk} current value is tabulated in Table 3.4. In addition, the B_{pk} given in (3.24) is calculated for all chokes with respective PWM techniques and is tabulated in Table 3.4. The B_{pk} for all chokes is less than the B_{sat} value, thus validating the CM choke performance satisfactorily.

In addition, it is evident from Table 3.4 that the box volume of types A CM choke is less compared to the types B and C; this is because the L_{cm} required with the C-BPWM scheme is lower for $f_{sw1} = 10$ kHz compared to the H-PWM-L-ON, PWM-ON, and M-BPWM schemes. In addition, as the M-BPWM has the higher i_{cm_BLdc} for both the $f_{sw1} = 10$ kHz and $f_{sw2} = 100$ kHz, the box volumes of the types C and E CM chokes are higher.

The following inferences can be made from the above discussion.

1. The CM choke requirements for the BLDC motor drive with the H-PWM-L-ON and the PWM-ON schemes are identical.
2. Among the H-PWM-L-ON, PWM-ON, C-BPWM, and M-BPWM schemes,

the C-BPWM has the lowest CM choke requirement.

3. For any of the f_{sw} employed, the BLDC motor drive with the M-BPWM scheme shows the highest CM choke requirement and unipolar PWM has the same CM choke requirement.

3.6 Effects of PWM on Motor and CM Performance

The unipolar and bipolar PWMs are extensively used in a three-phase BLDC motor drive. The key performance parameters like torque ripple, current ripple, commutation, vibration, efficiency, voltage utilization ratio, impact of dead band, and reliability are discussed for various PWM schemes in [2], [55], [5], [52], [56], and [57].

In the context of PWM control strategies, it is observed that the H-PWM-L-ON or H-ON-L-PWM exhibit an uneven loss distribution among active devices, while the PWM-ON or ON-PWM demonstrate a more balanced loss distribution [2]. It is noted that the PWM-ON and ON-PWM configurations outperform the H-PWM-L-ON or H-ON-L-PWM in terms of various key performance parameters, including efficiency, reliability, current ripple, torque ripple and the operational safety area (SOA) for sensorless operation [2], [55], [5], [52], [56], [57]. However, H-PWM-L-ON, H-ON-L-PWM, PWM-ON and ON-PWM have the same CM performance and CM choke requirement.

In the context of PWM control strategies, the C-BPWM configuration stands out for its rapid control response, enabling four-quadrant operation and facilitating regenerative braking. Nevertheless, it is imperative to note that this approach is not without trade-offs. The voltage fluctuation between the PWM ON and OFF states is doubled, consequently increasing the amplitude of current ripples, electrical losses, and heat generation [5], [52]. Conversely, the M-BPWM configuration presents a distinct characteristic where the voltage fluctuation between the PWM ON and OFF states remains consistent with that of the unipolar PWM method. However, due to the halved conduction time, there is a notable reduction in the current ripple by a factor of two [55]. Theoretically, this reduction ratio amounts to one-half and one-fourth when compared to the unipolar PWM and C-BPWM methods, respectively [2], [55].

As for the CM performance considerations, it is worth highlighting that C-BPWM outperforms both M-BPWM and the unipolar PWM techniques regarding CM performance. Additionally, the CM choke requirement is notably less in the case of C-BPWM compared to other PWM schemes.

These factors should be meticulously considered when selecting an appropriate PWM control strategy, as they substantially impact both system and CM performance.

3.7 Conclusion

SiC devices can significantly improve the efficiency, power density, and dynamic performance of the BLDC motor drive. However, the challenging issue of v_{cm} also appears in the BLDC drive system. This chapter has investigated the critical phenomenon of CM voltage and its adverse effects on a three-phase BLDC drive. The CM analysis has been performed for two distinct classes of popular PWM schemes namely, (i) unipolar PWM and (ii) bipolar PWM for 10 kHz and 100 kHz switching frequencies.

In the case of unipolar PWM, the derived voltage expressions revealed that the pulsating nature of the CM voltages is predominant in unipolar PWM schemes. As a result, the v_{cm} generated for the H-PWM-L-ON and PWM-ON is almost the same. Thus, in the case of the unipolar PWM schemes time domain profile may appear different but the spectrum of the v_{cm} generated is almost the same. As a result, the CM choke requirement for unipolar PWMs in a three-phase BLDC motor drive is almost the same.

In the case of a bipolar PWM scheme, the C-BPWM generates less v_{cm} noise due to the complementary nature of the active phase pole voltage. However, in the case of the M-BPWM scheme, it generates high v_{cm} noise. Thus, in the case of a bipolar PWM scheme the nature of v_{cm} noise changes significantly. As a result, the CM choke requirement for C-BPWM is less compared to M-BPWM.

With the increase in f_{sw} , the v_{cm} is upward shifted, indicating that the spectral envelope of v_{cm} has increased. As a result, the CM choke requirement for H-PWM-L-ON, PWM-ON, C-BPWM, and M-BPWM increase by 82.20%, 73.2%, 73.2%, and 65.05%, respectively.

The CM analysis presented in this chapter, combined with the discussions on the torque ripple and efficiency in the literature, will help the designer choose an appropriate PWM scheme for a given application.

Chapter 4

DC-side EMI Filters With Integrated Magnetics Chokes

4.1 Introduction

This chapter presents two integrated magnetic choke structures for DC-side single and two-stage passive EMI filters. The integrated choke for a single-stage EMI filter utilizes ER, I, and one toroidal core with a suitable winding arrangement. Similarly, the integrated choke for a two-stage EMI filter utilizes one ER and two toroidal cores with suitable winding arrangements. These integrated magnetic choke structures are suitable for a toroidal with a small window area.

The core structures used in the presented integrated chokes are commercially available in a wide range of dimensions; thereby providing design flexibility and avoiding extra costs of customization. The designed integrated chokes utilize the high permeability noncrystalline CM choke that has a lesser window area and offers higher CM inductance. The decoupled CM and DM flux through the ER core and toroidal core of the CM choke reduces the risk of magnetic saturation in the presented integrated chokes. In addition, these integrated chokes reduce the PCB area and box volume of the filter when compared to their respective conventional single-stage and two-stage EMI filters.

In addition, this chapter also includes the analytical expression for CM and DM inductance which are validated experimentally using an impedance analyzer. Moreover, the magnetic saturation analysis is presented for the single-stage and two-stage integrated chokes along with the simulation in ANSYS 3D Maxwell. The CM and DM noise attenuation performance and the reduction in PCB area and EMI filter box volume incorporating these integrated chokes have been validated experimentally on a three-phase BLDC motor drive.

4.2 Integrated Choke for Single-Stage EMI Filter

The integrated choke for a single-stage EMI filter as shown in Figure 4.1(a) consists of ER core, I core, and toroidal core. The central limb of the ER core is placed into

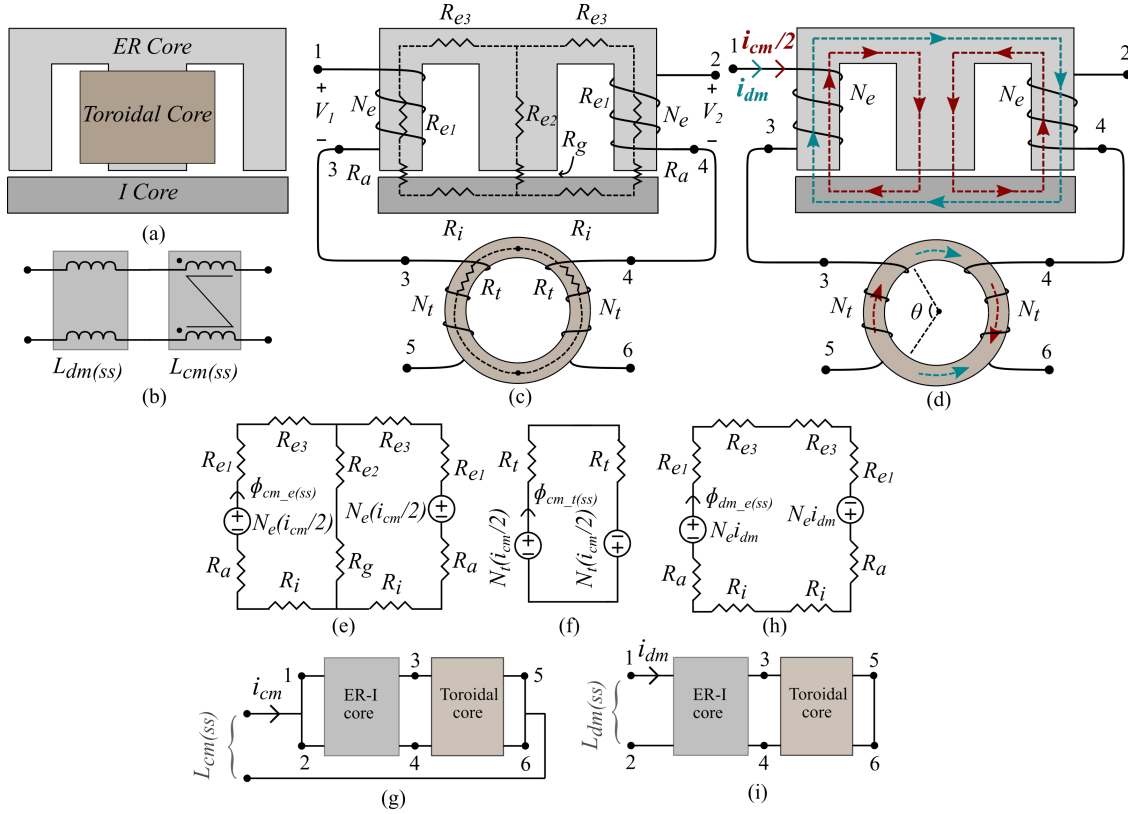


Figure 4.1: Integrated choke for single-stage EMI filter. (a) ER, I, and toroidal cores arrangement, (b) electrical equivalence, (c) winding structure and terminal connections, (d) flux due to i_{cm} and i_{dm} currents in the presented choke, (e) magnetic equivalent circuit of ER and I cores with i_{cm} current, (f) magnetic equivalent circuit of the toroidal core with i_{cm} current, (g) terminal connection to measure $L_{cm(ss)}$, (h) magnetic equivalent circuit of ER and I cores with i_{dm} current, and (i) terminal connection to measure $L_{dm(ss)}$ inductance.

the window area of the toroidal core and the I core is placed on top of the ER core.

The electrical equivalence of the presented choke, with the CM inductance ($L_{cm(ss)}$) and the DM inductance ($L_{dm(ss)}$), is shown in Figure 4.1(b). In Figure 4.1(c), N_e and N_t denote the number of turns on the ER core and toroidal core, respectively; V_1 and V_2 are the voltages induced in the windings mounted on the outer limbs of ER core; R_{e1} , R_{e2} , and R_{e3} are the reluctance of ER core; R_i and R_t are the reluctance of the I core and toroidal core, respectively; where, R_a and R_g denote the air-gap reluctance of the outer and central limb of ER core, respectively. The reluctance in k^{th} section (R_k) of the presented choke is given by

$$R_k = \frac{l_k}{\mu_o \mu_{rk} A_k} \quad (4.1)$$

where l_k , A_k , μ_{rk} are the mean magnetic path length, cross-sectional area, and relative permeability corresponding to k^{th} section respectively; μ_o is the relative permeability of free space. The theoretical estimation of $L_{cm(ss)}$ and $L_{dm(ss)}$ inductance of the presented integrated choke for the single-stage filter is presented

below.

4.2.1 CM Inductance

The flux due to the CM current (i_{cm}) in the ER, I, and toroidal cores of the presented choke is indicated by the red color in Figure 4.1(d). With the winding arrangement shown in Figure 4.1(d), the CM flux exists in the central limb and is canceled out in the outer limb. Thus, the magnetic circuit of the combined ER and I cores is shown in Figure 4.1(e). In Figure 4.1(e), the flux ($\phi_{cm.e(ss)}$) due to i_{cm} current in ER and I core can be written as

$$\phi_{cm.e(ss)} = \frac{N_e(i_{cm}/2)}{R_{e1} + 2R_{e2} + R_{e3} + R_a + 2R_g + R_i} \quad (4.2)$$

As i_{cm} current results in equal voltages across each winding of the ER core, the voltages (V_1 and V_2) can be expressed by neglecting the winding resistance as

$$\begin{aligned} V_1 = V_2 &= N_e \frac{d\phi_{cm.e(ss)}}{dt} \\ &= \frac{N_e^2}{2} \left(\frac{1}{R_{e1} + 2R_{e2} + R_{e3} + R_a + 2R_g + R_i} \right) \frac{di_{cm}}{dt} \end{aligned} \quad (4.3)$$

However, the CM voltage (V_{cm}) due to the i_{cm} current is expressed in terms of the CM inductance ($L_{cm.e(ss)}$) offered by the combined ER and I cores as

$$V_{cm} = L_{cm.e(ss)} \frac{di_{cm}}{dt} \quad (4.4)$$

As $V_{cm} = V_1 = V_2$, the $L_{cm.e(ss)}$ inductance is obtained by comparing (4.3) and (4.4) as

$$L_{cm.e(ss)} = \frac{N_e^2}{2} \left(\frac{1}{R_{e1} + 2R_{e2} + R_{e3} + R_a + 2R_g + R_i} \right) \quad (4.5)$$

Similarly, the flux in the toroidal core due to the i_{cm} current is shown in red color in Figure 4.1(d), and the corresponding magnetic circuit is shown in Figure 4.1(f). The CM inductance ($L_{cm.t(ss)}$) offered by the toroidal core is given by

$$L_{cm.t(ss)} = \frac{N_t^2}{2R_t} \quad (4.6)$$

Thus, the sum of inductance offered by the combined ER and I core and the inductance offered by the toroidal core contribute to the total CM inductance of the presented choke. Thus, $L_{cm(ss)}$ offered by the presented integrated choke, designed

for a single-stage EMI filter, is obtained using (4.5) and (5.15) and is given by

$$L_{cm(ss)} = \frac{N_t^2}{2R_t} + \frac{N_e^2}{2} \left(\frac{1}{R_{e1} + 2R_{e2} + R_{e3} + R_a + 2R_g + R_i} \right) \quad (4.7)$$

The terminal connection of the integrated choke for the experimental measurement of $L_{cm(ss)}$ inductance is shown in Figure 4.1(g).

4.2.2 DM inductance

The flux due to the DM current (i_{dm}) in the ER, I, and toroidal cores of the presented choke is denoted in blue color in Figure 4.1(d). The corresponding magnetic equivalent circuit of the combined ER and I core is shown in Figure 4.1(h). The flux $\phi_{dm.e(ss)}$ due to the i_{dm} current in ER and I core, shown in Figure 4.1(h), is given by

$$\phi_{dm.e(ss)} = \frac{N_e i_{dm}}{R_{e1} + R_{e3} + R_a + R_i} \quad (4.8)$$

The voltages (V_1 and V_2) induced in the windings due to the i_{dm} current are written by neglecting the winding resistance as

$$V_1 = -V_2 = N_e \frac{d\phi_{dm.e(ss)}}{dt} = \frac{N_e^2}{R_{e1} + R_{e3} + R_a + R_i} \frac{di_{dm}}{dt} \quad (4.9)$$

Further, the DM voltage (V_{dm}) due to the i_{dm} current can be expressed in terms of $L_{dm.e(ss)}$ inductance as

$$V_{dm} = L_{dm.e(ss)} \frac{di_{dm}}{dt} \quad (4.10)$$

As $V_{dm} = V_1 - V_2$, inductance $L_{dm.e(ss)}$ is obtained using (4.9) and (4.10) and is given by

$$L_{dm.e(ss)} = \frac{2N_e^2}{R_{e1} + R_{e3} + R_a + R_i} \quad (4.11)$$

Similarly, the flux due to i_{dm} current in the toroidal core is indicated by the blue color in Figure 4.1(d). The DM inductance ($L_{dm.t(ss)}$) offered by the toroidal is given by

$$L_{dm.t(ss)} = \frac{\mu_o \mu_{dm.eff} A_t N_t^2}{l_{eff}} \quad (4.12)$$

where A_t , $\mu_{dm.eff}$, and l_{eff} are the cross-sectional area of the toroidal core, effective DM permeability, and the effective mean magnetic length, respectively. The l_{eff}

is expressed in terms of the outer diameter (OD), inner diameter (ID) and angle covered by each winding (θ) is given by

$$l_{eff} = \sqrt{\frac{OD^2}{\sqrt{2}} \left(\frac{\theta}{4} + 1 + \sin \frac{\theta}{2} \right)^2 + ID^2 \left(\frac{\theta}{4} - 1 + \sin \frac{\theta}{2} \right)^2} \quad (4.13)$$

The sum of inductances offered by the combined ER and I core and the inductance offered by the toroidal core contributes to the total DM inductance of the presented choke. Thus, the $L_{dm(ss)}$ inductance offered by the presented integrated choke designed for a single-stage EMI filter is obtained using (4.11) and (4.12) and is given by

$$L_{dm(ss)} = \frac{\mu_o \mu_{dm,eff} A_t N_t^2}{l_{eff}} + \frac{2N_e^2}{R_{e1} + R_{e3} + R_a + R_i} \quad (4.14)$$

The terminal connection of the presented integrated choke for the experimental measurement of $L_{dm(ss)}$ inductance is shown in Figure 4.1(i).

4.2.3 Magnetic Flux Density and Saturation

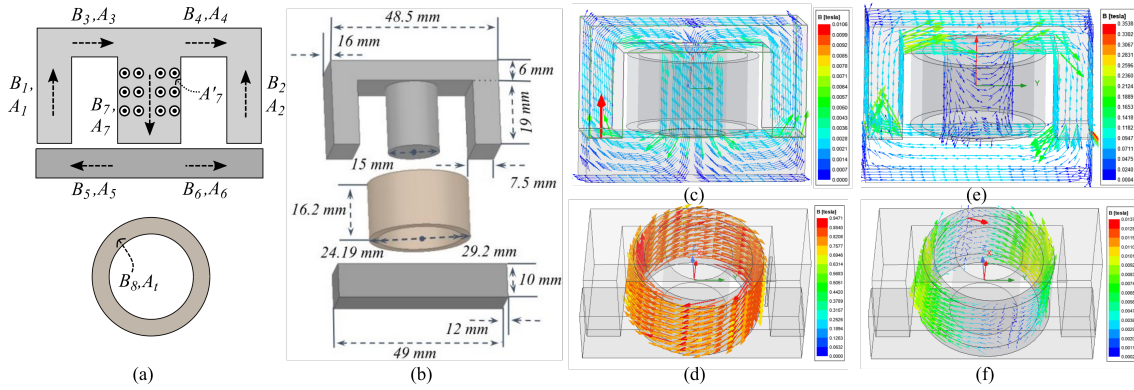


Figure 4.2: (a) Magnetic flux and flux density in various cross-sectional areas of the presented choke, (b) exploded view of the magnetic structure with dimensions of the ER, I, and toroidal cores for ANSYS 3D model, (c) CM flux distribution in ER and I cores, (d) CM flux distribution in the toroidal core, (e) DM flux distribution in ER and I cores, and (f) DM flux distribution in toroidal core.

The magnetic flux density (B_j , $j = \{1, 2, 3, 4, 5, 6, 7, 8\}$) in various sections of the ER, I, and toroidal cores are indicated in Figure 4.2(a). The B_j , ($j = \{1, 2, 3, 4, 5, 6, 7, 8\}$) is expressed in terms of the total flux and the cross-sectional

area of the corresponding section as

$$B_j = \begin{cases} \frac{\phi_{dm.e(ss)} + \phi_{cm.e(ss)}}{A_j}, & j=\{1,3,5\} \\ \frac{\phi_{dm.e(ss)} - \phi_{cm.e(ss)}}{A_j}, & j=\{2,4,6\} \\ \frac{2\phi_{dm.t(ss)}}{A'_j} \hat{x} + \frac{2\phi_{cm.e(ss)}}{A_j} \hat{y}, & j=7 \\ \frac{\phi_{cm.t(ss)} + \phi_{dm.t(ss)}}{A_t}, & j=8 \end{cases} \quad (4.15)$$

where \hat{x} and \hat{y} in (4.15) represent the perpendicular coordinates. By substituting $\phi_{cm.e(ss)}$ and $\phi_{dm.e(ss)}$ from (4.2) and (4.8), respectively, in (4.15), and rewriting the flux $\phi_{cm.t(ss)}$ and $\phi_{dm.t(ss)}$ in terms of $L_{cm.t(ss)}$ and $L_{dm.t(ss)}$ gives the flux density as

$$B_j = \begin{cases} \frac{1}{N_e A_j} \left(\frac{L_{dm.e(ss)} i_{dm}}{2} + L_{cm.e(ss)} i_{cm} \right), & j=\{1,3,5\} \\ \frac{1}{N_e A_j} \left(\frac{L_{dm.e(ss)} i_{dm}}{2} - L_{cm.e(ss)} i_{cm} \right), & j=\{2,4,6\} \\ \sqrt{\left(\frac{L_{dm.t(ss)} i_{dm}}{N_t A'_j} \right)^2 + \left(\frac{2L_{cm.e(ss)} i_{cm}}{N_e A_j} \right)^2}, & j=7 \\ \frac{1}{N_t A_t} \left(L_{cm.t(ss)} i_{cm} + \frac{L_{dm.t(ss)} i_{dm}}{2} \right), & j=8 \end{cases} \quad (4.16)$$

In (4.16), B_1, B_2, B_3, B_4 , and B_7 correspond to the flux density of the ER core; B_5 and B_6 correspond to the flux density of the I core; B_8 is the flux density of the toroidal core. Hence, the conditions for avoiding saturation in ER, I and the toroidal cores of the presented choke can be obtained as

$$\max\{B_1, B_2, B_3, B_4, B_7\} < B_{sat} \text{ of ER core}, \quad (4.17)$$

$$\max\{B_5, B_6\} < B_{sat} \text{ of I core, and} \quad (4.18)$$

$$B_8 < B_{sat} \text{ of toroidal core.} \quad (4.19)$$

where, saturation flux density (B_{sat}) is provided by the manufacturer. The integrated choke in Figure 4.1(a) is simulated in ANSYS 3D MAXWELL, with the dimensions as shown in Figure 4.2(b). The flux distribution in ER and I core with the i_{cm} current are shown in Figure 4.2(c). The flux distribution in the toroidal core is shown in Figure 4.2(d). As depicted in Figure 4.1(d), the CM flux flows through the central limb in the ER core, as seen in Figure 4.2(c) validating the magnetic equivalent circuit of ER and I cores as shown in Figure 4.1(e).

Similarly, the flux distribution in ER and I core, with the i_{dm} current, is shown in Figure 4.2(e), and the flux distribution in the toroidal core is shown in Figure 4.2(f). As seen in Figure 4.2(e) and (f), the flux in the central limb of the ER core corresponds to the DM flux of the toroidal core; this results in an increase in the $\mu_{dm.eff}$ and thereby contributing to further increase in the DM inductance of the presented choke [58], [36], thus validating the magnetic equivalent circuit of ER and

I core, as shown in Figure 4.1(h).

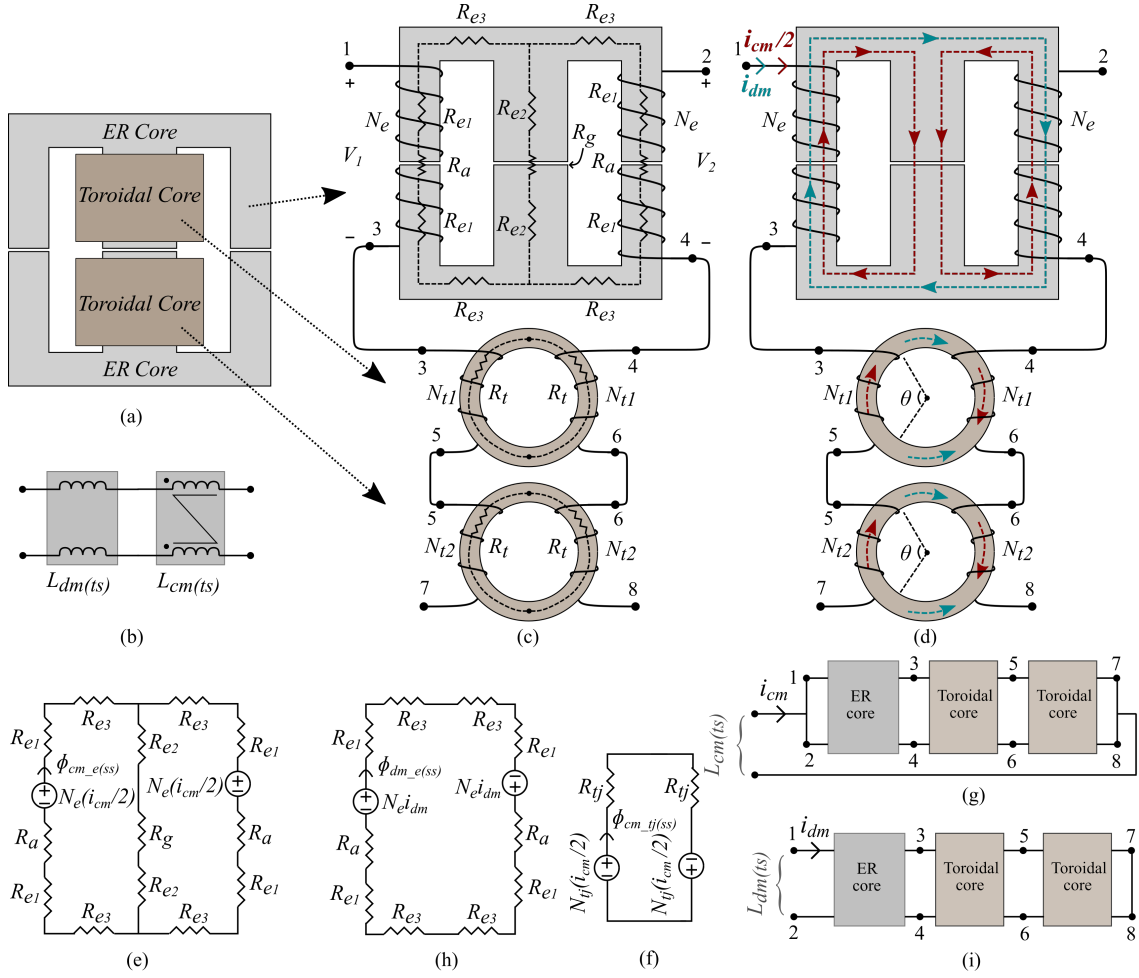


Figure 4.3: Integrated choke for two-stage EMI filter. (a) ER and two toroidal cores arrangement, (b) electrical equivalence, (c) winding structure and terminal connections, (d) flux due to i_{cm} and i_{dm} currents in the presented choke, (e) magnetic equivalent circuit of ER cores with i_{cm} current, (f) magnetic equivalent circuit of the toroidal core with i_{cm} current, (g) terminal connection to measure $L_{cm}(ts)$, (h) magnetic equivalent circuit of ER cores with i_{dm} current, and (i) terminal connection to measure $L_{dm}(ts)$ inductance.

The magnetic flux distribution in ER and I core with $i_{cm} = 500mA$ and $i_{dm} = 4A$ is shown in Figures 4.2(c) and (d), respectively. It is observed from 4.2(c) and (d) that the maximum magnetic flux density in the ER and I cores are about 0.1 T; which is less than the $B_{sat} = 0.5$ T for ferrite core material. The magnetic flux distribution in the toroidal core is shown in Figures 4.2(e) and (f), respectively. It is observed from Figures 4.2(e) and (f) that, the maximum magnetic flux density in the toroidal core is about 0.9 T which is less than the $B_{sat} = 1.2$ T for nanocrystalline core material [59].

Therefore, the following inferences can be drawn from the above discussion as follows:

1. The toroidal core primarily contributes to the CM inductance, therefore the $L_{cm.t(ss)}$ component dominates in the $L_{cm.ss}$ inductance. Hence, the maximum

magnetic flux density in the toroidal core is depicted by the CM flux in the core.

2. The DM flux of both the toroidal and the combined ER and I core contribute to the $L_{dm(ss)}$ inductance of the presented choke. Hence, the maximum magnetic flux density in the ER and I cores is depicted by the DM flux in the respective cores.

4.3 Integrated Choke for Two-Stage EMI Filter

The integrated choke for a two-stage EMI filter as shown in Figure 4.3(a) consists of one ER core and two toroidal cores. It is constructed by placing the central limb of the ER core into the window area of two toroidal cores.

The electrical equivalence of the presented choke, with the CM inductance ($L_{cm(ts)}$) and the DM inductance ($L_{dm(ts)}$), is as shown in Figure 4.3(b). The winding arrangement of the presented choke is shown in Figure 4.3(c), where N_e and N_{tj} , $j = \{1, 2\}$, denote the number of turns on the ER core and toroidal core, respectively. V_1 and V_2 are the voltages induced in the windings mounted on the outer limbs of the ER core. R_{e1} , R_{e2} , and R_{e3} are the reluctance of ER core. R_t is the reluctance of the toroidal core. R_a and R_g denote the air-gap reluctance of the outer and central limb of the ER core, respectively. The reluctance in k^{th} section (R_k) can be written from (4.1). The theoretical estimation of $L_{cm(ts)}$ and $L_{dm(ts)}$ of the two-stage integrated choke is presented below.

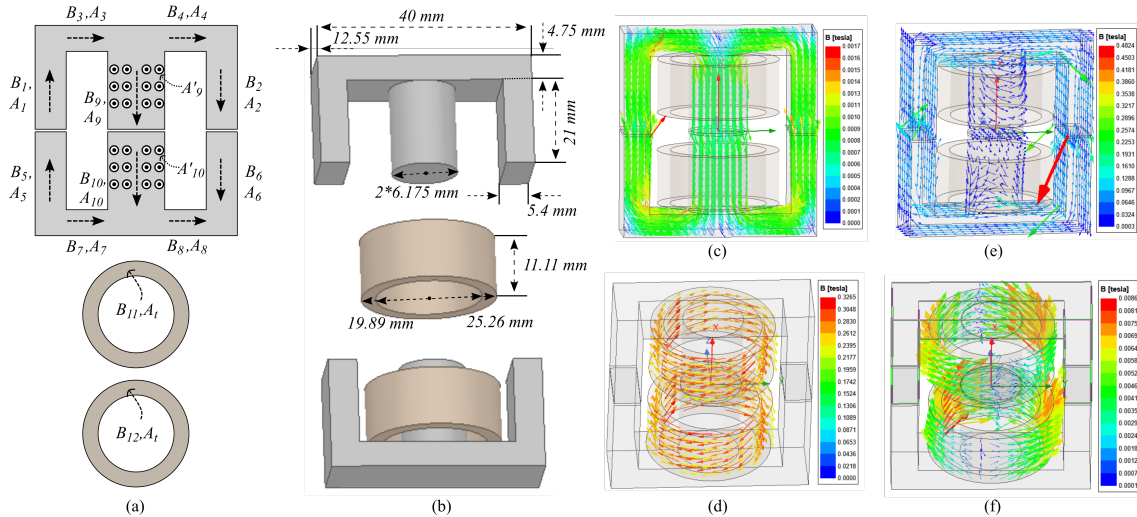


Figure 4.4: (a) Magnetic flux and flux density in various cross-sectional areas of the presented choke (b) exploded view of the magnetic structure with dimensions of the ER and toroidal cores for ANSYS 3D model, (c) CM flux distribution in ER cores, (d) CM flux distribution in the two toroidal core, (e) DM flux distribution in ER cores, and (f) DM flux distribution in the two toroidal core.

4.3.1 CM Inductance

The flux due to the i_{cm} current in the ER and toroidal cores of the presented choke is indicated by the red color in Figure 4.3(d). With the winding arrangement as shown in Figure 4.3(d), the CM flux is only established in the central limb and canceled out in the outer limb. The magnetic circuit of the ER core with i_{cm} current is shown in Figure 4.3(e). From Figure 4.3(e), the flux ($\phi_{cm.e(ts)}$) can be written as

$$\phi_{cm.e(ts)} = \frac{N_e(i_{cm}/2)}{2R_{e1} + 4R_{e2} + 2R_{e3} + R_a + 2R_g} \quad (4.20)$$

The voltages (V_1 and V_2) due to the i_{cm} current can be written by neglecting the winding resistance as

$$\begin{aligned} V_1 = V_2 &= N_e \frac{d\phi_{cm.e(ts)}}{dt} \\ &= \frac{N_e^2}{2} \left(\frac{1}{2R_{e1} + 4R_{e2} + 2R_{e3} + R_a + 2R_g} \right) \frac{di_{cm}}{dt} \end{aligned} \quad (4.21)$$

However, V_{cm} is equal to V_1 and V_2 for i_{cm} current. Hence, the CM inductance ($L_{cm.e(ts)}$) offered by the ER core is obtained comparing (4.4) and (4.21) and given by

$$L_{cm.e(ts)} = \frac{N_e^2}{2} \left(\frac{1}{2R_{e1} + 4R_{e2} + 2R_{e3} + R_a + 2R_g} \right) \quad (4.22)$$

Similarly, the flux in the toroidal core due to the i_{cm} current is shown in Figure 4.3(d) (red). The corresponding magnetic equivalent circuit is shown in Figure 4.3(f). The CM inductances ($L_{cm.t1(ts)}$) and ($L_{cm.t2(ts)}$), offered by the toroidal cores with N_{t1} and N_{t2} turns, are given by

$$L_{cm.tj(ts)} = \frac{N_{tj}^2}{2R_t}; \quad j = \{1, 2\} \quad (4.23)$$

Thus, the sum of inductances ($L_{cm.e(ts)}, L_{cm.tj(ts)}$) offered by the ER core and the toroidal cores gives the total CM inductance of the presented choke. Thus, the inductance offered by the presented integrated choke ($L_{cm(ts)}$), designed for a two-stage EMI filter, is derived from (4.22) and (4.23) and given by

$$L_{cm(ts)} = \frac{1}{2R_t} \sum_{j=1,2} N_{tj}^2 + \frac{N_e^2}{2} \left(\frac{1}{2R_{e1} + 4R_{e2} + 2R_{e3} + R_a + 2R_g} \right) \quad (4.24)$$

The terminal connection of the presented integrated choke for the experimental measurement of $L_{cm(ts)}$ is shown in Figure 4.3(g).

4.3.2 DM inductance

The flux due to i_{dm} current in the ER and toroidal cores of the presented choke is shown in Figure 4.3(d) (blue). The corresponding magnetic equivalent circuit is shown in Figure 4.3(h). In Figure 4.3(h), the flux ($\phi_{dm.e}$) due to the i_{dm} current in the ER core is written as

$$\phi_{dm.e(ts)} = \frac{N_e i_{dm}}{2R_{e1} + 2R_{e3} + R_a} \quad (4.25)$$

The voltages (V_1 and V_2) due to i_{dm} current are given by neglecting the winding resistance as

$$V_1 = -V_2 = N_e \frac{d\phi_{dm.e(ts)}}{dt} = \frac{N_e^2}{2R_{e1} + 2R_{e3} + R_a} \frac{di_{dm}}{dt} \quad (4.26)$$

Since, V_{dm} is equal to $(V_1 - V_2)$, $L_{dm.e(ts)}$ is obtained by comparing (4.10) and (4.26) and given by

$$L_{dm.e(ts)} = \frac{2N_e^2}{2R_{e1} + 2R_{e3} + R_a} \quad (4.27)$$

Similarly, the flux due to the i_{dm} current in the toroidal cores is indicated by the blue color in Figure 4.3(d). The DM inductances ($L_{dm.tj}$, $j = \{1, 2\}$), offered by the toroidal cores, are given by

$$L_{dm.tj(ts)} = \frac{\mu_o \mu_{dm.eff} A_t N_{jt}^2}{l_{eff}}; \quad j = \{1, 2\} \quad (4.28)$$

Thus, the sum of $L_{dm.e(ts)}$, $L_{dm.t1(ts)}$ and $L_{dm.t2(ts)}$ gives the total DM inductance offered by the integrated choke. Therefore, the $L_{dm(ts)}$ of the choke designed for a two-stage EMI filter is given by

$$L_{dm(ts)} = \frac{\mu_o \mu_{dm.eff} A_t}{l_{eff}} \sum_{j=1,2} N_{tj}^2 + \frac{2N_e^2}{2R_{e1} + 2R_{e3} + R_a} \quad (4.29)$$

The terminal connection of the integrated choke for measuring $L_{dm(ts)}$ is shown in Figure 4.3(i).

4.3.3 Magnetic Flux Density and Saturation

The flux density in various sections (B_j , $j = \{1, 2, 3, 4, 5, 6, 7, 8, 9, 10, 11, 12\}$) of the presented integrated choke is indicated in Figure 4.4(a). The B_j is written in terms of the total flux and the cross-sectional area of the corresponding section as

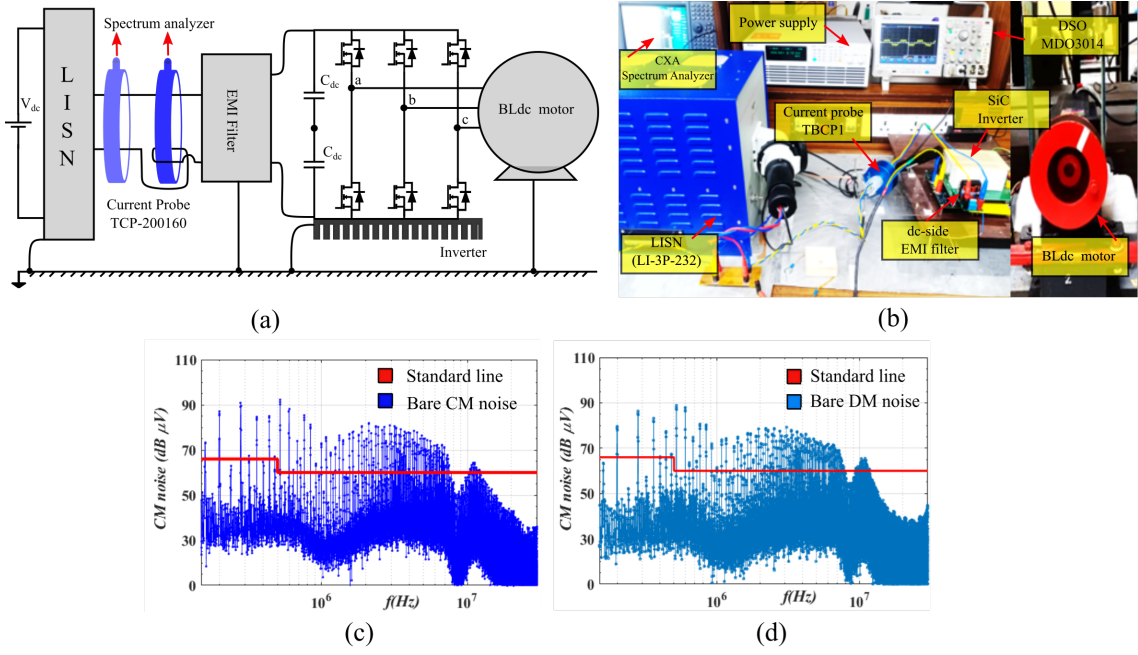


Figure 4.5: (a) Experimental diagram to measure CM and DM noise for BLDC drive system, (b) laboratory setup for EMI test, (c) bare CM noise, and (d) bare DM noise.

$$B_j = \begin{cases} \frac{\phi_{dm-e}(ts) + \phi_{cm-e}(ts)}{A_j}, & j=\{1,3,5,7\} \\ \frac{\phi_{dm-e}(ts) - \phi_{cm-e}(ts)}{A_j}, & j=\{2,4,6,8\} \\ \frac{2\phi_{dm-t}(ts)}{A'_j} \hat{x} + \frac{2\phi_{cm-e}(ts)}{A_j} \hat{y}, & j=\{9,10\} \\ \frac{\phi_{cm-t}(ts) + \phi_{dm-t}(ts)}{A_t}, & j=\{11,12\} \end{cases} \quad (4.30)$$

where \hat{x} and \hat{y} in (4.30) represent the perpendicular coordinates. By substituting $\phi_{cm-e}(ts)$ and $\phi_{dm-e}(ts)$ from (4.20) and (4.25), respectively, and rewriting $\phi_{cm-t}(ts)$ and $\phi_{dm-t}(ts)$ in terms of $L_{cm-t}(ts)$ and $L_{dm-t}(ts)$ in (4.30) gives

$$B_j = \begin{cases} \frac{1}{N_e A_j} \left(\frac{L_{dm-e}(ts) i_{dm}}{2} + L_{cm-e}(ts) i_{cm} \right), & j=\{1,3,5,7\} \\ \frac{1}{N_e A_j} \left(\frac{L_{dm-e}(ts) i_{dm}}{2} - L_{cm-e}(ts) i_{cm} \right), & j=\{2,4,6,8\} \\ \sqrt{\left(\frac{L_{dm-t}(ts) i_{dm}}{N_t A'_j} \right)^2 + \left(\frac{2L_{cm-e}(ts) i_{cm}}{N_e A_j} \right)^2}, & j=\{9,10\} \\ \frac{1}{N_{tj} A_t} \left(L_{cm-tj}(ts) i_{cm} + \frac{L_{dm-tj}(ts) i_{dm}}{2} \right), & j=\{11,12\} \end{cases} \quad (4.31)$$

Thus, (4.31) gives the magnetic flux density in various sections of the presented choke. In (4.31), the B_1 to B_{10} corresponds to the flux density of the ER core and the flux densities B_{11} and B_{12} correspond to the toroidal cores. Hence, the

conditions for the presented choke to avoid saturation are given by

$$\max\{B_1, B_2, B_3, B_4, B_5, B_7, B_8, B_9, B_{10}\} < B_{sat} \text{ of ER core,} \quad (4.32)$$

$$\max\{B_{11}, B_{12}\} < B_{sat} \text{ of toroidal core.} \quad (4.33)$$

The integrated choke shown in Figure 4.3(a) is simulated in ANSYS 3D MAXWELL, with the dimensions as shown in Figure 4.4(b). The flux distribution in the ER core with the i_{cm} current is shown in Figure 4.4(c). Figure 4.4(d) shows the flux distribution in the toroidal core. As depicted in Figure 4.4(c), the CM flux flows through the central limb in the ER core. Thus, validating the magnetic equivalent circuit of the ER core in Figure 4.3(e).

Similarly, the flux distribution in the ER core, with the i_{dm} current, is shown in Figure 4.4(e), and the flux distribution in the toroidal core is shown in Figure 4.4(f). As seen in Figures 4.4(e) and (f), the flux in the central limb of the ER core corresponds to the DM flux of the toroidal core and results in an increase in the μ_{dm_eff} which increase the DM inductance of the presented choke further [58, 36]. The flux distribution in ER and toroidal core with $i_{cm} = 500$ mA is shown in Figures 4.4(c) and (d), respectively. Similarly, the flux distribution in the ER and toroidal core with $i_{dm} = 4$ A is shown in Figures 4.4(e) and (f), respectively. It is observed from Figures 4.4(c) and (e) that the maximum flux density in the ER core is around 0.2 T; which is less than the $B_{sat} = 0.5$ T for ferrite core material. It is observed from Figures 4.4(d) and (f) that, the maximum flux density in the toroidal core is around 0.3 T which is less than the $B_{sat} = 1.2$ T for nanocrystalline core material. Therefore, the following inferences can be drawn from the above discussion as follows.

1. The ER core predominantly contributes to the DM inductance of the presented choke, with the maximum flux density being directly associated with the DM flux generated within the ER core.
2. The toroidal core predominantly contributes to the CM inductance of the presented choke, with the maximum flux density being directly associated with the CM flux generated within the toroidal core.

4.4 Experiment Results and Discussion

The performance of the single-stage and two-stage EMI filters incorporating the conventional and presented chokes has been validated on a three-phase SiC-fed BLDC motor drive operated with the modified bipolar PWM technique [52], shown in Figure 4.5(a). The control technique is implemented using a DSP-based digital

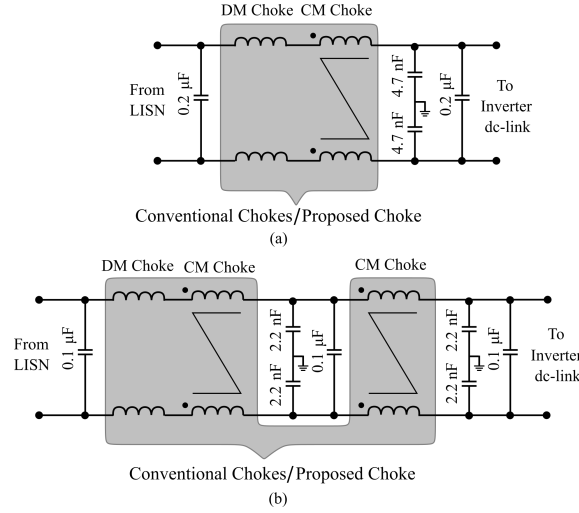


Figure 4.6: (a) Single-stage EMI filter and (b) two-stage EMI filter.

signal controller (TMS320F28379D). The experimental setup, as shown in Figure 4.5(b), consists of a SiC inverter (switching at 50 kHz); 1 kW, 310 V BLDC motor with inbuilt hall sensors; a LISN; high-bandwidth current probe (TBCP1-150) arrangement to measure the CM and DM noise. The current probe is connected to a spectrum analyzer (Cx9000B) to measure the CM and DM noise of the BLDC motor drive. The frequency spectra of the bare CM and DM noise are shown in Figures 4.5(c) and (d), respectively. The standard line in Figures 4.5(c) and (d) correspond to the EN5501 EMI standard.

To attenuate the DC-side CM and DM noise of the three-phase BLDC motor drive, the EMI filters are inserted in between the LISN and the inverter, as shown in Figure 4.5(a). The electrical equivalent circuits of the inserted single-stage and two-stage EMI filters are shown in Figures 4.6(a) and (b), respectively. The design procedure of the integrated choke for the single-stage EMI filter is shown in Figure 4.7(a). The $N_{t_{max}}$ and $N_{e_{max}}$ are the maximum allowable turns on the toroidal and ER core, respectively, of the integrated choke shown in Figure 4.7(c). The A to J in the geometrical constraints shown in Figure 4.7(a) indicate the dimensions shown in Figure 4.7(c). The design procedure of the integrated choke for the two-stage EMI filter is shown in Figure 4.7(b). The N_{max} refers to the maximum allowable turns on the toroidal core of the integrated choke shown in Figure 4.7(d). The A to F in the geometrical constraints shown in Figure 4.7(b) indicate the dimensions shown in Figure 4.7(d). The hardware prototypes for conventional and presented EMI filters are shown in Figures 4.8(a) and (b).

Further, the comparison between the estimated and measured $L_{cm(ss)}$, $L_{dm(ss)}$, $L_{cm(ts)}$ and $L_{dm(ts)}$ inductances is presented. The attenuation performance, thermal performance, PCB area, volume, and weight comparison of the EMI filter with the conventional and presented chokes are also discussed in detail.

Table 4.1: Core Properties

EMI filter	N_e	N_t	R_{e1}	R_{e2}	R_{e3}	R_a	R_g	R_i	$2R_t$
Single-stage	12	20	208417	141528	242759	795775	464202	77367	29813
Two-stage	20	$N_{t1} = 18, N_{t2} = 21$	145800	82484	153960	5871143	3321541	-	125533

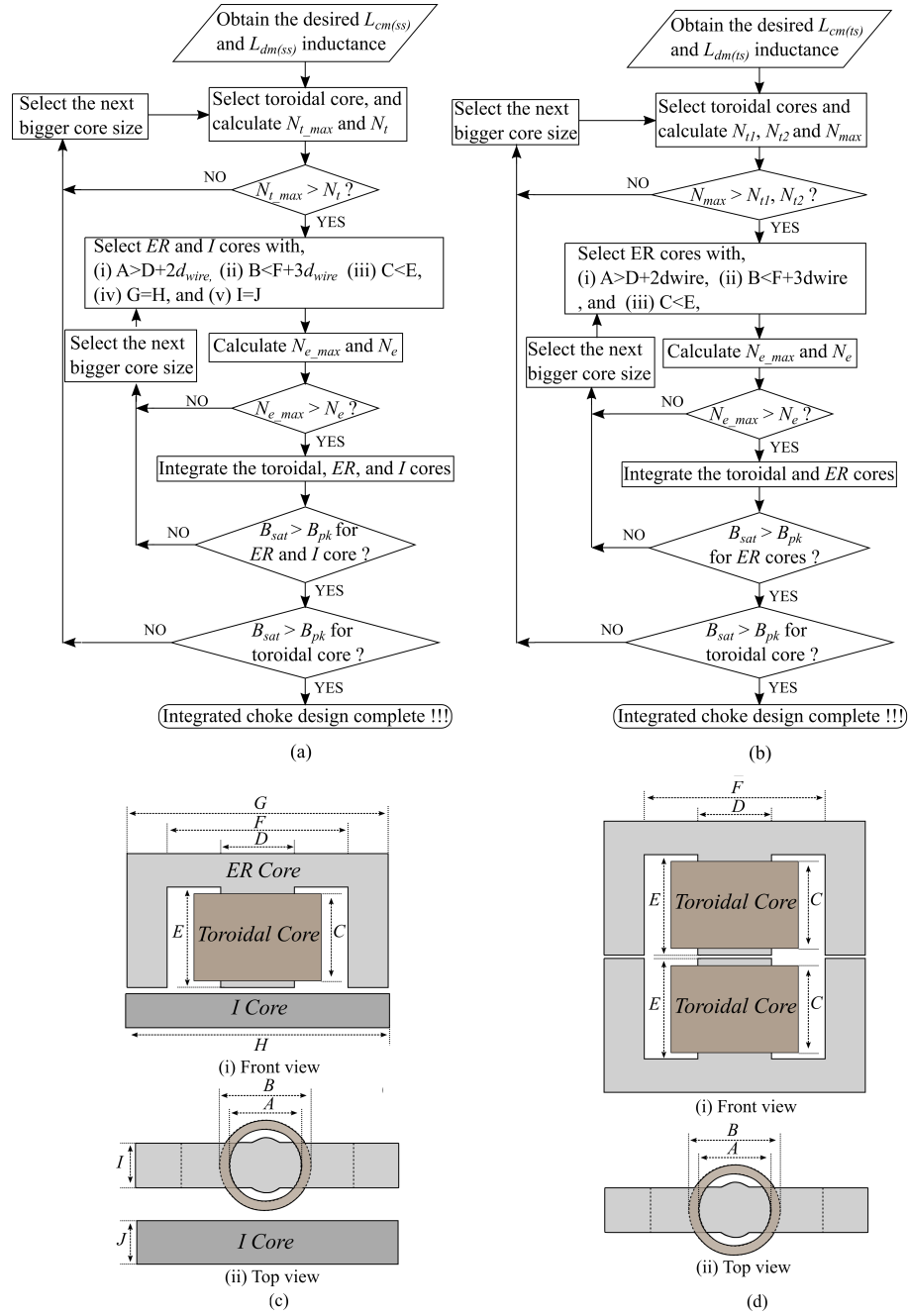


Figure 4.7: Design flowchart and dimensions of the integrated chokes. (a) Design flowchart of integrated choke for single-stage EMI filter, (b) design flowchart of integrated choke for two-stage EMI filter, (c) dimensions for integrated choke for single-stage EMI filter, and (d) dimension for integrated choke for two-stage EMI filter.

4.4.1 Estimation of inductances and attenuation performance of integrated chokes

Estimated and measured value of $L_{cm(ss)}$, $L_{dm(ss)}$, $L_{cm(ts)}$, and $L_{dm(ts)}$:

The core properties, number of turns, and reluctance of the presented chokes discussed in Chapters 4.2 and 4.3 are listed in Table 4.1. The relative permeability

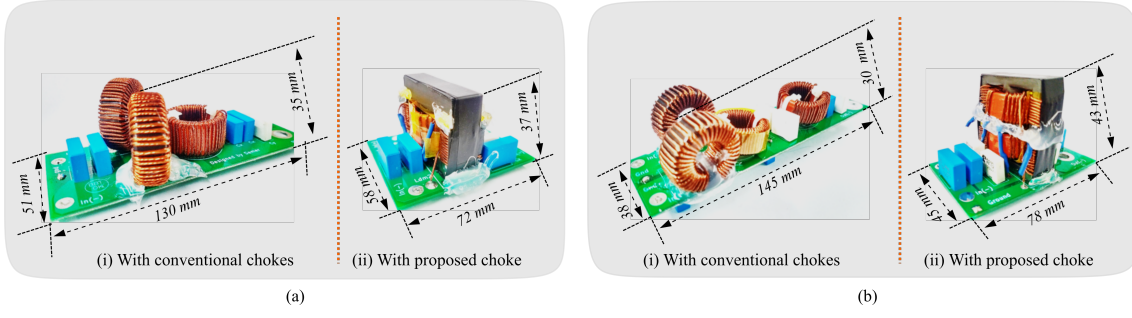


Figure 4.8: DC-side EMI filters. (a) Single-stage EMI filter and (b) two-stage EMI filter.

of the ER, I, and toroidal core of the presented choke used in the single-stage EMI filter are 700, 2100, and 55000 respectively. The relative permeability of the ER and toroidal cores of the presented choke, used in the two-stage EMI filter, are 1500 and 15000, respectively.

The inductance $L_{cm(ss)}$, $L_{dm(ss)}$, $L_{cm(ts)}$, and $L_{dm(ts)}$ estimated from (4.7), (4.14), (4.24), and (4.29), respectively, and the corresponding measured values are given in Table 4.2. It is observed from Table 4.2 that the estimated $L_{cm(ss)}$ and $L_{cm(ts)}$ match with the measured values to a greater extent. The measured $L_{dm(ss)}$ and $L_{dm(ts)}$ are higher than the estimated values. This is because of the increase in the effective permeability of the toroidal core after inserting the ER core into the window area of the toroidal core [36].

The core properties and the number of turns incorporated in single-stage and two-stage EMI filters with the conventional chokes are listed in Table 4.3. The CM and DM impedance of the single-stage EMI filter with the conventional and the presented chokes, as discussed in Chapter 4.2, are shown in Figures 4.9(a) and (b), respectively. The CM and DM impedance of the two-stage EMI filter with

Table 4.2: Estimated and Measured $L_{cm(ss)}$, $L_{dm(ss)}$, $L_{cm(ts)}$, and $L_{dm(ts)}$ Inductance

	$L_{cm(ss)}$	$L_{dm(ss)}$	$L_{cm(ts)}$	$L_{dm(ts)}$
Estimated	13.4 mH	242.9 μ H	6.10 mH	164.6 μ H
Measured	12.8 mH	301.4 μ H	5.90 mH	178.7 μ H

the conventional and the presented chokes, as discussed in Chapter 4.3, are shown in Figures 4.9(c) and (d), respectively. It is observed from Figure 4.9 that the EMI filters with the conventional and presented chokes offer similar CM and DM impedance.

Table 4.3: Conventional CM and DM choke details

EMI filter	CM choke			DM choke		
	L_{cm}	Core	N*	L_{dm}	Core	N*
Single- stage	12.8 mH (1 No.)	W67602	20	120 μ H (2 No.)	S130060 215943	45
Two- stage	3.5 mH (1 No.)	VAC-	20	60 μ H	HJS106026	37
	2.5 mH (1 No.)	W621	17	(2 No.)	215174	

* N denotes the number of turns.

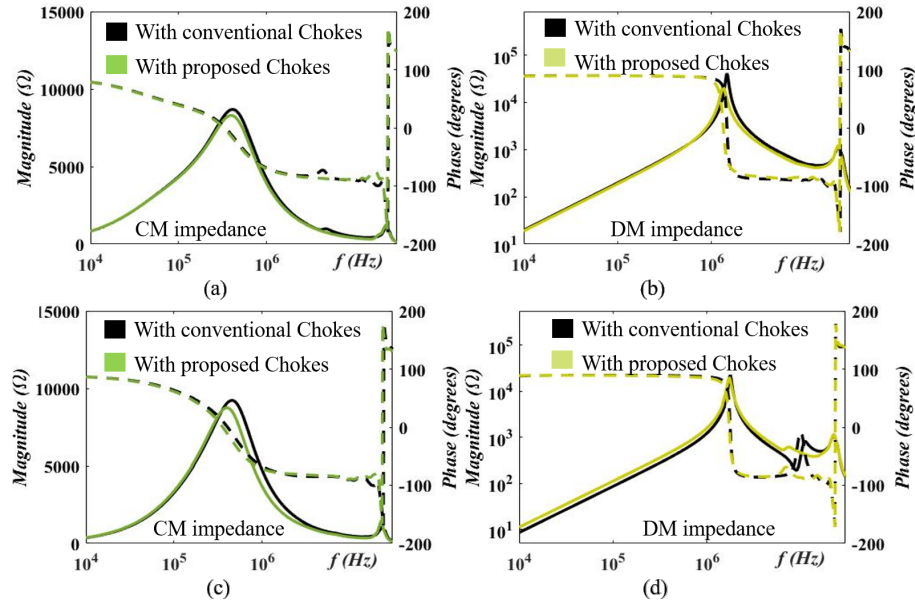


Figure 4.9: Measured impedance (solid line) and phase (dotted line) of presented and conventional EMI choke. (a) CM impedance of presented and conventional EMI choke for single-stage, (b) DM impedance of presented and conventional EMI choke for single-stage, (c) CM impedance of presented and conventional EMI choke for two-stage, and (d) DM impedance of presented and conventional EMI choke for two-stage.

Attenuation performance of EMI filters with conventional and presented chokes:

The measured bare CM and DM noise at the DC side of the motor drive system are shown in Figures 4.5(c) and (d), respectively. It is observed from Figures 4.5(c) and (d) that the CM and DM noise exceed the standard limit. The conventional and the presented EMI filter for single-stage and two-stage is shown in Figures 4.8(a) and (b), respectively. The CM and DM noise obtained by inserting the conventional and

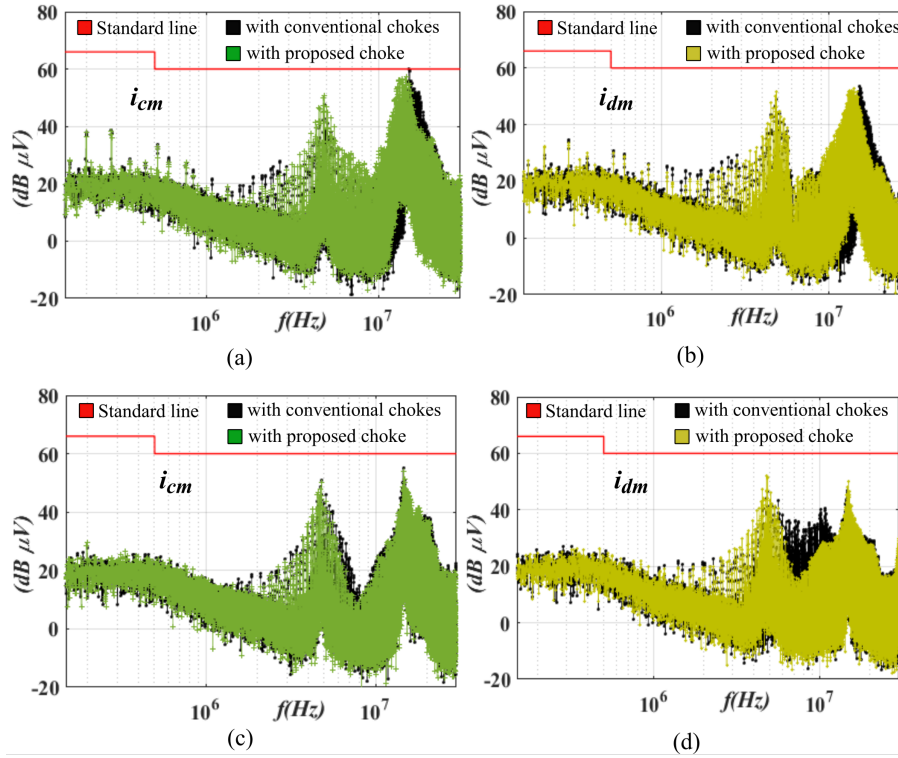


Figure 4.10: EMI performance of the filter. (a) CM performance of conventional and presented single-stage EMI filter (b) DM performance of conventional and presented single-stage EMI filter, (c) CM performance of conventional and presented two-stage EMI filter, and (d) DM performance of conventional and presented two-stage EMI filter.

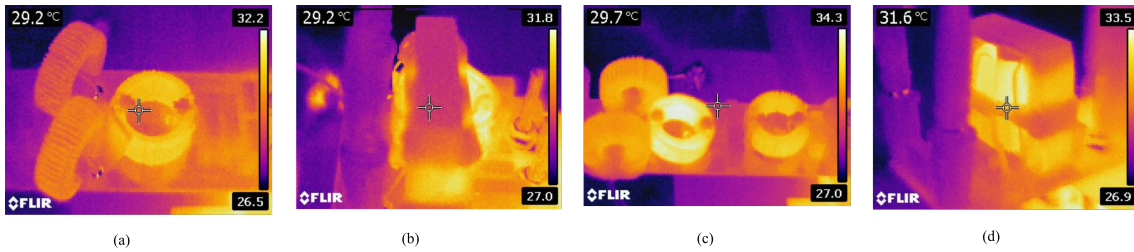


Figure 4.11: Thermal performance of the filter. (a) Conventional single-stage EMI filter (b) integrated single-stage EMI filter, (c) conventional two-stage EMI filter, and (d) integrated two-stage EMI filter.

presented filters shown in Figures 4.8(a)(i) and (ii) is shown in Figures 4.10(a) and (b), respectively. Similarly, the conventional and presented filters shown in Figures 4.8(c)(i) and (ii) result in the CM and DM noise as shown in Figures 4.10(c) and (d), respectively. It is evident from Figure 4.10 that the EMI filter incorporating the conventional and presented chokes offers similar CM and DM noise attenuation performance. In addition, the thermal behavior of the single-stage EMI filters with conventional and presented chokes, with the motor drawing 4 A current, is shown in Figures 4.11(a) and (b), respectively. The thermal behavior of the two-stage EMI filters with conventional and presented chokes is shown in Figures 4.11(c) and (d), respectively. It is observed from Figure 4.11 that, the thermal performance of the

conventional and the presented chokes are similar in both single-stage and two-stage EMI filters.

Thus, the single-stage and two-stage EMI filters with the presented choke provide similar attenuation, and thermal performance as compared to the corresponding EMI filters with conventional chokes. Further, the benefits of the presented chokes in terms of the PCB area, volume, and weight are discussed in detail.

Table 4.4: Comparison Between Conventional and Presented EMI Filter

EMI filter	Type of Choke	PCB Area (mm ²)	Filter	Filter
			Volume (mm ³)	Weight (g)
Single-stage	Conventional	6630	232050	150.5
	presented	4176	154512	152.0
Two-stage	Conventional	5510	165300	118
	presented	3510	150930	121

4.4.2 Comparison of PCB Area, Volume, and Weight of EMI filters with conventional and presented chokes

The PCB area, filter box volume, and filter weight of the single-stage and two-stage EMI filters with conventional and presented chokes are presented in Table ???. The reduction in PCB area and filter box volume of the filter for single-stage are 37% and 34%, respectively, as compared to the conventional chokes used in the single-stage EMI filter. Similarly, the reduction in PCB area and filter box volume of the filter for two-stage are 36% and 9%, respectively, as compared to the conventional chokes used in the two-stage EMI filter. Moreover, it is observed from Table ?? that the presented chokes do not cause a significant increase in the overall EMI filter weight. Thus, employing the presented chokes in single-stage and two-stage EMI filters significantly reduces the PCB area and overall filter volume without considerably increasing the filter weight.

4.4.3 Losses comparison

The losses incurred within the CM and DM chokes of passive EMI filters, aimed at mitigating CM and DM noise, are detailed in Table 4.5. These losses are computed according to the methodology outlined in [27]. For a current of 5 amps and a switching frequency of 50 kHz, the single-stage loss approximates 12 watts. Correspondingly, for the same current and frequency, the two-stage loss amounts to approximately 6.557 watts.

Similarly, for a current of 5 amps and a switching frequency of 50 kHz, the single-stage integrated EMI filter loss approximates 10.176 watts. Correspondingly, for the same current and frequency, the two-stage integrated EMI filter loss amounts to approximately 9.282 watts.

Table 4.5: Loss Comparison Between Conventional and Presented EMI Filters.

EMI filter	Type of Choke	Core loss (W)		Copper loss (W)		Total loss (W)
		CM	DM	CM	DM	
		choke	choke	choke	choke	
Single-stage	Conventional	2.04	0.3	3	6.75	12.09
	presented	2.04	3.0326	3	2.1	10.176
Two-stage	Conventional	1.032	0.2	2.55	2.775	6.557
	presented	1.032	3.9	2.55	1.8	9.282

4.5 Conclusion

The core arrangement and the winding structures of the two presented integrated magnetic chokes for single-stage and two-stage EMI filters, respectively, are discussed in detail. The CM and DM inductance offered by the two presented integrated chokes is estimated from the magnetic equivalent circuits and is verified experimentally. The detailed saturation analysis is presented to estimate the maximum magnetic flux density of the presented chokes. The comparative analysis of the single-stage and two-stage EMI filters with the conventional chokes and the presented chokes is discussed. With the same CM and DM noise attenuation performance, the EMI

filter with presented chokes significantly reduces the PCB area and the box volume of the filter, without considerable change in the weight and thermal performance. In particular, the PCB area of the single-stage and two-stage EMI filter with the presented chokes is reduced by 37% and 36%, respectively, and the box volume is reduced by 34% and 9%, respectively.

Chapter 5

ER and Rectangular Core Based Integrated Chokes for DC-side EMI filters

5.1 Introduction

This chapter presents two integrated choke structures by utilizing the free space of the toroidal cores with larger window areas. One of the integrated choke structures comprises the toroidal and EE core and is suitable for single-stage EMI filters. In this integrated choke structure, the DM inductance of the conventional toroidal CM choke is increased without a change in its box volume. The other integrated choke structure comprises toroidal and rectangular cores and is suitable for two-stage EMI filters. In this integrated choke structure, the CM inductance of the conventional toroidal CM choke is increased without necessitating any alteration to its enclosure volume. This configuration proves particularly advantageous in low-voltage applications, where the inherent leakage inductance of both the CM choke and the accompanying C_x capacitor serve to mitigate the DM component of noise effectively.

This chapter discusses the core and winding arrangement of the two above-mentioned integrated chokes in detail. Additionally, the analytical estimation of their CM and DM inductances is presented along with the experimental validation. Moreover, the reduction in the PCB and volume of the EMI filters incorporating the two integrated chokes when compared to their respective conventional EMI filters is discussed in detail.

5.2 Toroidal-EE-Based Integrated CM Choke for DC-side Single-Stage EMI filters

5.2.1 Design of Integrated Choke

The toroidal CM chokes are widely used in conventional EMI filters to avoid saturation in the CM choke due to its leakage inductance, which contributes to

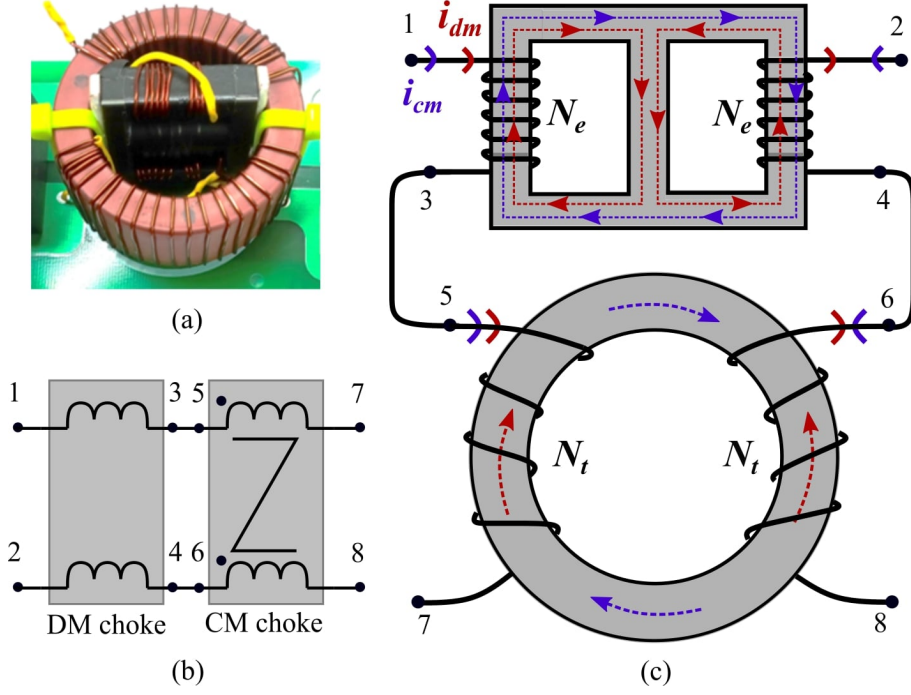


Figure 5.1: (a) Prototype of integrated choke, (b) electrical equivalence of the integrated choke, and (c) winding structure and terminal connection of integrated choke.

the DM inductance. Hence, the presented integrated choke is designed such that, it improves the DM inductance without impacting the saturation of the conventional toroidal CM choke. Unlike the integrated choke presented in [36], the integrated choke provides an increase in DM inductance without an increase in the box volume. The prototype of the integrated choke that constitutes an EE-core inserted in the window area of the toroidal core is shown in Figure 5.1(a). The electrical equivalence of the integrated choke with the CM choke and DM choke is shown in Figure 5.1(b). The winding structure and the terminal connections between the toroidal core and EE-core are shown in Figure 5.1(c). The N_t and N_e denote the number of turns on the toroidal and EE cores, respectively. Further, the CM inductance and the DM inductance of the integrated choke, denoted by $L_{cm-prop}$ and $L_{dm-prop}$, respectively, are analytically estimated.

Estimation of CM inductance

The flux in the toroidal and the EE-core due to the common mode current (i_{cm}) flowing is indicated in Figure 5.1(c) (blue). The corresponding magnetic circuit of the integrated choke with the i_{cm} current flowing is shown in Figure 5.2(a). The R_t denotes half the reluctance of the toroidal core, while R_{e1} and R_{e2} are the reluctance of the outer leg and center leg of the EE core, respectively. Where,

$$R_t = \frac{l_t/2}{\mu_o \mu_{r,t} A_t}, R_{e1} = \frac{l_1}{\mu_o \mu_{r,1} A_1}, \text{ and } R_{e2} = \frac{l_2}{\mu_o \mu_{r,2} A_2}. \quad (5.1)$$

l_t , l_1 , l_2 and l_g are the mean magnetic length of the toroidal core, outer legs of EE-core, center leg of EE-core, and the air gap between the toroidal and EE-core, respectively; while, A_t , A_1 , A_2 and A_g are the area of cross-section of the toroidal core, outer legs of EE-core, center leg of EE-core, and the air gap between the toroidal and EE-core, respectively.

As indicated in Figure 5.1(c), the flux due to i_{cm} current is confined within the toroidal and EE-cores. Thus, the flux due to i_{cm} in toroidal core ($\phi_{cm,t}$) and EE-core ($\phi_{cm,e}$) shown in Figure 5.2(a) are given by,

$$\phi_{cm,t} = \frac{N_t i_{cm}}{R_t} \text{ and } \phi_{cm,e} = \frac{N_e i_{cm}}{R_{e1}} \quad (5.2)$$

Thus, the $L_{cm,prop}$ inductance is given by,

$$L_{cm,prop} = \frac{N_t \phi_{cm,t} + N_e \phi_{cm,e}}{2i_{cm}} = \frac{N_t^2}{2R_t} + \frac{N_e^2}{2R_{e1}} \quad (5.3)$$

Thus, the estimated $L_{cm,prop}$ can be calculated from (5.3), while the terminal connections to experimentally measure the $L_{cm,prop}$ inductance is shown in Figure 5.2(b). Similarly, the CM inductance for the conventional toroidal CM choke ($L_{cm,conv}$) is given by,

$$L_{cm,conv} = \frac{N_t^2}{2R_t} \quad (5.4)$$

From (5.3) and (5.4), the $L_{cm,prop}$ is higher than $L_{cm,conv}$; however, for a low permeability EE-core, the $L_{cm,prop}$ and $L_{cm,conv}$ are approximately equal. Hence, the CM inductance offered by the Toroidal-EE integrated CM choke is the same as that of the conventional choke.

Estimation of DM inductance

The flux in the toroidal and the EE-cores with the DM current (i_{dm}) excitation is shown in Figure 5.1(c) (red). The corresponding equivalent magnetic circuit of the integrated choke is shown in Figure 5.2(c). R_g is the air gap reluctance between toroidal and EE core and is given by,

$$R_g = \frac{l_g}{\mu_o A_g}. \quad (5.5)$$

Where, l_g and A_g are the mean magnetic length and area of the cross-section of the air gap between the toroidal and EE-core, respectively.

It is observed from Figure 5.2(c) that, the leakage flux of the toroidal core ($\phi_{dm,t}$) through the reluctance R_{e2} and the DM flux corresponding to the EE-core outer legs

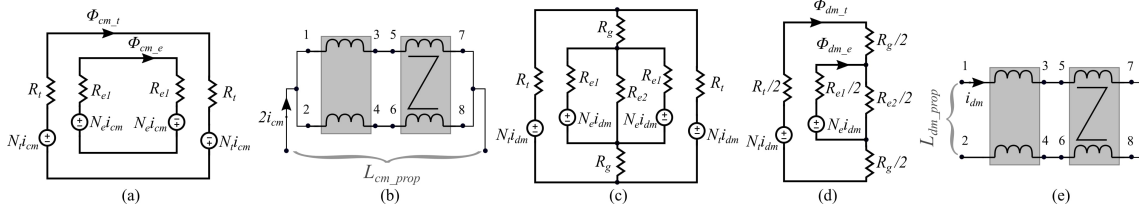


Figure 5.2: (a) Magnetic equivalent circuit with i_{cm} current excitation, (b) terminal connections for the integrated choke to measure the L_{cm_prop} inductance, (c) magnetic equivalent circuit with i_{dm} current excitation, (d) simplified magnetic equivalent circuit with the i_{dm} current excitation, and (e) terminal connections for the integrated choke to measure the L_{dm_prop} inductance.

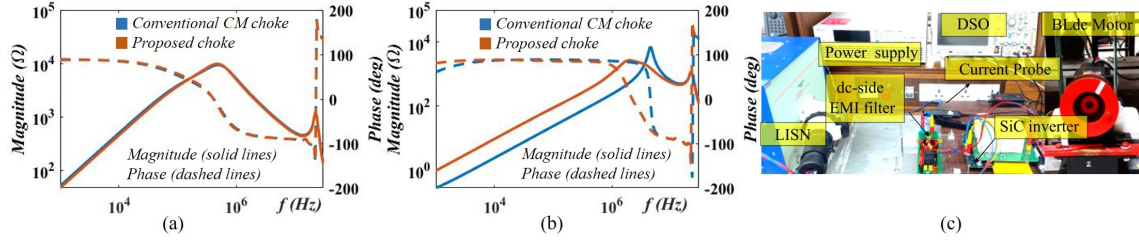


Figure 5.3: Comparison of (a) CM impedance profile of conventional and presented integrated choke, (b) DM impedance profile of conventional and presented integrated choke, and (c) experimental setup of a three-phase Sic-fed BLDC drive.

(ϕ_{dm_e}) through the R_{e2} contribute to the L_{dm_prop} inductance. The ϕ_{dm_t} and ϕ_{dm_e} are given from the simplified magnetic equivalent circuit shown in Figure 5.2(d) as,

$$\phi_{dm_t} = \frac{N_t R_{e1} i_{dm}}{(R_{e1} + R_{e2}) \left[\frac{R_t}{2} + R_g + \left(\frac{R_{e1}}{2} // \frac{R_{e2}}{2} \right) \right]} \text{ and} \quad (5.6)$$

$$\phi_{dm_e} = \frac{N_e \left(\frac{R_t}{2} + R_g \right) i_{dm}}{\left(\frac{R_t}{2} + R_g + \frac{R_t}{2} \right) \left(\frac{R_{e1}}{2} + \left[\left(\frac{R_t}{2} + R_g \right) // \frac{R_{e2}}{2} \right] \right)}. \quad (5.7)$$

Thus, the L_{dm_prop} inductance can be expressed as,

$$\begin{aligned} L_{dm_prop} &= \frac{N_t \phi_{dm_t} + N_e \phi_{dm_e}}{i_{dm}} \\ &= \frac{N_t^2 R_{e1}}{(R_{e1} + R_{e2}) \left[\frac{R_t}{2} + R_g + \left(\frac{R_{e1}}{2} // \frac{R_{e2}}{2} \right) \right]} + \frac{N_e^2 \left(\frac{R_t}{2} + R_g \right)}{\left(\frac{R_t}{2} + R_g + \frac{R_t}{2} \right) \left(\frac{R_{e1}}{2} + \left[\left(\frac{R_t}{2} + R_g \right) // \frac{R_{e2}}{2} \right] \right)} \end{aligned} \quad (5.8)$$

Thus, the estimated L_{dm_prop} can be calculated from (5.8), while the terminal connections to experimentally measure the L_{dm_prop} inductance is shown in Figure 5.2(e). Similarly, the DM inductance of the traditional CM transformer (L_{dm_conv}) is given by,

$$L_{dm_conv} = 2.5 \mu_o N_t^2 \frac{A_t}{l_{eff}} \left(\frac{l_t}{2} \sqrt{\frac{\pi}{A_t}} \right)^{1.45} \quad (5.9)$$

where l_{eff} is the mean magnetic length of the leakage flux of the toroidal core. From (5.8) and (5.9), the L_{dm_prop} is significantly higher than the L_{dm_conv} . Hence, the DM inductance offered by the Toroidal-EE choke is higher than the conventional choke.

5.2.2 Experimental Validation

To verify the presented integrated choke, the Toroidal-EE choke and the discrete inductors are built for testing purposes. Firstly, the analytically estimated value is verified by an impedance analyzer and later the EMI filter is designed to validate the performance of the conventional and integrated choke structures.

Table 5.1: Estimated and Measured L_{cm_prop} , L_{cm_conv} , L_{dm_prop} and L_{dm_conv} inductance

	L_{cm_prop}	L_{cm_conv}	L_{dm_prop}	L_{dm_conv}
Estimated	8.2mH	8.18mH	102.46 μ H	51.82 μ H
Measured	8.18mH	8.2mH	114.1 μ H	46.7 μ H

Small Signal Measurement

To validate the analysis presented in Chapter 5.2.1, the integrated choke is constructed with a toroidal core and an EE-core; while the conventional CM choke constitutes only the toroidal core. The reluctance R_t , R_{e1} , R_{e2} and R_g are calculated from (5.1) and (5.5) as 24444.44 H⁻¹, 534325.0405 H⁻¹, 208375.7891 H⁻¹, and 7957747.155 H⁻¹, respectively. The toroidal core of the conventional CM choke is wound with $N_t = 20$, while the winding turns corresponding to the integrated choke are $N_t = 20$ and $N_e = 5$. For $N_t = 20$ and $N_e = 5$, the inductances L_{cm_prop} , L_{cm_conv} , L_{dm_prop} and L_{dm_conv} are estimated from (5.3), (5.4), (5.8) and (5.9), and are given in Table 5.1. The corresponding experimentally measured L_{cm_prop} , L_{cm_conv} , L_{dm_prop} and L_{dm_conv} inductances using the network analyzer (PSM3750) is listed in Table 5.1.

It is evident from Table 5.1 that, the estimated and the experimentally measured inductances are equal; thus, validating the L_{cm_prop} and L_{dm_prop} inductances by (5.3) and (5.8), respectively. Moreover, as mentioned in Chapter 5.2.1, it is observed from Table 5.1 that, the CM inductance of the Toroidal-EE choke is the same as that of the traditional CM choke. However, the presented integrated choke offers a DM inductance of 67.4 μ H higher than the conventional choke of the same box volume. The CM and DM impedance profiles of the integrated choke and conventional CM choke are shown in Figures 5.3(a) and (b), respectively. Thus, from Figures 5.3(a)

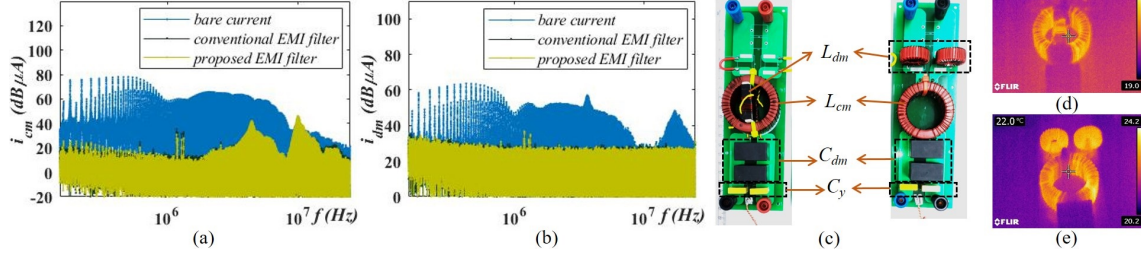


Figure 5.4: (a) Bare CM noise, CM noise with conventional choke, and CM noise with integrated choke for three-phase BLDC motor, (b) Bare DM noise, DM noise with conventional choke, and DM noise with integrated choke, (c) EMI filter with conventional and integrated chokes, (d) thermal image of integrated choke, and (e) thermal image of conventional choke.

and (b), and Table 5.1 it can be concluded that within the same box volume, the integrated choke structure offers higher DM inductance than the conventional CM choke.

Large Signal Measurement

The integrated choke is employed on the DC-side of the three-phase SiC-fed BLDC motor drive shown in Figure 5.3(c). The hardware set-up consists of a three-phase SiC inverter, BLDC motor, power supply, and LISN. The conventional single-stage EMI filter is inserted at the DC-side of the inverter to attenuate the CM current (i_{cm}) and the DM current (i_{dm}) through the LISN. The component values of the EMI filter are $C_y = 100$ nF, $L_{dm} = 100$ μ H, and $C_{dm} = 10$ μ F. The DC-link voltage is 500 V and the motor is loaded for 700 W. The SiC inverter is operated at the 20 kHz switching frequency.

The frequency spectrum of bare i_{cm} current, the i_{cm} current with the conventional EMI filter, and the i_{cm} current with the EMI filter that includes the integrated choke is shown in Figure 5.4(a). Similarly, the frequency spectrum of bare i_{dm} current, the i_{dm} current with the conventional EMI filter, and the i_{dm} current with the EMI filter that incorporates the integrated choke is shown in Figure 5.4(b). It is evident from Figures 5.4(a) and (b) that, the conventional EMI filter and the EMI filter incorporating the integrated choke offer identical attenuation to both the i_{cm} and the i_{dm} currents.

The conventional EMI filter and the EMI filter with the integrated choke are shown in Figure 5.4(c). It is observed from Figure 5.4(c) that, incorporating the integrated choke configuration reduces the overall volume occupied by the EMI filter by around 22%, for the similar CM and DM noise attenuation as that of the conventional EMI filter.

In addition, the thermal behavior of the EMI filter is of great concern in view of designing the high power density converters. Hence, the thermal performance of the

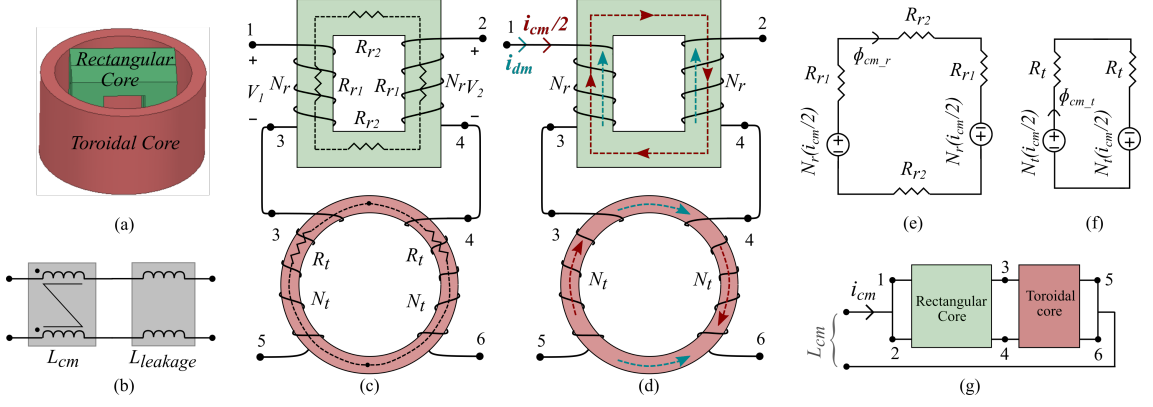


Figure 5.5: Integrated choke. (a) toroidal and rectangular cores arrangement, (b) electrical equivalence, (c) winding structure and terminal connections, (d) flux due to i_{cm} and i_{dm} currents in the integrated choke, (e) magnetic equivalent circuit of the rectangular core with i_{cm} current, (f) magnetic equivalent circuit of the toroidal core with i_{cm} current, and (g) terminal connection to measure L_{cm} inductance.

conventional EMI filter and the EMI filter with the integrated choke is shown in Figures 5.4(d) and (e), respectively. The temperature is measured using a thermal camera (FLIR) after 10 min of steady-state operation at 700 W with natural cooling. The hot-spot temperatures of the conventional and integrated chokes are 24.2 °C and 23 °C, respectively. Thus, it is evident from Figures 5.4(d) and (e) that, the EMI filter with integrated choke offers similar thermal performance as that of the conventional EMI filter.

5.3 Integrated Choke for High-Density Two-Stage Passive DC-Side EMI Filters

5.3.1 Design of Integrated Choke

The presented integrated choke incorporates toroidal and rectangular cores, as illustrated in Fig. 5.5(a). As depicted in the figure, the core configuration of the presented integrated choke involves positioning the rectangular core within the window area of the toroidal core. The electrical equivalence of the presented integrated choke, with the total CM inductance (L_{cm}) and the leakage inductance (L_l), is shown in Fig. 5.5(b). In Fig. 5.5(c), N_r and N_t denote the number of turns on the rectangular core and toroidal core, respectively; V_1 and V_2 are the voltages induced in the windings mounted on the rectangular core; R_{r1} and R_{r2} are the reluctance of the rectangular core; R_t is half the reluctances of the toroidal core.

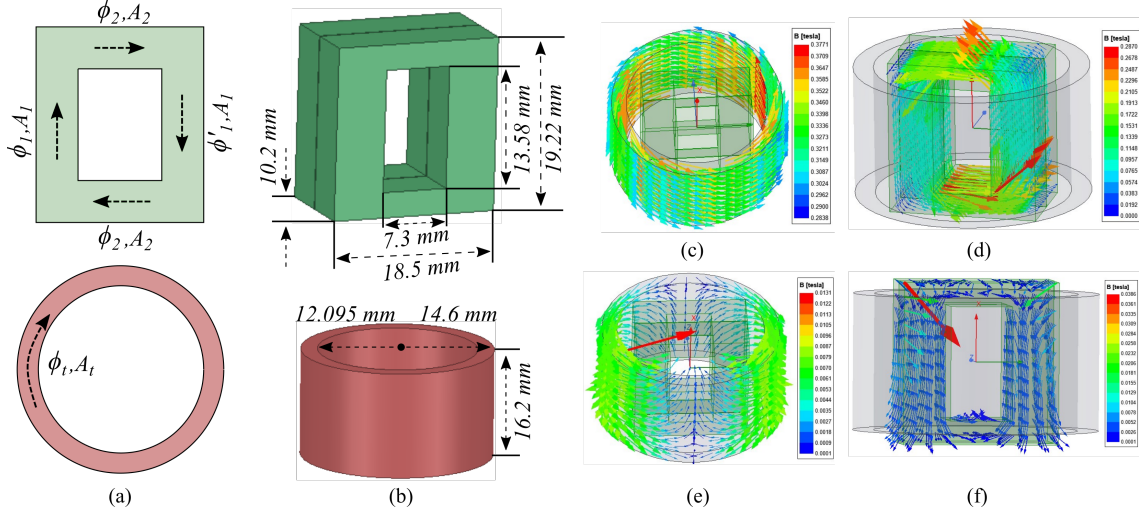


Figure 5.6: (a) Magnetic flux in various cross-sectional areas of the integrated choke, (b) exploded view of the magnetic structure with dimensions of the rectangular and toroidal cores for ANSYS 3D model, (c) CM flux distribution in toroidal cores, (d) CM flux distribution in the rectangular core, (e) DM flux distribution in toroidal cores, and (f) DM flux distribution in rectangular core.

The reluctance in k^{th} section (R_k) of the presented integrated choke is given by

$$R_k = \frac{l_k}{\mu_o \mu_{rk} A_k}. \quad (5.10)$$

where l_k , A_k , and μ_{rk} are the mean magnetic path length, cross-sectional area, and relative permeability corresponding to the k^{th} section, respectively; μ_o is the relative permeability of free space. The theoretical estimation of L_{cm} inductance of the presented integrated choke is further discussed.

5.3.2 Estimation of L_{cm} Inductance

The flux due to the CM current (i_{cm}) in the rectangular and toroidal cores of the presented integrated choke is indicated by the red color in Fig. 5.5(d). Thus, the magnetic circuit of the rectangular core for i_{cm} current excitation is shown in Fig. 5.5(e). In Fig. 5.5(e), the flux ($\phi_{cm,r}$) can be written as,

$$\phi_{cm,r} = \frac{N_r i_{cm}}{2(R_{e1} + R_{e2})}. \quad (5.11)$$

As i_{cm} results in equal voltages across each winding of the rectangular core, the voltages (V_1 and V_2) can be expressed by neglecting the winding resistance as

$$V_1 = V_2 = N_r \frac{d\phi_{cm,r}}{dt} = \frac{N_r^2}{2(R_{e1} + R_{e2})} \frac{di_{cm}}{dt}. \quad (5.12)$$

However, the CM voltage (V_{cm}) due to the i_{cm} is expressed in terms of the CM

inductance (L_{cm}) offered by the rectangular core as,

$$V_{cm} = L_{cm} \frac{di_{cm}}{dt}. \quad (5.13)$$

As $V_{cm} = V_1 = V_2$, the L_{cm} is obtained by comparing (5.12) and (5.13) as,

$$L_{cm.r} = \frac{N_r^2}{2(R_{e1} + R_{e2})}. \quad (5.14)$$

Similarly, the flux in the toroidal core due to i_{cm} is shown in red color in Fig. 5.5(d), and the corresponding magnetic circuit is shown in Fig. 5.5(f). The CM inductance ($L_{cm.t}$) offered by the toroidal core is given by,

$$L_{cm.t} = \frac{N_t^2}{2R_t}. \quad (5.15)$$

Thus, the sum of inductances offered by the combined rectangular and toroidal cores contributes to the total CM inductance of the presented integrated choke. The L_{cm} offered by the presented integrated choke is obtained from (5.14) and (5.15) as,

$$L_{cm} = L_{cm.t} + L_{cm.r} = \frac{N_t^2}{2R_t} + \frac{N_r^2}{2(R_{e1} + R_{e2})}. \quad (5.16)$$

The terminal connection of the presented integrated choke for the experimental measurement of L_{cm} is shown in Fig. 5.5(g).

5.3.3 Magnetic Flux Density and Saturation

The flux in the rectangular and toroidal cores depends on the DM and CM flux. The net flux generated by the i_{cm} and i_{dm} currents in various sections of the rectangular and toroidal cores are shown in Fig. 5.6(a). From i_{cm} and i_{dm} current excitation shown in Fig. 5.5(d), the resultant flux in the various sections of the rectangular core indicated in Fig. 5.6(a) is given by,

$$\phi_1 = \phi_{cm.r} + \phi_{dm.r} = \frac{L_{cm.r}i_{cm}}{N_r} + \frac{L_{dm.r}i_{dm}}{2N_r}, \quad (5.17)$$

$$\phi_1' = \phi_{cm.r} - \phi_{dm.r} = \frac{L_{cm.r}i_{cm}}{N_r} - \frac{L_{dm.r}i_{dm}}{2N_r}, \text{ and} \quad (5.18)$$

$$\phi_2 = \phi_{cm.r} = \frac{L_{cm.r}i_{cm}}{N_r}. \quad (5.19)$$

As evident from Figs. 5.6(a), the ϕ_1 and ϕ_1' fluxes flow through the area of cross-section, A_1 . From (5.17) and (5.18), it is evident that, ϕ_1 results in higher magnetic flux density than ϕ_1' . Thus, the magnetic flux densities, B_1 and B_2

corresponding to ϕ_1 and ϕ_2 , respectively, can be expressed as,

$$B_1 = \frac{\phi_1}{A_1} = \frac{1}{N_r A_1} \left(L_{cm,r} i_{cm} + \frac{L_{dm,r} i_{dm}}{2} \right) \text{ and} \quad (5.20)$$

$$B_2 = \frac{\phi_2}{A_2} = \frac{1}{N_r A_2} (L_{cm,r} i_{cm}), \quad (5.21)$$

where A_1 and A_2 are the cross-sectional areas of the rectangular core, as shown in Fig. 5.6(a). Thus, the maximum flux density in the rectangular core, $B_{max,r}$, is given by

$$B_{max,r} = \max\{B_1, B_2\}. \quad (5.22)$$

Similarly, the resultant flux in the toroidal core is given by,

$$\phi_t = \phi_{cm,t} + \frac{\phi_{dm,t}}{2}. \quad (5.23)$$

Thus, the maximum flux density in the toroidal core is given as,

$$B_{max,t} = \frac{1}{A_t N_t} \left(L_{cm,t} i_{cm} + \frac{L_{dm,t} i_{dm}}{2} \right). \quad (5.24)$$

Hence, to avoid saturation in rectangular and toroidal cores, $B_{max,r}$ and $B_{max,t}$ should be less than the saturation flux density, B_{sat} , of the respective cores.

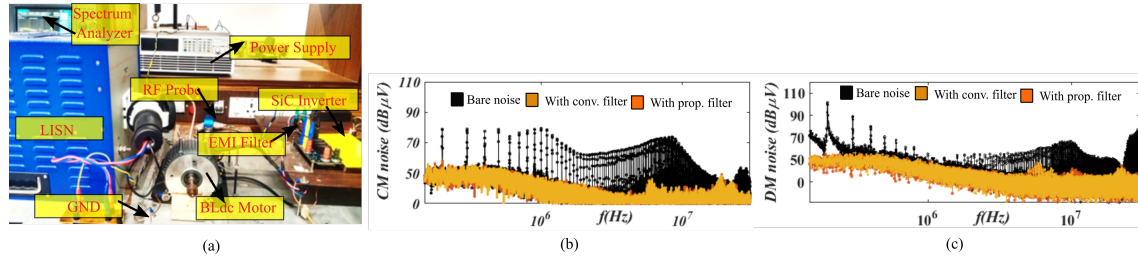


Figure 5.7: (a) Experimental setup, (b) CM spectra of conventional and presented integrated EMI choke, and (c) DM spectra of conventional and presented integrated EMI choke.

To analyze the flux distribution in the toroidal and rectangular cores, the presented integrated choke is simulated in ANSYS 3D Maxwell with the dimensions shown in Fig. 5.6(b). The CM flux generated in the toroidal and rectangular cores with the i_{cm} of 400 mA is shown in Figs. 5.6(c) and (d), respectively. As observed from Fig. 5.6(d), the CM flux in the rectangular core is in line with that considered in Fig. 5.5(d), thus validating the magnetic equivalent circuit shown in Fig. 5.5(e). In the same way, the DM flux generated in the toroidal and rectangular core for i_{dm} of 8 A is shown in Figs. 5.6(e) and (f), respectively. As observed from Fig. 5.6(f), the DM flux in the rectangular core is in line with the flux direction indicated in blue in Fig. 5.5(d).

It is observed from Fig. 5.5(d) and (f) that the maximum magnetic flux density in the rectangular core is about 0.1 T; which is less than the $B_{sat} = 0.5$ T for ferrite core material. The magnetic flux distribution in the toroidal core is shown in Fig. 5.6(c) and (e), respectively. It is observed from Fig. 5.6(c) and (e) that, the maximum magnetic flux density in the toroidal core is about 0.9 T which is less than the $B_{sat} = 1.2$ T for nanocrystalline core material.

5.4 Experimental Verification

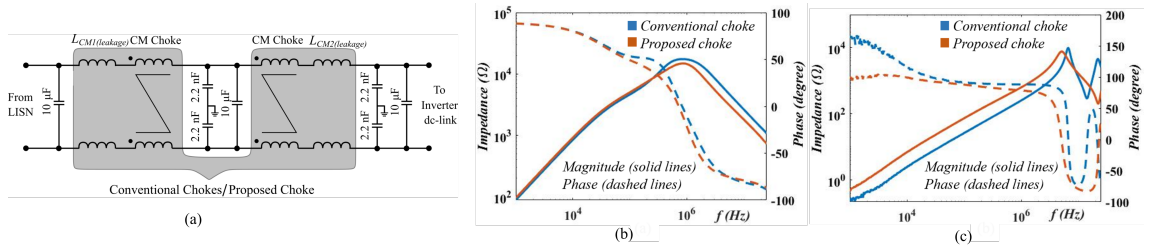


Figure 5.8: (a) DC-side two-stage EMI filter, (b) measured CM impedance of conventional and presented integrated EMI choke, and (c) measured DM impedance of conventional and presented integrated EMI choke.

The experimental setup, as shown in Fig. 5.7(a), consists of a SiC inverter (switching at 100 kHz with H-PWM-L-ON); 300 W, 48 V BLDC motor; a LISN; high-bandwidth current probe (TBCP1-150) to measure the CM and DM noise. The frequency spectra of the bare CM and DM noises are shown in Figs. 5.7(b) and (c), respectively. To attenuate the DC-side CM and DM noises a two-stage EMI filter is inserted in between the LISN and the inverter, and its parameters are shown in Fig. 5.8(a). Further, the comparison between the estimated and measured L_{cm} inductance is presented. The attenuation performance, PCB area, volume, and weight comparison of the EMI filter with the conventional and integrated choke are also discussed in detail.

5.4.1 Estimated and measured value of L_{cm} inductance

The relative permeabilities of the rectangular and toroidal cores of the presented integrated choke used in the two-stage EMI filter are 12500 and 55000, respectively. The inductance L_{cm} estimated from (5.16) and the corresponding measured values at 10 kHz are 15.14 mH. and 15.3 mH, respectively. It is observed that the estimated and measured L_{cm} match to a greater extent.

The core properties and the number of turns incorporated in two-stage EMI filters with the conventional chokes are listed in Table 5.2. The CM and DM impedances of the two-stage EMI filter with the conventional and the presented integrated chokes

are shown in Figs. 5.8(b) and (c), respectively. It is observed from Fig. 5.8 that the EMI filters with the conventional and presented integrated chokes offer similar CM impedance, additionally, there is an advantage of improved DM impedance with the presented integrated choke.

5.4.2 Attenuation performance of EMI filters with conventional and integrated chokes

The measured bare CM and DM noises at the DC-side of the motor drive system are shown in Figs. 5.7(b) and (c), respectively. It is observed from Figs. 5.7(b) and (c) that the CM and DM noises exceed the standard limit. The conventional and the presented integrated EMI filters are shown in Figs. 5.9(a) and (b), respectively. The CM and DM noise spectra were obtained by inserting the conventional EMI filter and the presented integrated EMI filter, shown in Figs. 5.9(b) and (c), respectively. It is evident from Figs. 5.7(b) and (c) that, the EMI filter incorporating the conventional and presented integrated chokes offers similar CM and DM noise attenuation performance. Thus, the two-stage EMI filters with the presented integrated choke provide similar attenuation as compared to the corresponding EMI filters with conventional chokes. Further, the benefits of the presented integrated choke in terms of the PCB area, volume, and weight are discussed in detail.

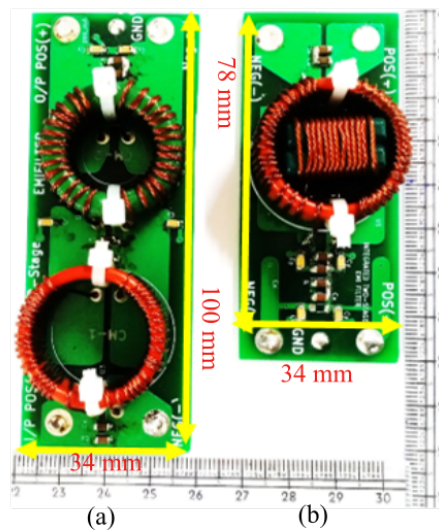


Figure 5.9: DC side two-stage EMI filter. (a) Conventional filter and (b) presented integrated filter.

Table 5.2: Magnetic Core Properties

	Nanocrystalline toroidal core	Ferrite toroidal core	Ferrite rectangular core
Model no.	T60004-12030 -W676-51	Bourns 8107-RC	Ferrite core (MnZN)
B_{max} .	1.2T	0.5T	0.5T
No. of turns (N)	20	13	12

Table 5.3: Comparison Between Conventional and presented Integrated EMI Filter

	PCB Area (mm ²)	Filter Volume (mm ³)	Filter Weight (g)
Conventional	3400	54400	69
integrated	2652	42432	51

5.4.3 Comparison of PCB Area, Volume, and Weight of EMI filters with conventional and integrated chokes

The PCB area, filter box volume, and filter weight of the two-stage EMI filter with conventional and presented integrated chokes are given in Table 5.3. The reduction in PCB area and filter box volume is 22% each, as compared to the conventional EMI filter. Moreover, it is observed from Table 5.3 that the presented integrated chokes do not cause a significant change in the overall EMI filter weight.

Thus, employing the presented integrated choke in a two-stage EMI filter reduces the PCB area and overall filter volume without a considerable change in the filter weight.

5.5 Conclusion

This chapter presents an integrated choke to reduce the volume occupied by the passive EMI filters. The CM inductance and the DM inductance of the integrated choke for single-stage EMI filters are analytically estimated and verified

experimentally. The estimated and experimental values match with great accuracy. The analysis and experimentation prove that the integrated choke offers higher DM inductance than the conventional CM choke. The EMI filter incorporating the integrated choke shows similar conducted EMI noise attenuation performance with reduced volume. Additionally, the thermal performance of the EMI filter incorporating the integrated choke is observed to be identical to that of the conventional EMI filter.

Similarly, the core arrangement and the winding structure of the integrated magnetic chokes for the two-stage EMI filter are discussed in detail. The CM inductance offered by the integrated choke is estimated from the magnetic equivalent circuits and is verified experimentally. The detailed saturation analysis is presented to estimate the maximum magnetic flux density of the integrated choke. With the same CM and DM noise attenuation performance, the EMI filter with integrated chokes significantly reduces the PCB area and the box volume of the filter, without considerable change in the weight. In particular, the PCB area and the filter box volume are reduced by 22%, compared to the conventional two-stage EMI filter.

Chapter 6

Conclusion and Future Work

6.1 Conclusion

In recent years, three-phase BLDC motor drives have gained widespread adoption, particularly in applications such as electric vehicles, solar water pumps, and compressor units in refrigeration systems. However, the efficient operation of these systems is often challenged by issues related to EMI. The thesis highlighted the significance of understanding the contribution of each phase-to-ground current to CM noise. It dispelled misconceptions and proposed a comprehensive CM equivalent circuit, incorporating all relevant parasitic capacitances and their source. The thesis investigated how CM voltage impacts the performance of BLDC drives, with a specific focus on both unipolar and bipolar PWM schemes. It highlighted differences in CM voltage generation between these schemes and analyzed how CM voltage affects CM noise and the need for CM choke. Additionally, a magnetic integrated approach was introduced to reduce the size of DC-side EMI filters, offering significant reductions in PCB area and box volume without compromising performance. Further, the detailed conclusion from each chapter is discussed.

The propagation of CM noise in the BLDC motor has been discussed with theoretical analysis and experimental validation. Two widely used modulation schemes for the BLDC motor namely, SSC and BPWM are studied. A DPI network is designed to emulate the motor phase-to-ground parasitic capacitances and provide insights on each phase-to-ground current that contributes to the CM noise in the motor. From the analysis, a generalized CM equivalent circuit is proposed including all the three-phase-to-ground parasitic capacitances of the BLDC motor. The provided analysis clarifies the misconception that two conducting phases contribute to the CM current in the BLDC motor. Additionally, it is shown that the CM noise in the 120° modulation schemes is predominantly due to the floating phase of the motor. Finally, the design of the CM choke and LC filter (passive CM filtration schemes) is presented to attenuate the CM noise in the BLDC motor drive to validate the analysis.

Further, the thesis investigated the critical phenomenon of CM voltage and its adverse effects on a three-phase BLDC drive. The CM analysis has been performed

for two distinct classes of popular PWM schemes namely, unipolar PWM and bipolar PWM for 10 kHz and 100 kHz switching frequencies.

In the case of unipolar PWM, the derived voltage expressions revealed that the pulsating nature of the CM voltages is predominant in unipolar PWM schemes. As a result, the v_{cm} generated for the H-PWM-L-ON and PWM-ON is almost the same. Thus, in the case of the unipolar PWM schemes time domain profile may appear different but the spectrum of the v_{cm} generated is almost the same for all the PWM schemes. As a result, the CM choke requirement for unipolar PWMs in a three-phase BLdc motor drive is almost the same.

In the case of bipolar PWM schemes, the C-BPWM generates less v_{cm} noise due to the complementary nature of the active phase pole voltage. However, in the case of the M-BPWM scheme, it generates high v_{cm} noise. Thus, in the case of a bipolar PWM scheme the nature of v_{cm} noise changes significantly. As a result, the CM choke requirement for C-BPWM is less compared to M-BPWM.

With the increase in f_{sw} , the v_{cm} is upward shifted, indicating that the spectral envelope of v_{cm} has increased. As a result, the CM choke requirement for H-PWM-L-ON, PWM-ON, C-BPWM, and M-BPWM increase by 82.20%, 73.2%, 73.2%, and 65.05%, respectively with increase in the switching frequency from 10 kHz to 100 kHz.

Further, in this thesis, the magnetic integrated approach is used to reduce the DC-side EMI filter size. The core arrangement and the winding structures of the two proposed integrated magnetic chokes for single-stage and two-stage EMI filters, respectively, are discussed. The CM and DM inductance offered by the two proposed integrated chokes is estimated from the magnetic equivalent circuits and is verified experimentally. The detailed saturation analysis is discussed to estimate the maximum magnetic flux density of the proposed chokes. The comparative analysis of the single-stage and two-stage EMI filters with the conventional chokes and the proposed chokes is presented. With the same CM and DM noise attenuation performance, the EMI filter with proposed chokes significantly reduces the PCB area and the box volume of the filter, without considerable change in the weight and thermal performance. In particular, the PCB area of the single-stage and two-stage EMI filter with the proposed chokes is reduced by 37% and 36%, respectively, and the box volume is reduced by 34% and 9%, respectively.

Further, the thesis discussed a way of improving the DM inductance of the conventional CM choke for large window areas. Incorporating the proposed integrated choke configuration reduces the overall volume occupied by the EMI filter by around 22%, for the similar CM and DM noise attenuation as that of the conventional EMI filter. Further, for low-voltage applications with integrated choke configuration for a two-stage EMI filter with the same CM and DM noise attenuation

performances, the EMI filter with the proposed integrated choke significantly reduces the PCB area and the box volume of the filter, without considerable change in the weight. In particular, the PCB area and the filter box volume are reduced by 22% each, compared to the conventional two-stage EMI filter.

6.2 Future work

The future scope of the work includes,

1. Exploring the analysis and mitigation techniques to reduce the EMI noise for open-end winding BLDC motor drive.
2. Investigating the radiated emissions due to the integrated structures and exploring the winding or core configurations that effectively eliminate the radiated noise.
3. Incorporating various parasitic capacitance cancellation techniques to improve the frequency response of the passive EMI filters with the presented integrated chokes.
4. Investigating the conducted EMI noise for open-end winding BLDC motor drive.

References

- [1] Jinhe Zhou, Seyyedmilad Ebrahimi, and Juri Jatskevich. Extended Operation of Brushless DC Motors Beyond 120° Under Maximum Torque Per Ampere Control. *IEEE Trans. on Energy Conv.*, 38(2):1280–1291, Ja. 2023. doi:10.1109/TEC.2023.3236594.
- [2] Nam Huh, Hyung-Seok Park, Man Hyung Lee, and Jang-Mok Kim. Hybrid PWM control for regulating the high-speed operation of BLdc motors and expanding the current sensing range of dc-link single-shunt. *Energies*, 12(22), Nov. 2019. doi:10.3390/en12224347.
- [3] Ahmad S. Al-Adsani, Michel E. AlSharidah, and Omid Beik. BLDC Motor Drives: A Single Hall Sensor Method and a 160° Commutation Strategy. *IEEE Trans. on Energy Conv.*, 36(3):2025–2035, Dec. 2021. doi:10.1109/TEC.2020.3046183.
- [4] Yen-shin Lai and Yong-kai Lin. Assessment of pulse-width modulation techniques for brushless dc motor drives. In *Proc. IEEE Industry Applications Conference Forty-First IAS Annual Meeting*, volume 4, pages 1629–1636, Oct. 2006. doi:10.1109/IAS.2006.256754.
- [5] Lei Yang, Z. Q. Zhu, Hong Bin, Zhuya Zhang, and Liming Gong. Safety operation area of zero-crossing detection-based sensorless high-speed BLdc motor drives. *IEEE Trans. Ind. Appl.*, 56(6):6456–6466, Jul. 2020. doi:10.1109/TIA.2020.3012594.
- [6] Saikat Dey and Ayan Mallik. A Comprehensive Review of EMI Filter Network Architectures: Synthesis, Optimization and Comparison, journal = Electronics. 10(16), 2021. ISSN 2079-9292. URL <https://www.mdpi.com/2079-9292/10/16/1919>. doi:10.3390/electronics10161919.
- [7] Chang liang Xia. *Permanent Magnet Brushless DC Motor Drives and Controls*. John Wiley & Sons, 2012.
- [8] Lei Yang, ZQ Zhu, Hong Bin, Zhuya Zhang, and Liming Gong. Safety Operation Area of Zero-Crossing Detection based Sensorless High Speed BLDC Motor Drives. *IEEE Trans. Ind. Electron.*, 56(6):6456–6466, Jul. 2020.
- [9] Bilal Akin and Manish Bhardwaj. Trapezoidal Control of BLDC Motors Using Hall Effect Sensors. *Texas instruments*, 2010.

- [10] S. Sashidhar, V. Guru Prasad Reddy, and B. G. Fernandes. A Single-Stage Sensorless Control of a PV-Based Bore-Well Submersible BLDC Motor. *IEEE J. Emerg. Sel. Topics Power Electron.*, 7(2):1173–1180, Jun. 2019. doi: 10.1109/JESTPE.2018.2810506.
- [11] Xiaoyan Huang, Andrew Goodman, Chris Gerada, Youtong Fang, and Qinfen Lu. Design of a Five-Phase Brushless DC Motor for a Safety Critical Aerospace Application. *IEEE Trans. Ind. Electron.*, 59(9):3532–3541, Sep. 2011.
- [12] Ashok Bindra. Wide-Bandgap-Based Power Devices: Reshaping the power electronics landscape. *IEEE Power Electron. Mag.*, 2(1):42–47, Mar. 2015.
- [13] Thomas M Jahns and Hang Dai. The past, present, and future of power electronics integration technology in motor drives. *CPSS Transactions on Power Electronics and Applications*, 2(3):197–216, Sep. 2017.
- [14] Lei Yang, ZQ Zhu, Hong Bin, and Liming Gong. Spectral Analysis and Sideband Harmonic Cancellation of Six-Step Operation with Low Carrier-Fundamental Frequency Ratio for High-Speed Brushless DC Drives. *IEEE Trans. Ind. Electron.*, 59(9), Aug. 2020.
- [15] Di Han, Casey T. Morris, Woongkul Lee, and Bulent Sarlioglu. Comparison Between Output CM Chokes for SiC Drive Operating at 20- and 200-kHz Switching Frequencies. *IEEE Trans. Ind. Appl.*, 53(3):2178–2188, Feb. 2017. doi: 10.1109/TIA.2017.2672919.
- [16] Jun-Kyu Park, Thusitha Randima Wellawatta, Zia Ullah, and Jin Hur. New equivalent circuit of the IPM-type BLDC motor for calculation of shaft voltage by considering electric and magnetic fields. *IEEE Trans. Ind. Electron.*, 52(5): 3763–3771, Oct. 2016.
- [17] Dong Jiang, Jianan Chen, and Zewei Shen. Common mode EMI reduction through PWM methods for three-phase motor controller. *CES Transactions on Electrical Machines and Systems*, 3(2):133–142, Jul. 2019.
- [18] Michele Perotti and Fiori. Investigating the EMI Mitigation in Power Inverters Using Delay Compensation. *IEEE Trans. Power Electron.*, 34(5):4270–4278, Jul. 2018.
- [19] Michele Perotti and Franco Fiori. A Closed Loop Delay Compensation Technique to Mitigate the Common Mode Conducted Emissions of Bipolar PWM Switched Circuits. *IEEE Trans. Power Electron.*, 36(5):5450–5459, Oct. 2021. doi: 10.1109/TPEL.2020.3031349.

- [20] H. Akagi, H. Hasegawa, and T. Doumoto. Design and performance of a passive EMI filter for use with a voltage-source PWM inverter having sinusoidal output voltage and zero common-mode voltage. *IEEE Trans. Power Electron.*, 19(4): 1069–1076, Nov. 2004. doi: 10.1109/TPEL.2004.830039.
- [21] Chenjun Cui, Gang Liu, and Kun Wang. A novel drive method for high-speed brushless dc motor operating in a wide range. *IEEE Trans. Power Electron.*, 30(9):4998–5008, Sep. 2015. doi:10.1109/TPEL.2014.2361752.
- [22] Yen-Shin Lai, Fu-San Shyu, and Yung-Hsin Chang. Novel loss reduction pulsewidth modulation technique for brushless dc motor drives fed by MOSFET inverter. *IEEE Trans. Power Electron.*, 19(6):1646–1652, Nov. 2004. doi:10.1109/TPEL.2004.836626.
- [23] Dong Jiang, Fei Wang, and Jing Xue. PWM impact on CM noise and ac CM choke for variable speed motor drives. *IEEE Trans. Ind. Appl.*, 49(2):963–972, Feb. 2013. doi:10.1109/TPEL.2016.2608388.
- [24] Thibaud Plazenet, Thierry Boileau, Cyrille Caironi, and Babak Nahid-Mobarakeh. A comprehensive study on shaft voltages and bearing currents in rotating machines. *IEEE Trans. Ind. Appl.*, 54(4):3749–3759, Mar. 2018. doi:10.1109/TIA.2018.2818663.
- [25] Environmental conditions and test procedures for airborne equipment, 2020. URL <https://www.rtca.org/standards/publications/>.
- [26] Fang Luo, Shuo Wang, Fei Wang, Dushan Boroyevich, Nicolas Gazel, Yong Kang, and Andrew Carson Baisden. Analysis of CM volt-second influence on CM inductor saturation and design for input EMI filters in three-phase dc-fed motor drive systems. *IEEE Trans. Power Electron.*, 25(7):1905–1914, Feb. 2010. doi:10.1109/TPEL.2010.2043541.
- [27] Yoann Y. Maillet. High-density discrete passive emi filter design for dc-fed motor drives. M.s. thesis, Virginia Polytechnic Institute and State University, Aug. 2008.
- [28] Chi Kwan Lee, Danting Xu, Bryan M. H. Pong, Sitthisak Kiratipongvoot, and Wai Man Ng. A three-winding common mode inductor. *IEEE Trans. on Power Electron.*, 32(7):5180–5187, Sept. 2017. doi:10.1109/TPEL.2016.2609435.
- [29] Yongxing Zhou, Wenjie Chen, Xu Yang, Ru Zhang, Ruitao Yan, Jinlu Liu, and Haoyu Wang. A new integrated active emi filter topology with both cm noise

- and dm noise attenuation. *IEEE Trans. on Power Electron.*, 37(5):5466–5478, Nov. 2022. doi:10.1109/TPEL.2021.3130113.
- [30] Yechi Zhang and Dong Jiang. An active emi filter in grounding circuit for dc side cm emi suppression in motor drive system. *IEEE Trans. on Power Electron.*, 37(3):2983–2992, Sep. 2022. doi:10.1109/TPEL.2021.3110144.
- [31] Shiqi Jiang, Yitao Liu, Zhaozhao Mei, Jianchun Peng, and Ching-Ming Lai. A magnetic integrated lcl-emi filter for a single-phase sic-mosfet grid-connected inverter. *IEEE J. Emerg. Sel. Top. Power Electron.*, 8(1):601–617, Aug. 2020. doi:10.1109/JESTPE.2019.2937816.
- [32] Yoann Maillet, Rixin Lai, Shuo Wang, Fei Wang, Rolando Burgos, and Dushan Boroyevich. High-density emi filter design for dc-fed motor drives. *IEEE Trans. on Power Electron.*, 25(5):1163–1172, May 2010. doi:10.1109/TPEL.2009.2039004.
- [33] Javad Borsalani, Ali Dastfan, and Javad Ghalibafan. An integrated emi choke with improved dm inductance. *IEEE Trans. on Power Electron.*, 36(2):1646–1658, Jul. 2021. doi:10.1109/TPEL.2020.3010131.
- [34] Yanwen Lai, Shuo Wang, and Boyi Zhang. Investigation of magnetic field immunity and near magnetic field reduction for the inductors in high power density design. *IEEE Trans. on Power Electron.*, 34(6):5340–5351, Sep. 2019. doi:10.1109/TPEL.2018.2868646.
- [35] Bellamkonda Dwiza, Kalaiselvi Jayaraman, Naga Brahmendra Yadav Gorla, Samarjeet Singh, and Josep Pou. Analysis of common-mode noise and design of a reduced-volume concentric choke for dual active bridge dc-dc converter with integrated magnetics. *IEEE J. Emerg. Sel. Top. Power Electron.*, pages 1–1, Apr. 2023. doi:10.1109/JESTPE.2023.3270625.
- [36] Wenhua Tan, Carlos Cuellar, Xavier Margueron, and Nadir Idir. A common-mode choke using toroid-eq mixed structure. *IEEE Trans. on Power Electron.*, 28(1):31–35, Jan. 2013.
- [37] Yongbin Chu, Shuo Wang, Ning Zhang, and Dianbo Fu. A common mode inductor with external magnetic field immunity, low-magnetic field emission, and high-differential mode inductance. *IEEE Trans. on Power Electron.*, 30(12):6684–6694, Dec. 2015. doi:10.1109/TPEL.2014.2387063.
- [38] Ning Zhu, Jinsong Kang, Dewei Xu, Bin Wu, and Yuan Xiao. An integrated ac choke design for common-mode current suppression in neutral-connected

- power converter systems. *IEEE Trans. on Power Electron.*, 27(3):1228–1236, Mar. 2012. doi:10.1109/TPEL.2011.2162748.
- [39] Rangarajan M. Tallam, Gary L. Skibinski, Todd A. Shudarek, and Richard A. Lukaszewski. Integrated differential-mode and common-mode filter to mitigate the effects of long motor leads on ac drives. *IEEE Trans. on Ind. Appl.*, 47(5): 2075–2083, Jul. 2011. doi:10.1109/TIA.2011.2161431.
- [40] Wai Keung Mo and Kasper M. Paasch. Hybrid magnetic 3-phase integrated emi filter. In *2018 20th European Conference on Power Electronics and Applications (EPE'18 ECCE Europe)*, pages P.1–P.6, Nov. 2018.
- [41] Yitao Liu, Shiqi Jiang, Weihua Liang, Huaizhi Wang, and Jianchun Peng. Modeling and design of the magnetic integration of single- and multi-stage emi filters. *IEEE Trans. on Power Electron.*, 35(1):276–288, May 2020. doi:10.1109/TPEL.2019.2915804.
- [42] Kazuhiro Umetani, Takahiro Tera, and Kazuhiro Shirakawa. Novel magnetic structure of integrated differential-mode and common-mode inductors to suppress dc saturation. In *International Power Electronics Conference (IPEC-Hiroshima 2014 - ECCE ASIA)*, pages 304–311, May 2014. doi:10.1109/IPEC.2014.6869598.
- [43] Huan Zhang, Boyi Zhang, and Shuo Wang. Integrated common mode and differential mode inductors with low near magnetic field emission. In *IEEE Energy Conversion Congress and Exposition (ECCE)*, pages 5375–5382, Nov. 2017. doi:10.1109/ECCE.2017.8096900.
- [44] Shiqi Jiang, Yitao Liu, Zhaozhao Mei, Jianchun Peng, and Ching-Ming Lai. A magnetic integrated lcl-emi filter for a single-phase sic-mosfet grid-connected inverter. *IEEE J. Emerg. Sel. Top. Power Electron.*, 8(1):601–617, Mar. 2020. doi:10.1109/JESTPE.2019.2937816.
- [45] Nam Huh, Hyung-Seok Park, Man Hyung Lee, and Jang-Mok Kim. Hybrid PWM Control for Regulating the High-Speed Operation of BLDC Motors and Expanding the Current Sensing Range of DC-link Single-Shunt. *Energies*, 12 (22), Nov. 2019. ISSN 1996-1073. doi: 10.3390/en12224347.
- [46] A.K.Wallace and R.Spee. The effects of motor parameters on the performance of brush-less DC drives. *IEEE Power Electronics Specialists Conference*, 1987. doi: 10.1109/PESC.1987.7077231.

- [47] Z.Q.Zhu H.Zhan and M.Odavic. Analysis and suppression of zero sequence circulating current in open winding PMSM drives with common DC bus. *ECCE.*, 2016. doi: 10.1109/ECCE.2016.7854872.
- [48] Timothy Hegarty. An overview of conducted EMI specifications for power supplies. *Texas instruments*, Jun. 2018.
- [49] Rajan Kumar and Bhim Singh. BLDC motor driven solar PV array fed water pumping system employing zeta converter. *IEEE Trans. Ind. Appl.*, 52(3): 2315–2322, Jan. 2016. doi: 10.1109/TIA.2016.2522943.
- [50] Kalaiselvi Jayaraman and Manish Kumar. Design of Passive Common-Mode Attenuation Methods for Inverter-Fed Induction Motor Drive With Reduced Common-Mode Voltage PWM Technique. *IEEE Trans. Power Electron.*, 35 (3):2861–2870, Jul. 2019.
- [51] Samarjeet Singh, Naga Brahmendra Yadav Gorla, Kalaiselvi Jayaraman, and Josep Pou. Analysis and mitigation of the common-mode noise in a three-phase SiC-based brushless dc motor drive with 120° conduction mode. *IEEE Trans. Power Electron.*, 37(5):5514–5523, May 2022. doi:10.1109/TPEL.2021.3133880.
- [52] Hag-Wone Kim, Hee-Keun Shin, Hyungsoo Mok, Yong-Kyun Lee, and Kwan-Yuhl Cho. Novel PWM Method with Low Ripple Current for Position Control Applications of BLDC Motors. *Journal of Power Electronics*, 11: 726–733, Sept. 2011. doi:10.1109/TPEL.2016.2608388.
- [53] Clayton R Paul, Robert C Scully, and Mark A Steffka. *Introduction to electromagnetic compatibility*. John Wiley & Sons, 2022.
- [54] Di Han, Casey T. Morris, Woongkul Lee, and Bulent Sarlioglu. Comparison between output CM chokes for SiC drive operating at 20 and 200-kHz switching frequencies. *IEEE Trans. Ind. Appl.*, 53(3):2178–2188, Feb. 2017. doi:10.1109/TIA.2017.2672919.
- [55] Ho-Jin Kim, Hyung-Seok Park, and Jang-Mok Kim. Expansion of operating speed range of high-speed bldc motor using hybrid pwm switching method considering dead time. *Energies*, 13(19), 2020. ISSN 1996-1073. doi: 10.3390/en13195212.
- [56] Mohamed Dahbi, Said Doubabi, and Ahmed Rachid. Current spikes minimization method for three-phase permanent magnet brushless dc motor with real-time implementation. *Energies*, 11(11), 2018. ISSN 1996-1073. doi: 10.3390/en11113206.

- [57] Dae-kyong Kim, Kwang-woon Lee, and Byung-il Kwon. Commutation torque ripple reduction in a position sensorless brushless dc motor drive. *IEEE Trans. on Power Electron.*, 21(6):1762–1768, Nov. 2006. doi:10.1109/TPEL.2006.882918.
- [58] Fang Luo, Dushan Boroyevich, Paolo Mattevelli, Khai Ngo, David Gilham, and Nicolas Gazel. An integrated common mode and differential mode choke for emi suppression using magnetic epoxy mixture. In *Twenty-Sixth Annual IEEE Applied Power Electronics Conference and Exposition (APEC)*, pages 1715–1720, 2011. doi: 10.1109/APEC.2011.5744827.
- [59] Di Han, Casey T. Morris, Woongkul Lee, and Bulent Sarlioglu. Comparison between output cm chokes for sic drive operating at 20- and 200-khz switching frequencies. *IEEE Trans. on Ind. Appl.*, 53(3):2178–2188, Feb. 2017. doi:10.1109/TIA.2017.2672919.